

博士論文

**A Study on Biomechanical Simulation of Human  
Respiratory System with Finite Element Method**  
(有限要素法による呼吸器系生体力学シミュレーション  
手法に関する研究)

**Sept. 2016**

(平成 28 年 9 月)

**Zhang Guangzhi**

(張 広志)

**Yamaguchi University**

山口大学大学院医学系研究科

# CONTENTS

<b>List of figure</b> .....	i
<b>Acknowledgement</b> .....	v
<b>Abstract</b> .....	vii
<b>1 Introduction</b> .....	1
1.1 Anatomy and biomechanical phenomena in human respiratory system.....	1
1.2 Previous studies on modeling human respiratory system.....	4
1.3 Approach and outline of this study.....	9
<b>2 Action of intercostal muscle contraction on rib movement</b> .....	11
2.1 Method.....	14
2.1.1 Finite element model of chest.....	14
2.1.2 Transversely isotropic hyperelastic material model for respiratory muscles.....	16
2.1.3 Simulation condition.....	22
2.1.4 Simulation procedure.....	23
2.2 Results.....	25
2.2.1 Rib movement generated by intercostal muscles in a single interspace.....	25
2.2.2 Deflection of ribs during muscle contraction.....	25
2.2.3 Rib movement generated by individual intercostal muscle.....	26
2.2.4 Rib movement generated by entire inspiratory and expiratory Intercostal muscles.....	38
2.3 Discussion.....	41
2.3.1 Reproduction of the theory of Hamberger.....	41
2.3.2 Relationship between rigid rotation and deformation of ribs.....	41
2.3.3 Action of intercostal muscle contraction on ribs.....	42
2.3.4 The net effect during entire intercostal muscle contraction.....	48
2.4 Conclusions.....	51
<b>3 Simulation of thorax deformation by activating intercostal muscles and diaphragm</b> .....	53
3.1 Method.....	54
3.1.1 Simulation conditions.....	54
3.1.2 Simulation procedure.....	55
3.2 Results.....	57
3.2.1 Rib motion.....	57
3.2.2 Diaphragm motion.....	64
3.2.3 Thorax deformation during normal quiet breathing and comparison with 4D-CT images.....	69
3.3 Discussion.....	77
3.3.1 Rib motion.....	78
3.3.2 Diaphragm motion.....	80
3.3.3 Validation of simulated thorax deformation with 4D-CT images.....	82

3.4	Conclusions.....	85
<b>4</b>	<b>Simulation of lung deformation and ventilation.....</b>	<b>86</b>
4.1	Method.....	86
4.1.1	Porous hyperelastic material model.....	86
4.1.2	Simulation conditions.....	94
4.2	Results and discussion.....	94
4.2.1	Lung deformation.....	94
4.2.2	Ventilatory volume, alveolar and pleural pressures during normal quiet breathing.....	96
4.4	Conclusions.....	98
<b>5</b>	<b>Influences of ventilation on blood circulation during cardiopulmonary resuscitation.....</b>	<b>99</b>
5.1	Method.....	100
5.1.1	Connection of the circulatory system.....	100
5.1.2	Simulation procedure.....	101
5.2	Results and discussion.....	102
5.2.1	Deformation of lung and heart.....	102
5.2.2	Open airway and occluded airway cardiopulmonary resuscitation...103	
5.2.3	Open-occluded airway and occluded-open airway cardiopulmonary resuscitation.....	106
5.2.4	Occluded-open-occluded-open airway cardiopulmonary resuscitation.....	108
5.3	Conclusions.....	111
<b>6</b>	<b>Conclusions.....</b>	<b>113</b>
	<b>References.....</b>	<b>116</b>

# List of figure

<b>Fig. 1-1</b> Locations of the lungs, ribs, intercostal muscles, diaphragm and pleural space in human chest.....	2
<b>Fig. 1-2</b> Rib rotation axis and representative rib motion.....	2
<b>Fig. 1-3</b> Locations of central tendon and muscles in the diaphragm.....	3
<b>Fig. 2-1</b> FEM model of the rib cage and intercostal muscles.....	15
<b>Fig. 2-2</b> FEM model of lungs and heart.....	15
<b>Fig. 2-3</b> FEM model of diaphragm.....	15
<b>Fig. 2-4</b> Fiber orientation of intercostal muscles measured by Loring.....	16
<b>Fig. 2-5</b> Fiber orientation of diaphragm.....	16
<b>Fig. 2-6</b> Hill's three-element muscle model.....	18
<b>Fig. 2-7</b> Active force-length relationship of the diaphragm and intercostal muscles of an adult baboon.....	20
<b>Fig. 2-8</b> The rib movements due to the contraction of the external and internal interosseous intercostal muscles in one interspace locating between the rib 5 and 6.....	26
<b>Fig. 2-9</b> Different motions and structures of the upper and lower ribs.....	27
<b>Fig. 2-10</b> Portion 1, 2 and 3 divided according to the distribution of moment along curved ribs studied by De Troyer et al. ....	28
<b>Fig. 2-11</b> The fragments of the internal intercostal muscles.....	31
<b>Fig. 2-12</b> The fragments of the external intercostal muscles.....	31
<b>Fig. 2-13</b> The normalized displacement of the sternum generated by separate fragments of the internal intercostal muscles.....	32
<b>Fig. 2-14</b> The normalized displacement at lateral extremes of the ribs from rib 1 to 5 generated by separate fragments of the internal intercostal muscles.....	32
<b>Fig. 2-15</b> The normalized displacement at lateral extremes of the ribs from rib 6 to 10 generated by separate fragments of the internal intercostal muscles.....	33
<b>Fig. 2-16</b> The normalized displacement of the sternum generated by separate fragments of the external intercostal muscles.....	33
<b>Fig. 2-17</b> The normalized displacement at lateral extremes of the ribs from rib 1 to 5 generated by separate fragments of the external intercostal muscles.....	34

<b>Fig. 2-18</b>	The normalized displacement at lateral extremes of the ribs from rib 6 to 10 generated by separate fragments of the external intercostal muscles.....	34
<b>Fig. 2-19</b>	Rib motion caused by fragment 4 of external intercostal muscles in portion 1.....	35
<b>Fig. 2-20</b>	Rib motion caused by fragment 3 of internal interosseous intercostal muscles in portion 1.....	35
<b>Fig. 2-21</b>	Rib motion caused by fragment 7 of external intercostal muscles in portion 2.....	36
<b>Fig. 2-22</b>	Rib motion caused by fragment 7 of internal intercostal muscles in portion 2.....	36
<b>Fig. 2-23</b>	Rib motion caused by fragment 8 of internal intercostal muscles in portion 3.....	37
<b>Fig. 2-24</b>	The front view of the inspiratory chest movement generated by the inspiratory intercostal muscles.....	39
<b>Fig. 2-25</b>	The lateral view of the inspiratory chest movement generated by the inspiratory intercostal muscles.....	39
<b>Fig. 2-26</b>	The front view of the inspiratory chest movement generated by the expiratory intercostal muscles.....	40
<b>Fig. 2-27</b>	The lateral view of the inspiratory chest movement generated by the expiratory intercostal muscles.....	40
<b>Fig. 2-28</b>	Mechanical actions of the intercostal muscles in portion 2 and 3 and simulated deformation results.....	47
<b>Fig. 2-29</b>	Deformation shift direction due to component going along the ribs of the muscle force and net effect direction due to the component normal to the ribs of the muscle force.....	48
<b>Fig. 3-1</b>	Time dependence of activation of the diaphragm and intercostal muscles.....	55
<b>Fig. 3-2</b>	Front view of inspiratory rib motion generated by the intercostal muscles.....	58
<b>Fig. 3-3</b>	Rear view of inspiratory rib motion generated by the intercostal muscles.....	58
<b>Fig. 3-4</b>	Lateral view of inspiratory rib motion generated by the intercostal muscles.....	59
<b>Fig. 3-5</b>	Front view of expiratory rib motion generated by the intercostal muscles.....	59
<b>Fig. 3-6</b>	Rear view of expiratory rib motion generated by the	

intercostal muscles.....	60
<b>Fig. 3-7</b> Lateral view of expiratory rib motion generated by the intercostal muscles.....	60
<b>Fig. 3-8</b> Comparison of simulated and experimental bucket-handle angle during inspiratory chest movement.....	62
<b>Fig. 3-9</b> Comparison of simulated and experimental pump-handle angle during inspiratory chest movement.....	62
<b>Fig. 3-10</b> Simulated bucket-handle angle during expiratory chest movement.....	63
<b>Fig. 3-11</b> Simulated pump-handle angle during expiratory chest movement.....	63
<b>Fig. 3-12</b> Clinical observation of the diaphragm motion and chest movement on the sagittal plane in MRI scans.....	65
<b>Fig. 3-13</b> Simulation results of the right hemidiaphragm for comparison with the clinical observation.....	66
<b>Fig. 3-14</b> Front view of the diaphragm deformation.....	66
<b>Fig. 3-15</b> Rear view of the diaphragm deformation.....	67
<b>Fig. 3-16</b> Motion of the rib cage caused by isolated contraction of the diaphragm.....	67
<b>Fig. 3-17</b> Distribution of muscle forces based on the radial fibre orientation in the diaphragm.....	68
<b>Fig. 3-18</b> Simulation results of the right hemidiaphragm from simultaneous activation of the diaphragm and inspiratory intercostal muscles for comparison with the clinical observation.....	68
<b>Fig. 3-19</b> The front view of obtained thorax deformation.....	71
<b>Fig. 3-20</b> The lateral view of obtained thorax deformation.....	71
<b>Fig. 3-21</b> The oblique view of obtained thorax deformation.....	72
<b>Fig. 3-22</b> Location of planes X and Z in the chest.....	72
<b>Fig. 3-23</b> CT images on plane X.....	73
<b>Fig. 3-24</b> Extracted motion of plane X from CT images.....	73
<b>Fig. 3-25</b> The simulation results on plane X.....	74
<b>Fig. 3-26</b> CT images on plane Z.....	74
<b>Fig. 3-27</b> Extracted motion of plane Z from CT images.....	75
<b>Fig. 3-28</b> The simulation results on plane Z.....	75
<b>Fig. 3-29</b> Movement at location L1 on plane Z compared with 4D-CT images.....	76
<b>Fig. 3-30</b> Movement at location L2 on plane Z compared with 4D-CT images.....	76

<b>Fig. 3-31</b>	Movement at location L3 on plane Z compared with 4D-CT images.....	77
<b>Fig. 4-1</b>	Front view of lung deformation during normal quiet breathing.....	95
<b>Fig. 4-2</b>	Lateral view of lung deformation during normal quiet breathing.....	96
<b>Fig. 4-3</b>	Variations of alveolar, pleural pressures and lung volume change during normal quiet breathing respiration.....	96
<b>Fig. 5-1</b>	The main and lung circulation, and preload and afterload in human body....	101
<b>Fig. 5-2</b>	Circuit of the preload and afterload connected to the FEM model of the heart.....	101
<b>Fig. 5-3</b>	Deformation results of the thorax.....	102
<b>Fig. 5-4</b>	Deformation results of the lung.....	103
<b>Fig. 5-5</b>	Deformation results of the heart.....	103
<b>Fig. 5-6</b>	Heart volume change during open and occluded airway CPR.....	104
<b>Fig. 5-7</b>	Pleural pressure during open and occluded airway CPR.....	105
<b>Fig. 5-8</b>	Pressure in the heart during open and occluded airway CPR.....	105
<b>Fig. 5-9</b>	Heart volume change during occluded-open and open-occluded airway CPR.....	106
<b>Fig. 5-10</b>	Pleural pressure during occluded-open and open-occluded airway CPR.....	107
<b>Fig. 5-11</b>	Pressure in the heart during occluded-open and open-occluded airway CPR.....	107
<b>Fig. 5-12</b>	The displacement of the sternum in dorsal direction during occluded-open-occluded-open airway CPR.....	109
<b>Fig. 5-13</b>	Heart volume change during occluded-open-occluded-open airway CPR...	110
<b>Fig. 5-14</b>	Pleural pressure during occluded-open-occluded-open airway CPR.....	110
<b>Fig. 5-15</b>	Pressure in the heart during occluded-open-occluded-open airway CPR....	111

# Acknowledgement

I would like to personally thank the following people who supported me during writing this thesis.

First I would like to express my deepest appreciation to my supervisor, Professor Xian CHEN. Thank you for your time and patience for the discussion of my research, careful explanation of mechanical problems, and critical review of my work. Thank you for all the care for me all the time. I also thank the examiner committee, Associate Professor Junji OHGI, Professor Takashi SAITO, Associate Professor Koji MORI, Professor Shoji KIDO, Associate Professor Yasushi HIRANO for their suggestions and reviews during the examination.

Moreover, I would like to thank to Professor Toshiaki HISADA for his valuable advice and support. And I also appreciate the Doctor Seiryu SUGIURA for his helpful advice of my research, Doctor Toshiro MIURA, Radiological Technologist Akira NAKAMOTO and Radiological Technologist Chikanori MATSUMURA for the supply of medical data and review comments.

I really appreciate all of members in Medical Mechanical engineering laboratory Yamaguchi University Japan, thank you for giving me a very pleasant researching and study environment.

I extend special thanks to Dr. S. H. Loring, (Harvard Medical School, USA) for the experimental data on intercostal muscle orientation under NIH grant HL33009. This research was supported by the Japan Society for the Promotion of Science (JSPS) through the Funding Program for World-Leading Innovative R&D on Science and Technology (FIRST

Program) initiated by the Council for Science and Technology Policy (CSTP).

Finally, I really want to appreciate my father Juming Zhang and mother Fengxia Wang for bringing me up and 10 years support during study abroad in Japan.

Guangzhi ZHANG

Hiroshima city, September 2016

# Abstract

The human respiratory system has a complex structure that stretches from the trachea to the alveoli and involves many physiological phenomena such as the airflow, lung deformation, oxygen exchange, pleural pressure distribution, alveolar pressure distribution, respiratory muscle activation, and chest movement. Unfortunately, many respiratory diseases such as chronic obstructive pulmonary disease (COPD), pneumothorax, diaphragmatic paralysis, and lung cancer adversely affect this system. The biomechanical simulation of human respiratory system is expected to be a useful tool for diagnosis and treatment of respiratory diseases. This work aims to establish a computational model in order to reproduce the biomechanical phenomena happened during human breathing. In order to reproduce a reasonable mechanical environment inside the chest during breathing, we focus on activating the respiratory muscles to generate respiratory chest movements in terms of the actual physiological activity during breathing from a biomechanical point of view. According to pathological needs on diagnosis and treatment of respiratory diseases, the basic physiological phenomena during breathing are firstly essential to be reproduced by the computational model, such as the rib motion, diaphragm motion, lung deformation, ventilation, alveolar pressure and plural pressure inside the chest.

During human breathing, the biomechanical phenomena inside the thorax are determined by the thorax deformation, therefore at first we simulated the thorax deformation. The thorax deformation consists of rib motion driven by the contraction of the intercostal muscles and diaphragm motion.

Hence, in order to provide a reasonable mechanical environment for the organs inside the chest, the mechanical action of the intercostal muscles on the rib cage was firstly investigated, that what rib motion can be generated by the contraction of the intercostal muscles and why these motions are happened. After that the thorax deformation was reproduced by considering the diaphragm motion additionally. To reproduce the muscle contractions, we introduced the Hill-type transversely isotropic hyperelastic continuum skeletal muscle model, which allows the intercostal muscles and diaphragm to contract along the muscle fiber directions with clinically measurable muscle activation and active force-length relationship. The anatomical fiber orientations of the intercostal muscles and diaphragm were introduced. We first reproduced the representative motions of the rib and diaphragm in physiology. Afterwards, by activating the diaphragm and intercostal muscles simultaneously, the thorax deformation was simulated. Furthermore, the deformation results were compared with four-dimensional computed tomography (4D-CT) images for validation.

After reproduced the thorax deformation, in order to simulate the lung deformation, ventilation and pressures inside the chest during breathing, we modeled the lungs as porous hyperelastic material and established the respiratory model. The porous hyperelastic material can macroscopically reproduce the lung deformation and the airflow during ventilation simultaneously by considering the permeability between the lung parenchyma and air flow. Consequently, the variations of lung volume change, alveolar and pleural pressures during respiration were also reproduced and have a good consistence with the clinical observation.

The ventilation can affect the mechanical environment in the chest. With this established respiratory model, as an application, we additionally investigated influences of the ventilation on blood circulation during cardiopulmonary resuscitation (CPR). In order to reproduce the heart volume change due to inflow and outflow of blood inside the heart, we considered the blood inside the heart as the porous hyperelastic material and connected preload and afterload circuits representing the blood circulatory system. From the simulation results of the pleural and the cardiac chamber pressure and the volume change of the heart, we found the occluded airway system could promote the blood flow in the heart during CPR, as obtained in the experiments performed on domestic swine. Based on this, we also investigated that an occluded-open-occluded-open airway process could better increase flow rate of the blood to promote the efficiency of CPR.

# 1

## Introduction

---

### **1.1 Anatomy and biomechanical phenomena in human respiratory system[1], [2]**

During human breathing, the lungs are passive tissues and expanded by the thorax deformation. The thorax deformation is provided by the contraction of respiratory muscles. The main respiratory muscles are the intercostal muscles and the diaphragm. The intercostal muscles are inserted between the ribs consist of two muscle layers, which are the external and internal intercostal muscles. The diaphragm is located between the thoracic and abdominal cavity, as shown in Fig. 1-1. During normal breathing, the external intercostal muscles and diaphragm contract simultaneously to provide an increase of chest circumference anteroposteriorly and transversally and descend the bottom of the lungs inferiorly. Meanwhile, negative pleural pressure is generated in the pleural space, which is filled with incompressible fluid to provide lubrication for the sliding between the lungs and the thorax. Therefore, the lungs could be expanded and slide against the chest wall during breathing.

The rib motion and the diaphragm deformation determine the lung deformation during breathing. The rib motion is generated by the contraction of the intercostal muscles, and the direction of rib rotation is determined by the rib rotation axis consisting of two vertebral joints (costovertebral and costotransverse joints). Fig. 1-2 A and B illustrate the

location of the rib rotation axis for the upper and lower ribs. The directions of rib rotation axis are in the lateral directions for the upper ribs, and in the dorsal-ventral directions for the lower ribs. Therefore, when the intercostal

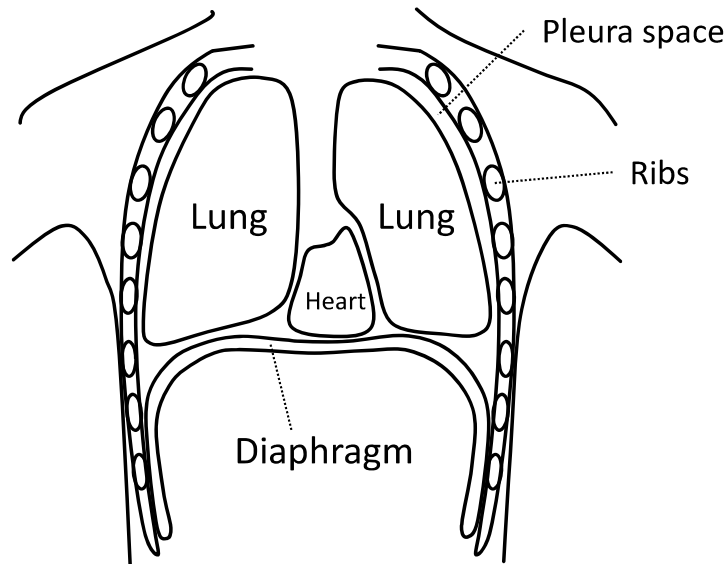


Fig. 1-1 Locations of the lungs, ribs, intercostal muscles, diaphragm and pleural space in human chest.

muscles contract, the upper and lower ribs perform pump-handle and bucket-handle motions, respectively, as show in Fig. 1-2 A and B. The pump-handle and bucket-handle motions make the upper lungs be expanded anteroposteriorly and lower lungs be expanded transversally, respectively.

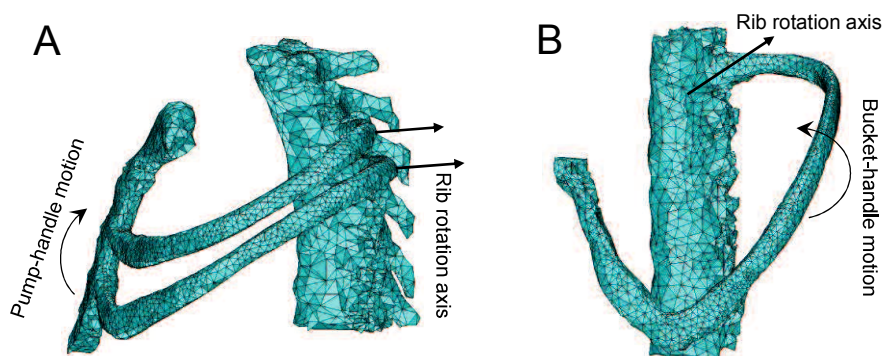


Fig. 1-2 Rib rotation axis and representative rib motion

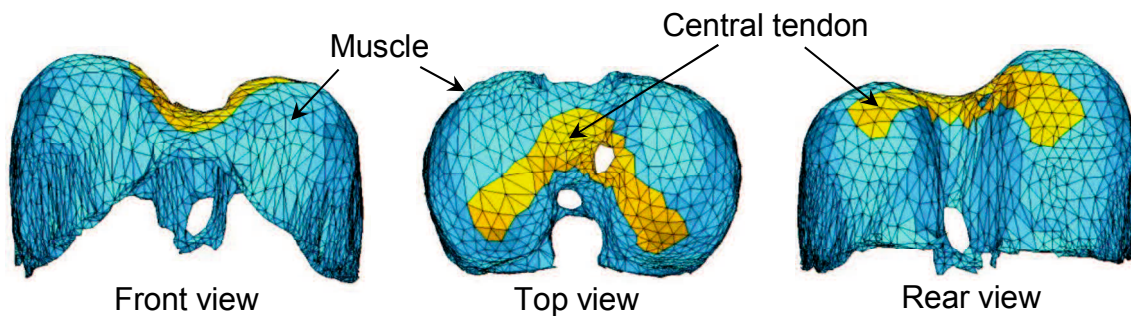


Fig. 1-3 Locations of central tendon and muscles in the diaphragm

On the other hand, the diaphragm expands the lungs in supero-inferior direction. It consists of two domes and the right dome is located more superior than the left dome. As Fig. 1-3 illustrates, the diaphragm is constituted of a central tendon and muscle fibers [3]. The muscle fibers are connected with the lower rib cage. Therefore, the contraction of the muscle fibers lowers the central tendon during breathing as well as pulls the lower ribs along the muscle fiber directions of the diaphragm. Because the intercostal muscles also act on the ribs, hence there is an interaction between diaphragm and intercostal muscles during breathing. Thereby, it is significant that the action of intercostal muscle contraction on rib movement, the diaphragm deformation and the interaction between the intercostal muscles and the diaphragm dominate the thorax deformation as well as the lung deformation. Consequently, the respiratory muscle contraction is fundamental biomechanical phenomenon which leads to a series of physiological and biomechanical phenomena during breathing exercise, such as the rib motion, diaphragm motion, lung deformation, ventilation, alveolar pressure and plural pressure inside the chest.

## **1.2 Previous studies on modeling human respiratory system**

A computational model of the human respiratory system would be a valuable aid to the diagnosis and treatment of the respiratory diseases and elucidation of physiological problems of the respiratory system. For example, chronic obstructive pulmonary disease (COPD) is characterized by the presence of airflow limitation, which is assessed by spirometry test or medical images such as multi detector-row computed tomography (MDCT) [4] in the diagnosis processes. However, the former does not provide information inside of the lung and the later only represents the morphologic feature without the airflow details. Computational models have been proposed to investigate the relationship between imaging measurements and disease severity for developing improved diagnostic methods [5]. On the other hand, computational fluid dynamic analyses have been performed to simulate pharmaceutical aerosol delivery by predicting the site of pharmaceutical aerosol deposition within the airways in the inhaled medicine for treating respiratory diseases [6]. Furthermore, lung deformation simulations have been applied to the radiation therapy for accurate prediction of the lung tumour motion due to breathing [7]. Moreover, the patients with pectus excavatum easily become short of breath and tire during exercise, and the cardiorespiratory function could be significantly improved after surgery [8]. However, the postoperative pain and other effects after surgery also puzzle the doctors in clinical. For that reason, the finite element analyses of rib cage were performed to elucidate stress distribution on the rib cage [9] and dynamic effects on the spine with asymmetric thoraces [10] after Nuss procedure.

The extreme goal of this research is to build a biomechanical computational model of respiratory system coupling the airflow in the bronchial system with the lung deformation for the diagnosis and treatment of the respiratory disease. To that end, it is first essential to develop an approach to simulating thorax deformation produced by respiratory muscle contraction as well as reproducing the ventilation and lung deformation in terms of the actual physiological activity during breathing from a biomechanical point of view.

Regarding the previous studies of modeling human respiratory system with biomechanical computational approach, because of the breathing exercise consists of the biomechanical phenomena: respiratory muscle contraction, thorax deformation, lung deformation and ventilation, so that some studies concentrated on revealing the respiratory muscles action [11]–[15], and some studies focused on reproducing the thorax deformation during breathing[16]–[23], furthermore some studies investigated the approaches to simulate the lung deformation [24]–[26], the air flow and ventilation [27]–[34].

The intercostal muscles and diaphragm are the main muscle during human breathing. Loring investigated the action of the intercostal muscles by modeling the intercostal muscles and rib cage with beam elements. Base on the anatomic and mechanical measurements in dogs and human cadavers, the canine [12] and human [11] FEM model were constructed. The muscles forces were applied along the muscle fiber directions in each interspace of ribs. Loring demonstrated the two dimensional geometric model of Hamberger, that the external and internal intercostal muscles can cause inspiratory and expiratory rib movements. In addition, with this three

dimensional FEM model, Loring found the intercostal muscles at the side of the rib cage generate the anteroposterior chest motion and the muscles at the front and back of the rib cage produce the transverse chest motion during human breathing. The diaphragm action is directly linked to the respiration. Because the complex geometric structure of the diaphragm, the diaphragm was modeled using three dimensional continuum approach with tetrahedral [17] and shell [13], [14] finite elements. Ladjal et al. considered the diaphragm as elastic and compressible tissues, and the Young's modulus and Poisson's ratio were applied in this study [17]. For the muscle contraction force, external forces were applied on the surfaces of the tetrahedral meshes. Simulated deformations of cross-sections of the diaphragm were compared with the clinical data observed in CT images for validation. Although obtained diaphragm movement was consistent with the observation in CT images with a small diaphragm movement, the linear elastic constitutive law is just suitable for small displacement problem, and the diaphragm always perform large movement during breathing exercise. Pato et al. simulated the diaphragm motion by using non-linear constitutive law and considering the muscle fibers as incompressible transverse isotropy hyperelastic tissues [13], [14]. These studies also introduced Hill's three-element skeletal muscle model into the constitutive law to make the muscle contract along the fiber directions measured from a female cadaver. Unfortunately, obtained diaphragm motion was not confronted with clinical data for validation. More importantly, not only the diaphragm, the intercostal muscles also participate the breathing exercise and generate rib movement, furthermore the rib movement provide a boundary condition for simulating the diaphragm motion. Regrettably, the influence from the rib

cage was not been considered in the studies mentioned above [13], [14],[17].

Indeed, DiMarco et al. have demonstrated that there is a synergism between the contraction of the diaphragm and intercostal muscles [35]. The intercostal muscle could decrease the shortening of the diaphragm muscle fibers via the rib movements to make the diaphragm generate greater muscle force to resist the abdominal and pleural pressures during breathing. Therefore, the diaphragm and rib motion should be considered and reproduced simultaneously, thereby the thorax deformation is obtained. Michel et al. simulated the thorax deformation using a hexahedral finite element model of the upper human body, which developed for rad safety [16]. The rib cage, lung heart, diaphragm and abdominal tissues were included in this FEM model and meshed independently. The muscle force was applied with beam element along the muscle fiber direction for the intercostal muscles and diaphragm. They simulated the thorax deformation during a respiratory cycle from functional residual capacity to total lung capacity. Unfortunately, they did not used a continuum model for the muscle contractions especially for the diaphragm, and they did not give details of the lung deformation and discuss the mechanical environment during the lung deformation. With a series of investigations, Ladjal et al. proposed an approach to simulating the thorax deformation including the rib movement and the diaphragm motion [17]–[21]. They first developed an approach to simulate the rib movements by considering the ribs as rigid bodies which doing rigid rotation around the around the spinal joints. In addition, the displacement caused by the rib rigid rotation was applied as the displacement boundary condition in order to simulate the thorax

deformation. The diaphragm deformation was simulated by applying pressures on the surface of diaphragm meshes. With experiments [36] and simulations [11], [12], it is demonstrated that the ribs could be easily bent by the contraction of the intercostal muscles and the rib cage could store the strain energy during inhaling process to assist the expiration, therefore it is not appropriate to consider the ribs as pure rigid bodies in order to simulate the thorax deformation.

Reproducing the thorax deformation could provide a boundary condition for the lung simulation, and the organ playing the most important role during respiration is the lung. Hence, lots of studies directly focused on constructing a computational mechanical model for the lung. Some studies simulated pulmonary air flow with computational fluid dynamics (CFD) method in order to understand the etiology of lung pathology to improve drug delivery methods [6], [31]. However, they did not consider the influence from the lung deformation. On the other hands, the lung deformation simulating approaches also have been investigated to predict the lung tumour movement during radiation therapy [21], [24]–[26]. In these studies, the lung was considered as an isotropic elastic or hyperelastic tissue with a displacement or pressure boundary condition instead of the respiratory muscle contraction. Therefore, the simulation results were mainly concentrated on the lung deformation without any discussion of the mechanical environment inside or outside the lung. Conversely, revealing the relationship between the mechanical environment, airflow inside the lung and the lung deformation has a wider range of applications in clinical, such as contributions to the improvement of mechanical ventilation method or development of advanced diagnostic and treating methods of COPD [27].

In order to consider the lung deformation and the air conduction simultaneously, some studies concentrated on simulating the coupling between the air conducting part (the trachea and bronchi) and the respiratory part (the parenchymal lung tissue) of the respiratory system [27]–[29]. This method requires very fine meshes and therefore need large-scale high-performance computing platforms and scalable parallel solvers to calculate the coupled system. Detailed information such as the pressure at the end of the airway tree and the deformation of surrounding tissues during breathing could be obtained. During breathing exercise, the airflow inside the lung is mainly influenced by the lung deformation, in addition the lung deformation is determined by the thorax deformation due to the respiratory muscle contraction. Therefore, in order to reproduce reasonable biomechanical environment for the lung behavior during human breathing, the respiratory muscle contraction and thorax deformation cannot be ignored. Unfortunately, these studies did not take account of the respiratory muscles and the thorax deformation, moreover there has no study simulated the human breathing by activating the respiratory muscles to reproduce a series of physiological and biomechanical phenomena during breathing exercise, range from the rib motion and diaphragm motion to the mechanical environment inside the chest, in terms of the actual physiological activity during breathing from a biomechanical point of view.

## **1.2 Approach and outline of this study**

In order to establish a computational mechanics model of the human respiratory system, this work attaches importance to the respiratory muscle contraction that is relationship between the respiratory muscle contraction

and the thorax deformation, and an important foundation for the simulation of the lung behaviour. Due to the complicated structure of the rib cage, we first investigate the detailed action of the intercostal muscles on the rib movements in chapter 2 and the diaphragm motion in chapter 3, thereby the thorax deformation is reproduced. After that, in chapter 4, the lung deformation and the ventilation is simulated by introducing porous hyperelastic material model. This approach let us obtained the alveolar pressure and pleural pressure generating the mechanical environment inside and outside the lungs during breathing. By the way, concerning the influence from the bronchial tree on the lung deformation, it is demonstrated that the stiffness property of the bronchial tree has no significant effect on simulating the lung deformation with finite element method [26] and the resistance happened in the bronchial tree is relatively small in the normal cases, therefore at current stage we do not introduce the bronchial tree provisionally. During inspiration, decreasing of the pleural pressure expands the lung to perform ventilation, and conversely the ventilation can also affect the mechanical environment in the chest. In chapter 5, established respiratory model is further used to investigate influence of the ventilation on the blood circulation during cardiopulmonary resuscitation (CPR) by additionally connecting blood circulatory system to the mesh of heart. According to the simulation results, we also propose a more efficient way to perform CPR, which could make more blood flow out of the heart during CPR.

## **2 Action of intercostal muscle contraction on rib movement**

---

The intercostal muscles are the predominant muscle generating the chest movement during human breathing. In order to model the human breathing, it is essential to understand the action of the intercostal muscles on generating the rib motion. The action of the intercostal muscles has been a subject in physiology for a long time. Unfortunately, there are also some controversies about the action of the intercostal muscle. Some studies described the intercostal muscles have respiratory actions [37]–[39], [36], [40], and some investigations agreed with the intercostal muscles mainly contribute to the trunk motion [41]–[43]. Recently, investigating the action of the intercostal muscles has been divided into two steps, (1) is to find out the mechanical action of the inspiratory muscles that is the relationship between the muscle contraction and the rib displacement, and (2) is to confirm the connections between the rib displacement and the respiratory effect [37], [40]. Step (2) could be obtained by applying external forces or displacements to each rib and measuring the airway pressure [37], [40]. However, because it is almost impossible to selectively activate the individual muscle groups as confessed by Wilson and De Troyer [39], step (1) has not been able to be directly obtained. Therefore, in order to understand the function of the intercostal muscles, the problem is to investigate the mechanical action of the inspiratory muscles.

The rib motions generated by the intercostal muscle contractions have just been roughly considered as doing rigid rotation around the spinal joints by far. It had been first explained by the theory of Hamberger over two centuries [44] that attributed the rib motion to the moment about spinal joints resulted from the contraction of intercostal muscles. Furthermore, this 2-dimensional theory was extended to describing 3-dimensional curved ribs by De Troyer [37]. This extended Hamberger theory involves the moment distribution on curved ribs for rib rigid rotation around the spinal joints. However, the experiments also illustrated that the ribs and especially the costal cartilages could not only rigidly rotate but also deform to restore the strain energy for expiration during breathing [45], and two adjacent ribs could also be bent toward to each other by the muscle forces of the intercostal muscles [36]. It implied that the cartilage and the ribs could be easily deformed under the intercostal muscle forces. Hence, in order to find out the relationship between the muscle contraction and the rib displacement, it is necessary to consider not only the rigid rotation of the rib cage but also the issue deformation in the rib cage happened during intercostal muscle contraction.

As described by Wilson and De Troyer, the complicated structure of the rib cage causes complex relation between the muscle force and the bone displacement throughout the rib cage [39]. For such a complicated structure of the human rib cage, finite element analysis (FEA) is a useful tool to qualitatively study the rib displacement and investigate the mechanism during intercostal muscle contraction. By using FEA, Loring inferred the rib movement generated by the internal intercostal muscles, external intercostal muscles, parasternal intercostal muscles and levator costae

muscles in the rib cages of human [12] and dogs [11], and explained the obtained rib motion with the original 2-dimensional Hamberger theory. Unfortunately, Loring had not considered the influence from the tissue deformation and distribution of the moment during the intercostal muscles contraction.

On the other hands, by applying external force on the ribs, the experiments resulted a hypothesis that the compliances of the ribs could determine the rib displacement generated by the intercostal muscle contraction, that in the end-expiratory lung volume the ribs could be displaced cranially more easily than caudally whether by the external or internal intercostal muscles [36]. It also means that the mechanical action of the intercostal muscles could also be covered and influenced by the compliances of the ribs. Unfortunately, there has been no study that selectively activates the intercostal muscles and simultaneously eliminates the compliance of the costovertebral and interchondral joints during experiments.

This study aims to investigate the mechanical action of the intercostal muscles that what rib motion can be generated by the contraction of the intercostal muscles and why these motions are happened. By using FEA, we consider not only the rigid rib rotation but also the rib and costal cartilage deformation and simultaneously eliminate the influence from the compliance of the costovertebral and interchondral joints during the intercostal muscle contraction. Considering the tissue deformation additionally lets us understand why the soft costal cartilages gradually run obliquely in the caudal direction and keep a right angle with the ribs in human trunk.

## **2.1 Methods**

### **2.1.1 Finite element model of chest**

Based on a voxel data set of the chest which was segmented from CT slices of a male volunteer to be used in the simulation of the electrophysiological activity of the heart [46], a 3D reconstruction of the sternum, rib, vertebrae, intercostal muscles, diaphragm, heart and lungs was performed and rendered to form STL format data. Since it is difficult to segment the intercostal muscles from CT slices, the 3D models of the intercostal muscles and diaphragm were constructed by referencing an anatomy textbook [47]. The finite element meshes shown in Fig. 2-1, Fig. 2-2, and Fig. 2-3, consisting of 424,304 tetrahedra elements and 92,841 nodes, were then generated from the 3D models using mesh generation software ANSYS ICEM CFD (ANSYS, Inc.).

The fiber direction of the intercostal muscles was assigned based on human cadaver data obtained from Loring (personal communications, 2012), as shown in Fig. 2-4. For the diaphragm, we referenced an anatomy textbook [47] to determine the fiber direction, as shown in Fig 2-5. We assumed that the fiber distribution had a radial pattern from the central tendon to the bottom edge.

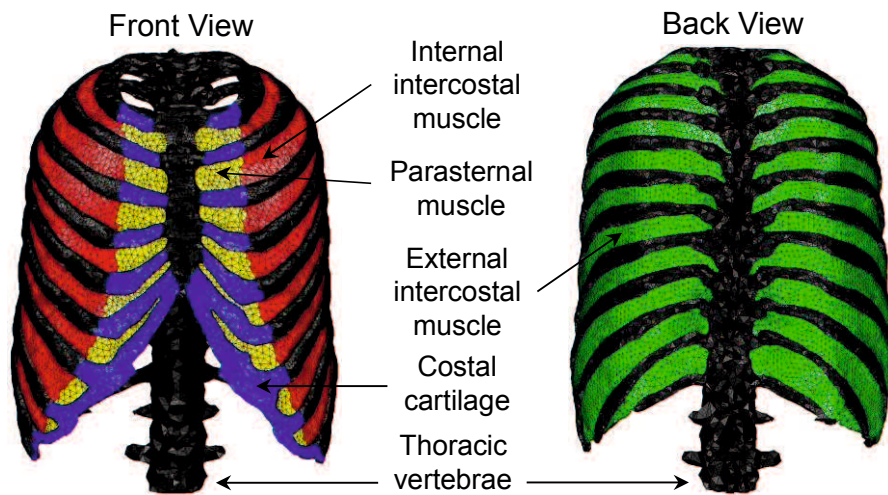


**Fig. 2-1** FEM model of the rib cage and intercostal muscles.

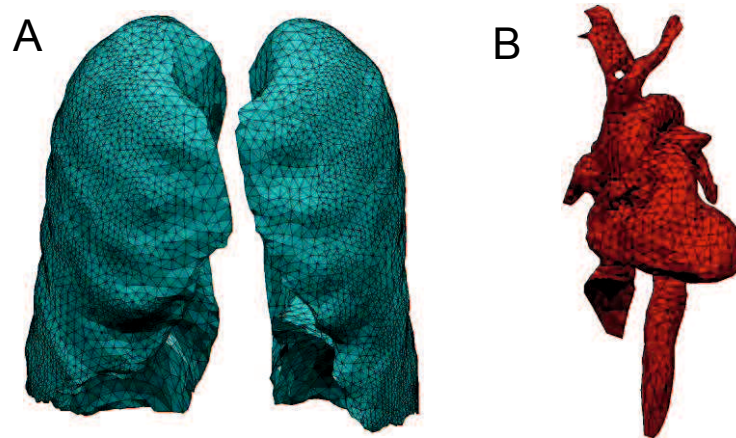


**Fig. 2-2** FEM model of lungs and heart A: lungs. B: heart.

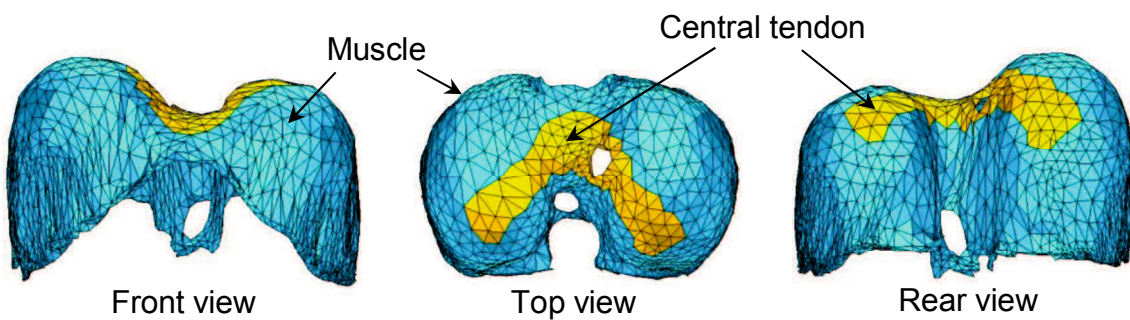


**Fig. 2-3** FEM model of diaphragm

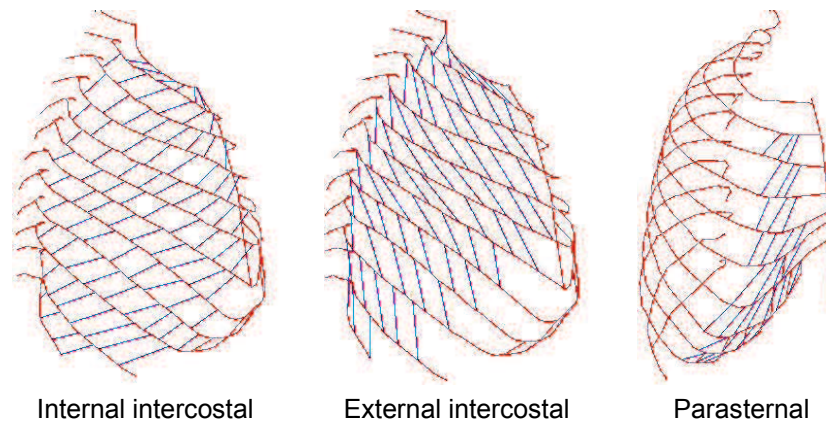


**Fig. 2-4** Fiber orientation of intercostal muscles measured by Loring [11].

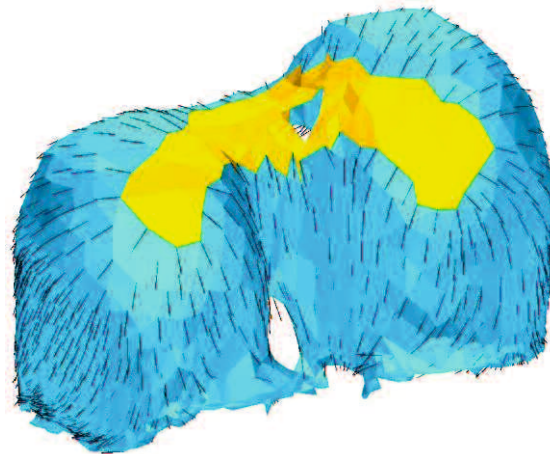


**Fig. 2-5** Fiber orientation of diaphragm

### **2.1.2 Transversely isotropic hyperelastic material model for respiratory muscles**

The intercostal muscles and diaphragm were considered to be incompressible hyperelastic materials. The function  $U_V = \det\mathbf{C} - 1$  represents the incompressible constraint and is enforced by the Lagrange multiplier  $\xi$ , where  $\det\mathbf{C}$  is the determinant of the right Cauchy-Green

tensor  $\mathbf{C}$ . To exclude the effect of the volume-changing deformation, the strain energy  $U_R$  was assumed to depend on the first reduced invariant of  $\mathbf{C}$ . This was defined as  $\bar{I}_1^C = J^{-2/3} \text{tr} \mathbf{C}$ , where  $J = \det \mathbf{F}$  denotes the determinant of the deformation gradient  $\mathbf{F}$ . By denoting  $\mathbf{t}$  as the external conservative force on the Neumann boundary, the total potential energy  $\Phi$  of the muscles can be formulated as a function of the displacement  $\mathbf{u}$  and Lagrange multiplier  $\xi$ , as shown in equation (2.1):

$$\Phi(\mathbf{u}, \xi) = \int_{\Omega} U_R d\Omega + \int_{\Omega} \xi U_V d\Omega - \int_{\partial\Omega} \mathbf{t} \cdot \mathbf{u} dS. \quad (2.1)$$

Given the principle of stationary potential energy, the variation in  $\Phi$  is equal to zero:

$$\delta\Phi = \int_{\Omega} \frac{\partial U_R}{\partial \mathbf{E}} \delta \mathbf{E} d\Omega + \int_{\Omega} \left( \xi \frac{\partial U_V}{\partial \mathbf{E}} \delta \mathbf{E} + \delta \xi U_V \right) d\Omega - \int_{\partial\Omega} \mathbf{t} \cdot \delta \mathbf{u} dS = 0, \quad (2.2)$$

where  $\mathbf{E}$  is the Green-Lagrange strain tensor. Thus, the weak form of the governing equation is as follows:

$$\begin{cases} \int_{\Omega} \delta \mathbf{E} \left( \frac{\partial U_R}{\partial \mathbf{E}} + \xi \frac{\partial U_V}{\partial \mathbf{E}} \right) d\Omega - \int_{\partial\Omega} \mathbf{t} \cdot \delta \mathbf{u} dS = 0 \\ \int_{\Omega} \delta \xi U_V d\Omega = 0 \end{cases} \quad (2.3)$$

The Lagrange multiplier corresponds to the hydrostatic pressure  $p$  by  $p = -2\xi$  [48]. In this study, the strain energy function  $U_R$  proposed by Martins et al. [49], [50] was introduced to model the skeletal muscles. This

model extends the traditional Hill's three-element muscle model to three dimensions. As shown in Fig. 2-6, the parallel element (PE) and series element (SE) are nonlinear springs which represent passive behaviour. The contractile element (CE) produces a contractile force when the muscle is excited.

The muscle force  $F$  can be assumed to be the sum of the forces in the PE and CE or SE:

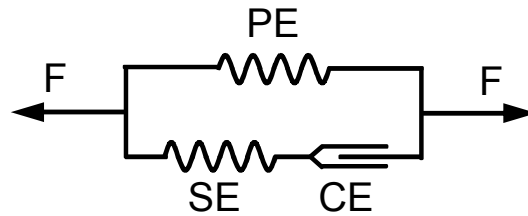


**Fig. 2-6** Hill's three-element muscle model

$$F = F^{\text{PE}} + F^{\text{SE}} = F^{\text{PE}} + F^{\text{CE}} . \quad (2.4)$$

Then, the nominal stress along the fibre direction  $T$  can be written as:

$$T = T^{\text{PE}} + T^{\text{SE}} = T^{\text{PE}} + T^{\text{CE}} . \quad (2.5)$$

The stress  $T^{\text{PE}}$  is defined as follows:

$$T^{\text{PE}} = T_0^{\text{M}} f_{\text{PE}}(\bar{\lambda}_f) \quad (2.6)$$

$$f_{\text{PE}}(\bar{\lambda}_f) = \begin{cases} 2aA(\bar{\lambda}_f - 1)e^{a(\bar{\lambda}_f - 1)^2} & , \text{for } \bar{\lambda}_f > 1 \\ 0 & , \text{otherwise} \end{cases} \quad (2.7)$$

where  $\bar{\lambda}_f$  is the stretch ratio in the fibre direction given by  $\bar{\lambda}_f = [J^{-2/3} \mathbf{C} : (\mathbf{N} \otimes \mathbf{N})]^{1/2}$ .  $\mathbf{N}$  is the initial direction of the muscle fibre,  $T_0^{\text{M}}$  denotes the maximum muscle nominal stress determining the maximum muscle contraction force,  $a$  and  $A$  are material constants [50], and  $f_{\text{PE}}(\bar{\lambda}_f)$  is the passive force-length relationship of the parallel element PE [50]. The stress  $T^{\text{CE}}$  is given by

$$T^{\text{CE}} = T_0^{\text{M}} f_{\text{CE}}(\bar{\lambda}_f) \alpha(t) \gamma, \quad (2.8)$$

where  $\gamma$  represents the muscle's activation level over a range from 0 to 1,  $\alpha$  represents the time dependence of the activation and for which the maximum value can be 1, and  $f_{\text{CE}}(\bar{\lambda}_f)$  is the active force-length relationship of the contractile element CE. In this study, this was considered to be the active force-length relationship for the muscle tissue. Fig 3 shows the experimental data for the active force-length relationship of the intercostal muscles and diaphragm as measured from an adult baboon [51].

According to the experimental data,  $f_{\text{CE}}(\bar{\lambda}_f)$  of the intercostal muscles can be formulated as

$$f_{CE}^{Int}(\bar{\lambda}_f) = \begin{cases} 0.85\bar{\lambda}_f - 0.48 & , \text{for } 0.6 \leq \bar{\lambda}_f < 0.7 \\ 2.43\bar{\lambda}_f - 1.59 & , \text{for } 0.7 \leq \bar{\lambda}_f < 0.8 \\ 3.32\bar{\lambda}_f - 2.30 & , \text{for } 0.8 \leq \bar{\lambda}_f < 0.9 \\ 3.10\bar{\lambda}_f - 2.10 & , \text{for } 0.9 \leq \bar{\lambda}_f < 1.0 \\ -2.30\bar{\lambda}_f + 3.30 & , \text{for } 1.0 \leq \bar{\lambda}_f < 1.1 \\ -3.20\bar{\lambda}_f + 4.29 & , \text{for } 1.1 \leq \bar{\lambda}_f < 1.2 \\ 0 & , \text{otherwise} \end{cases} \quad (2.9)$$

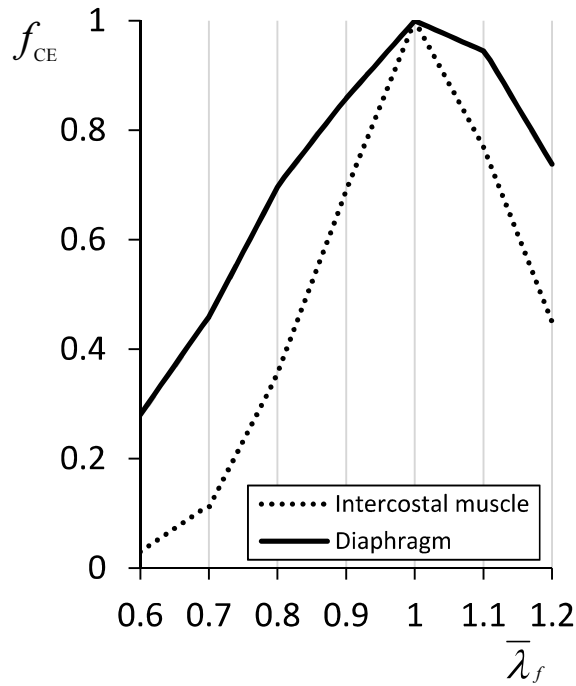


**Fig. 2-7** Active force-length relationship  $f_{CE}(\bar{\lambda}_f)$  of the diaphragm and intercostal muscles of an adult baboon

Then,  $f_{CE}(\bar{\lambda}_f)$  of the diaphragm can be formulated as

$$f_{CE}^{Dia}(\bar{\lambda}_f) = \begin{cases} 1.80\bar{\lambda}_f - 0.80 & , \text{for } 0.6 \leq \bar{\lambda}_f < 0.7 \\ 2.37\bar{\lambda}_f - 1.20 & , \text{for } 0.7 \leq \bar{\lambda}_f < 0.8 \\ 1.61\bar{\lambda}_f - 0.59 & , \text{for } 0.8 \leq \bar{\lambda}_f < 0.9 \\ 1.42\bar{\lambda}_f - 0.42 & , \text{for } 0.9 \leq \bar{\lambda}_f < 1.0 \\ -0.55\bar{\lambda}_f + 1.55 & , \text{for } 1.0 \leq \bar{\lambda}_f < 1.1 \\ -2.11\bar{\lambda}_f + 3.27 & , \text{for } 1.1 \leq \bar{\lambda}_f < 1.2 \\ 0 & , \text{otherwise} \end{cases} \quad (2.10)$$

The muscles were modelled as incompressible transversely isotropic hyperelastic materials for which the strain energy function can be written as follows:

$$U_R = U_I(\bar{I}_1^C) + U_f(\bar{\lambda}_f, \alpha, \gamma) \quad (2.11)$$

$$U_I = ce^{b(\bar{I}_1^C - 3) - 1} \quad (2.12)$$

$$U_f(\bar{\lambda}_f, \alpha, \gamma) = U_{PE}(\bar{\lambda}_f) + U_{CE}(\bar{\lambda}_f, \alpha, \gamma) \quad (2.13)$$

$$U_{PE}(\bar{\lambda}_f) = T_0^M \int_1^{\bar{\lambda}_f} f_{PE}(\lambda) d\lambda \quad (2.14)$$

$$U_{CE}(\bar{\lambda}_f, \alpha, \gamma) = T_0^M \int_1^{\bar{\lambda}_f} f_{CE}(\lambda) \alpha(t) \gamma d\lambda, \quad (2.15)$$

where  $U_I$  and  $U_f$  are the strain energies stored in the isotropic hyperelastic matrix and muscle fibre, respectively, and  $c$  and  $b$  are material constants. For an incompressible hyperelastic material, by

denoting  $p$  as the hydrostatic pressure, the second Piola-Kirchhoff stress tensor  $\mathbf{S}$  can be derived as follows:

$$\begin{aligned}
\mathbf{S} &= -p\mathbf{C}^{-1} + \frac{\partial U_R}{\partial \mathbf{E}} = -p\mathbf{C}^{-1} + \frac{\partial U_I}{\partial \bar{I}_1^C} \frac{\partial \bar{I}_1^C}{\partial \mathbf{E}} + \frac{\partial U_f}{\partial \bar{\lambda}_f} \frac{\partial \bar{\lambda}_f}{\partial \mathbf{E}} \\
&= -p\mathbf{C}^{-1} + \left\{ bce^{b(\bar{I}_1^C-3)} \right\} \left( 2\mathbf{I} - \frac{2}{3}\bar{I}_1^C \mathbf{C}^{-1} \right) \\
&\quad + \left\{ T_0^M \left( f_{PE}(\bar{\lambda}_f) + f_{CE}(\bar{\lambda}_f) \alpha(t) \gamma \right) \right\} \left( \bar{\lambda}_f^{-1} (\mathbf{N} \otimes \mathbf{N}) - \frac{1}{3} \bar{\lambda}_f \mathbf{C}^{-1} \right) \quad (2.16)
\end{aligned}$$

The material parameters used for the intercostal muscles and the diaphragm were  $T_0^M = 0.3$  MPa [51],  $c = 0.009348$  MPa, and  $b = 1.4939$  MPa [52]. The Lamé parameters  $\mu$  and  $\lambda$  of the isotropic elastic model were 569.23 and 853.85 MPa, respectively for bone [11]; 65.38 and 98.08 MPa, respectively, for cartilage [11]; and 5.18 and 10.05 MPa, respectively, for tendons [13].

### 2.1.3 Simulation condition

The muscles activation were set at 0.5 ( $\alpha=1.0$   $\gamma=0.5$ ) to make the muscle forces be equivalent to approximately half of the maximal absolute force at optimal muscle length. The fiber direction of the intercostal muscles was assigned based on the human cadaver data from Loring [11], as shown in Fig. 2. All the degrees of freedom at the bottom of vertebra were fixed as displacement boundary condition, and the simulations were performed with a nonlinear finite element analysis program developed in-house.

In order to investigate how the intercostal muscle contraction moves the rib cage, we did not consider the influence from the other muscles in the

human trunk. This is because all of the respiratory muscles are inserted and acts on the rib cage, therefore the entire effect could be considered as the summation of those individual muscles. Moreover, because the compliance of ribs depends on the lung volume during breathing and influences the rib displacement generated by the intercostal muscle contraction [36], the compliance of the costovertebral joint was set at relatively small in order to eliminate the influence from the compliance of the costovertebral and interchondral joints and model a neutral position of the rib cage during breathing.

#### **2.1.4 Simulation procedure**

The theory of Hamberger has been used to explained rib motion for over two centuries and generally accepted. Recently, because this theory, however, had been questioned due to the experiments of measuring rib compliance with external forces [36] which indicated the ribs could move cephalad more easily than caudad at end-expiratory lung volume and hypothesized that different rib moving directions are mainly caused by the distribution of the rib compliance in cranial and caudal direction throughout the rib cage, and not mainly relate to the torques around the spinal joints generated by the different fiber orientation of internal and external intercostal muscles as described in the theory of Hamberger. Therefore, we activated the intercostal muscles in a single interspace located in the middle of the rib cage in order to obtain the rigid rib rotation as described in the 2-dementional model by Hamberger.

Obtained rib rigid rotation is generated by the moment around the spinal joints due to the different fiber directions of the internal and external

intercostal muscles. Therefore, we virtually changed the fiber direction of the intercostal muscles to along the craniocaudal direction that the moment for rib rotation becomes zero to obtain the relationship between the rigid rotation and deformation of the ribs under the contracting forces of the intercostal muscles.

As De Troyer et al. [37] pointed out, the moment for rib rotation distributes along curved adjacent two ribs from dorsal to ventral portion of the rib cage and its direction also revised around the costochondral articulations. Therefore, from obtained relationship of between the rigid rotation and deformation of the ribs, the rib deformations caused by different intercostal muscles along the curved ribs also could be critical. For that reason, we individually activated the intercostal muscle groups from dorsal to ventral portion of the rib cage, and explained the mechanisms when the ribs were simultaneously rotated and deformed by different intercostal muscles throughout the rib cage.

After confirmed the partial mechanical action of the intercostal muscles, in order to investigate the net effect for entire intercostal muscles, we activated entire inspiratory and expiratory intercostal muscles and reproduced inspiratory and expiratory chest movements as observed clinically.

## **2.2 Results**

### **2.2.1 Rib movement generated by intercostal muscles in a single interspace**

The external and internal interosseous intercostal muscles in the interspace between rib 5 and 6 were activated. As the simulation results shown in Fig. 2-8-A, three points a, b and c in the rib cage were plotted for the comparison of the rib movement. Point a is at the middle of the sternum, point b and c locates at the lateral extremes of ribs 5 and 6. If the cranial direction is positive, the cranial displacement of point a was 0.2mm and points b and c were -0.3mm and 1.0mm, respectively, for the contraction of external intercostal muscles. Fig. 2-8-B shows the deformation for the contraction of internal interosseous intercostal muscles, the cranial displacement of point a was -0.3mm and points b and c were -0.8mm and 0.3mm, respectively. The results shows the external and internal intercostal muscles could rotate the sternum and ribs cranially and caudally, respectively.

### **2.2.2 Deflection of ribs during muscle contraction**

When the moment for rib rotation become zero, as expected, we obtained nearly the same two deformation results for the external and internal interosseous intercostal muscles, and one of them is shown in Fig. 2-8-C. The cranial displacement of point a was 0.05mm and points b and c were -1.0mm and 2.0mm, respectively. The adjacent two ribs 5 and 6 were prominent bent and moved more close to each other than during the contraction of external and internal intercostal muscles.

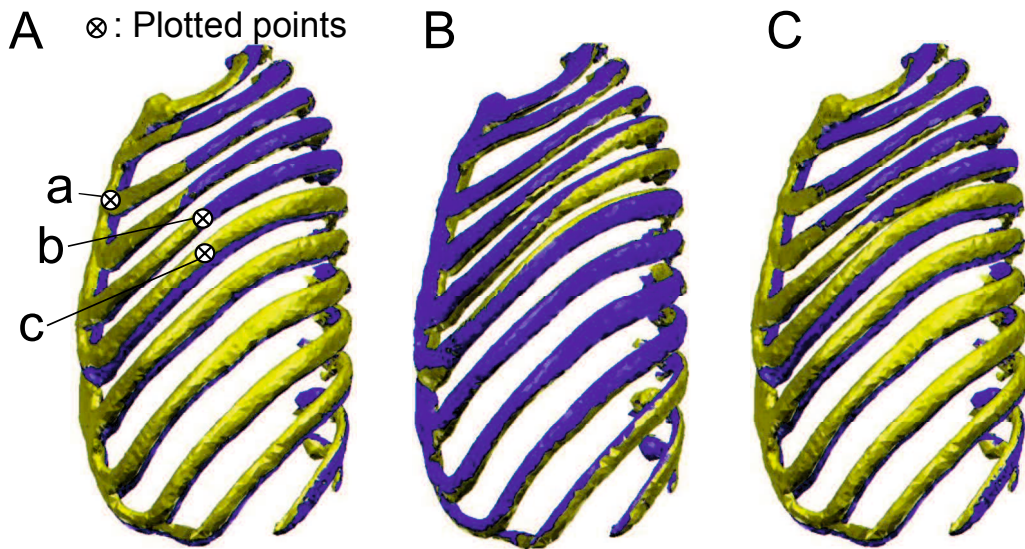


**Fig. 2-8** The rib movements due to the contraction of the external and internal interosseous intercostal muscles in one interspace locating between the rib 5 and 6 (Amplification factor 3.0; before muscle contraction: blue; after muscle contraction: orange). A: The lateral view of the rib movement caused by the external intercostal muscles. B: The lateral view of the rib movement caused by the internal interosseous intercostal muscles. C: The lateral view of the rib movement when the muscle fibers were artificially oriented in craniocaudal direction.

### 2.2.3 Rib movement generated by individual intercostal muscle

The rib rotation axes determine the rib rotation directions that upper ribs do the pump-handle motion (Fig. 2-9-A) and the lower ribs perform the bucket-handle motion (Fig. 2-9-B) [45]. In addition, the direction of the costal cartilage gradually shifts to oblique and nearly perpendicular to the

ribs, and our result illustrates this right angle in the costochondral articulations, as shown in Fig. 2-9-B, has a predominant function on the rib displacement during breathing. Hence, in order to explain the detailed mechanism later, first we distinguished the upper and lower ribs from anatomical structures.

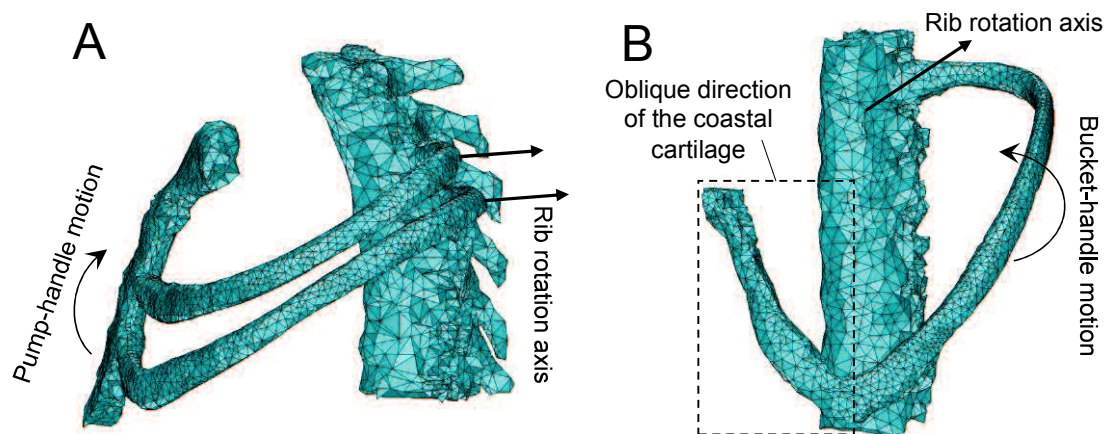


**Fig. 2-9** Different motions and structures of the upper and lower ribs. A: The upper ribs. B: The lower ribs.

The ribs was further differentiated into 3 portions as shown in Fig. 2-10-A, according to the distribution of moment along curved ribs around the spinal joints for rib rotation as shown in Fig. 2-10-B. Portion 1 has large moment and portion 2 has relative small moment. Regarding the separation for portion 3, because the direction of the moment is reversed around the costochondral articulations, therefore the mechanical action is also different between portion 2 and 3, as pointed out by De Troyer et al [37], [40]. This theory is the extended version of the Hamberger 2-demontional model in order to consider the influence from 3-demontional curved ribs on variation

of moment difference about two adjacent ribs, and concretely explained by De Troyer et al. [37], [40].

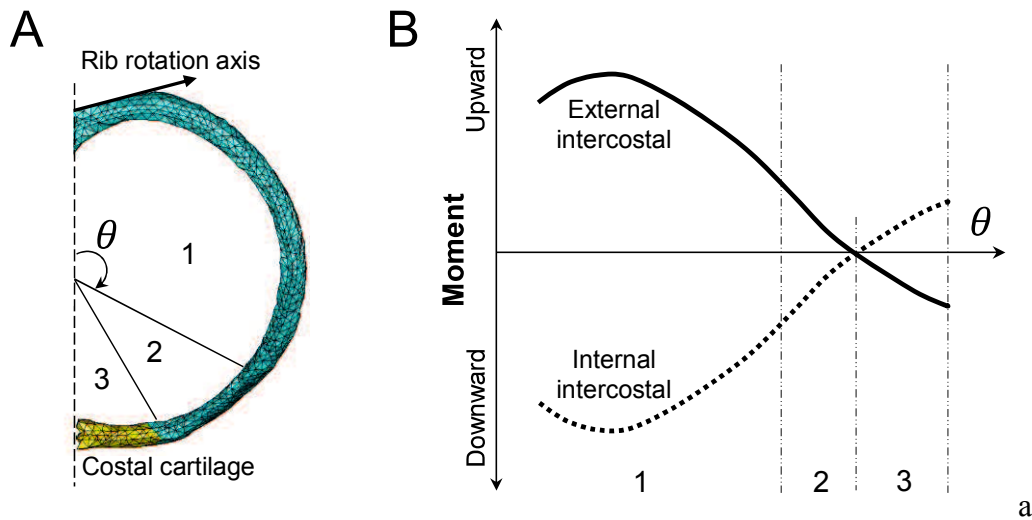


**Fig. 2-10** Portion 1, 2 and 3 divided according to the distribution of moment along curved ribs studied by De Troyer et al. [37]. A: Location of portion 1, 2 and 3. B: Distribution of moment.

In order to activate the intercostal muscles from dorsal to ventral portion, as Fig. 2-11 and Fig. 2-12 shows, we properly separated both the internal intercostal (Fig. 2-11) and external intercostal (Fig. 2-12) muscles to 8 fragments, and the angle  $\theta$  of each fragment is approximately 20 degrees from the center of the body. For visualizations, different colors were adopted for each muscle fragment, and fragments 1 to 8 were assigned from dorsal extremes to ventral extremes of the intercostal muscles.

For discussing the rib motion caused by these 8 fragments of internal and external intercostal muscles, as shown in Fig. 2-11 and Fig. 2-12, we selected the points at the middle of the sternum and the lateral extremes of

ribs from rib 1 to rib 10 as landmarks for representing rib motion. In addition, the displacements at the landmarks were normalized by the magnitude of the plotted sternum displacement for easier to assess, therefore the plotted sternum displacement reached -1 and 1 for the internal intercostal and external intercostal muscles, respectively.

During activating the internal intercostal muscles from fragments 1 to 8, the caudal displacement of the sternum gradually increased from fragments 1 to 5 and decreased from fragments 5 to 8, as shown in Fig. 2-13. For the upper rib 1 to 5, as shown in Fig. 2-14, the caudal displacement of rib 1 varied similarly to the displacement of the sternum in Fig. 2-13. The caudal displacement of ribs from 2 to 5 reached the maximal value between fragments 3 and 4, after that the caudal displacement gradually became smaller and reversed to cranial displacement between fragments 5 and 6, reached largest cranial displacement at fragment 7. For the lower rib 6 to 10, as Fig. 2-15 shows, the caudal displacement reached the maximal value between fragments 2 and 3, after that the caudal displacement gradually became smaller and reversed to cranial displacement between fragments 3 and 6, then decreased to fragment 8. These results illustrate that large downward rib and sternum displacements were happened during the contraction of the internal intercostal muscles in portion 1 of the rib cage. Some reversed rib displacements were generated by the internal intercostal muscles in portion 2 and 3 of the upper and lower rib cage, especially around the costochondral articulations. Therefore, it implies the mechanism is different between the portion 1, 2 and 3 of the rib cage.

Regarding the movements generated by the fragments of the external intercostal muscles, the cranial displacement of the sternum reached -1 at

fragment 5 and gradually decreased to 0.5 at fragment 8, as shown in Fig. 2-16. For the upper rib 1 to 5, as shown in Fig. 2-17, the cranial displacement of rib 1 varied similarly to the displacement of the sternum in Fig. 2-16. The cranial displacement of ribs from 2 to 5 reached the maximal value at fragment 4, after that the cranial displacement gradually became smaller and reversed to caudal displacement between fragments 5 and 6, reached largest caudal displacement at fragment 8. For the lower rib 6 to 10, as Fig. 2-18 shows, the displacement retain almost cranial, and the displacement of each rib first increased along with the fragment changed and then gradually decreased, after that the cranial displacement turned to increase again and then decreased from around fragment 6. These results illustrate that upward rib and sternum displacements were happened during the contraction of the external intercostal muscles not only in portion 1 but also in portion 2 of the rib cage. However, revised rib displacements occurred in the upper rib cage, and the two times increases of cranial displacement in the lower rib cage implies the mechanisms are different between the intercostal muscles in portion 1 and 2.

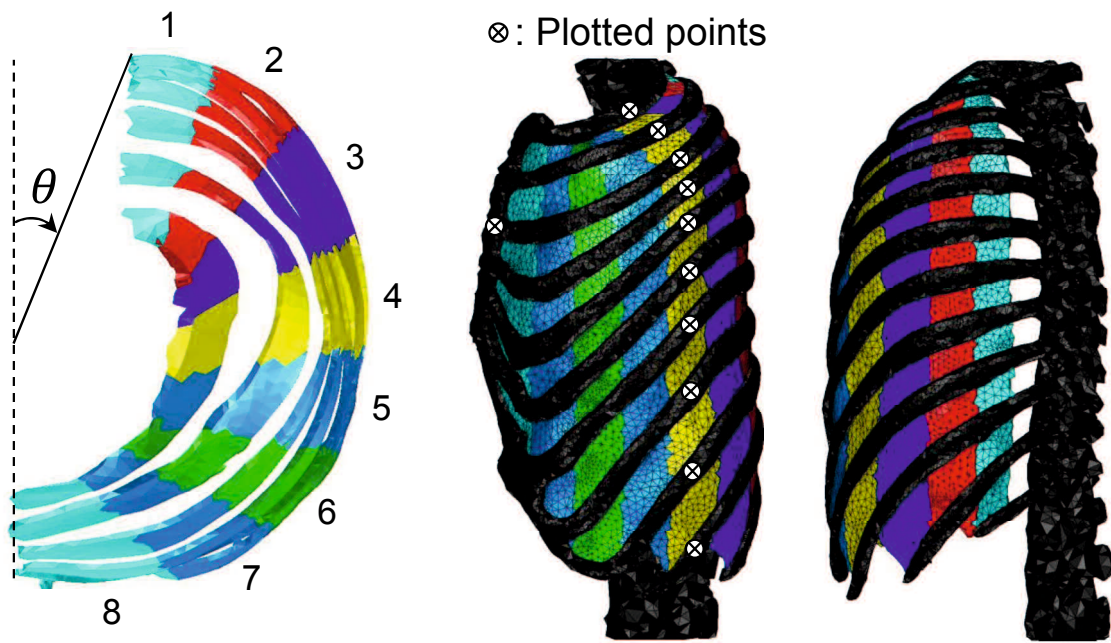


**Fig. 2-11** The fragments of the internal intercostal muscles.

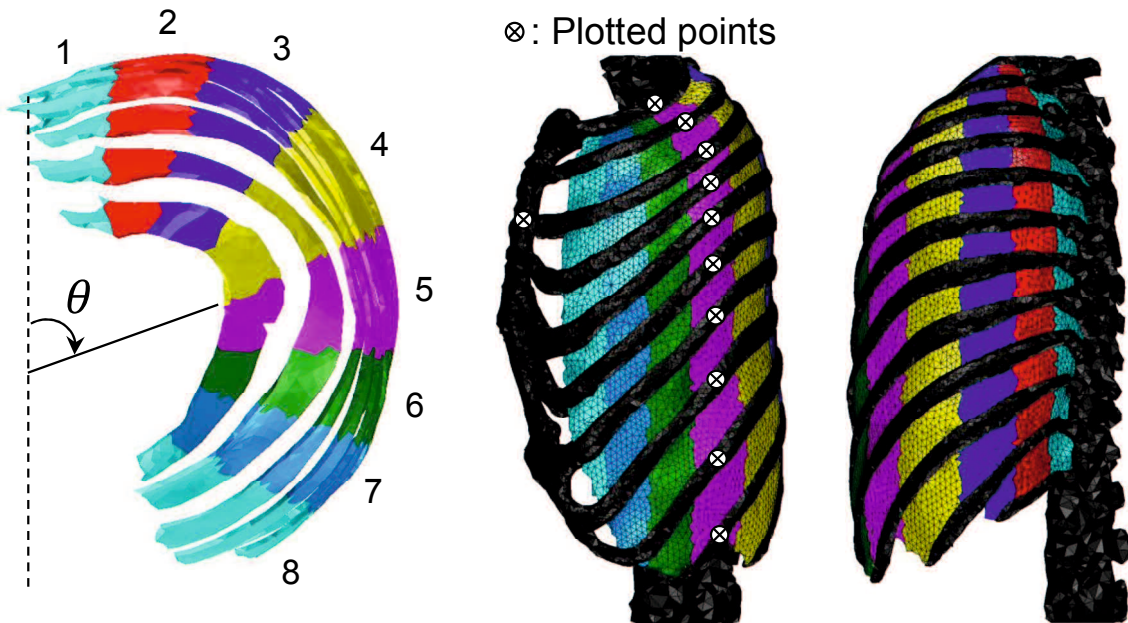


**Fig. 2-12** The fragments of the external intercostal muscles.

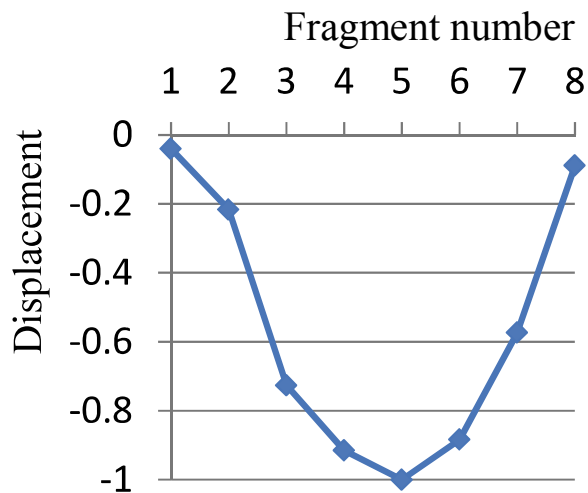


**Fig. 2-13** The normalized displacement of the sternum generated by separate fragments of the internal intercostal muscles (The horizontal axis shows number of the separate fragments, and the vertical axis shows normalized cranial displacement).

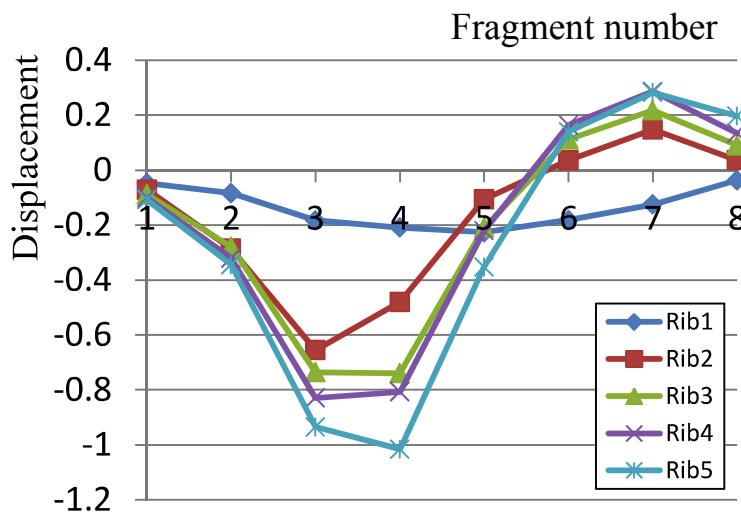


**Fig. 2-14** The normalized displacement at lateral extremes of the ribs from rib 1 to 5 generated by separate fragments of the internal intercostal muscles (The horizontal axis shows number of the separate fragments, and the vertical axis shows normalized cranial displacement).

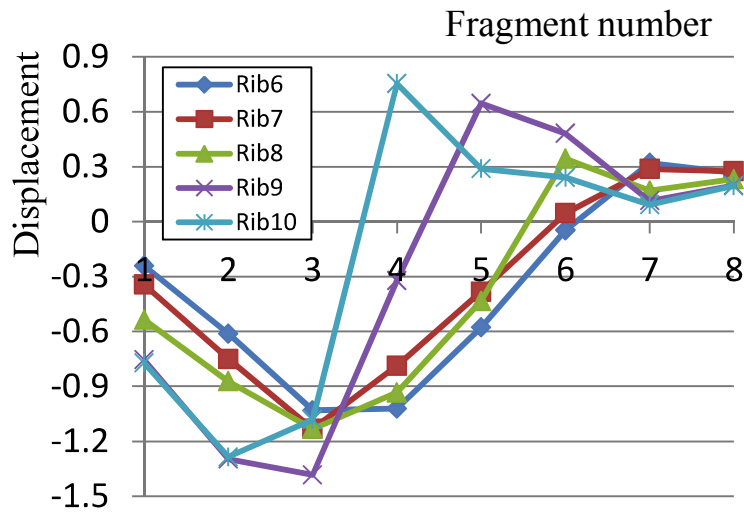


**Fig. 2-15** The normalized displacement at lateral extremes of the ribs from rib 6 to 10 generated by separate fragments of the internal intercostal muscles (The horizontal axis shows number of the separate fragments, and the vertical axis shows normalized cranial displacement).

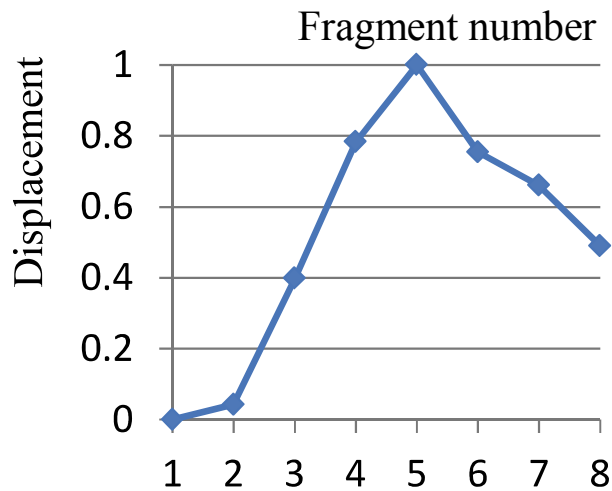


**Fig. 2-16** The normalized displacement of the sternum generated by separate fragments of the external intercostal muscles (The horizontal axis shows number of the separate fragments, and the vertical axis shows normalized cranial displacement).

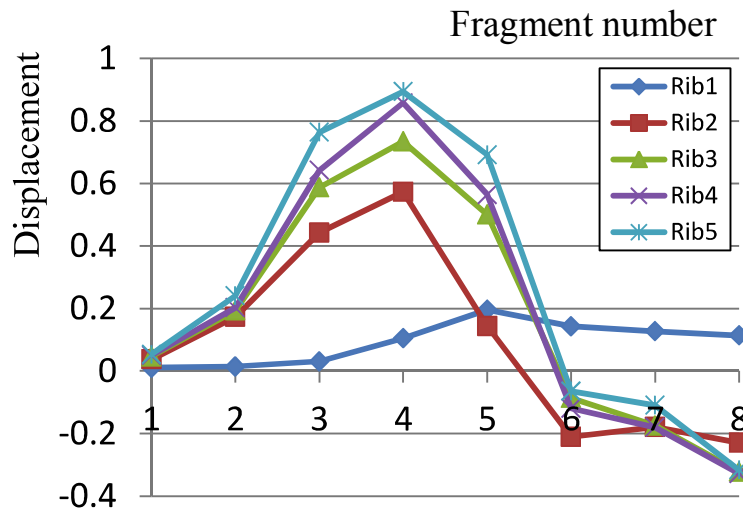


**Fig. 2-17** The normalized displacement at lateral extremes of the ribs from rib 1 to 5 generated by separate fragments of the external intercostal muscles (The horizontal axis shows number of the separate fragments, and the vertical axis shows normalized cranial displacement).

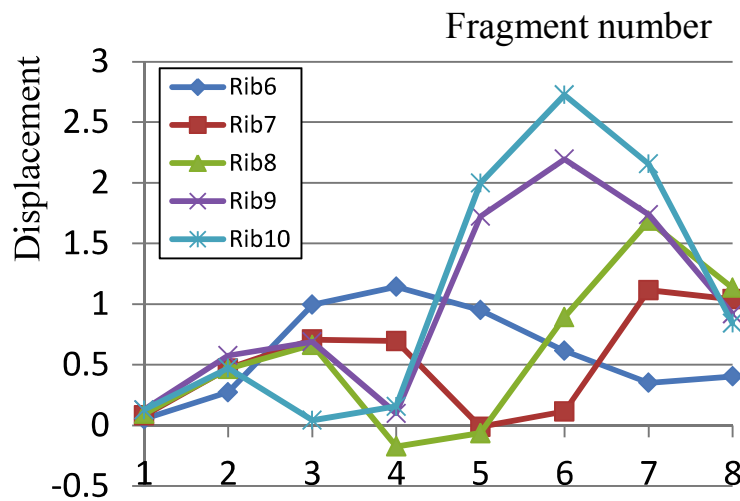


**Fig. 2-18** The normalized displacement at lateral extremes of the ribs from rib 6 to 10 generated by separate fragments of the external intercostal muscles (The horizontal axis shows number of the separate fragments, and the vertical axis shows normalized cranial displacement).

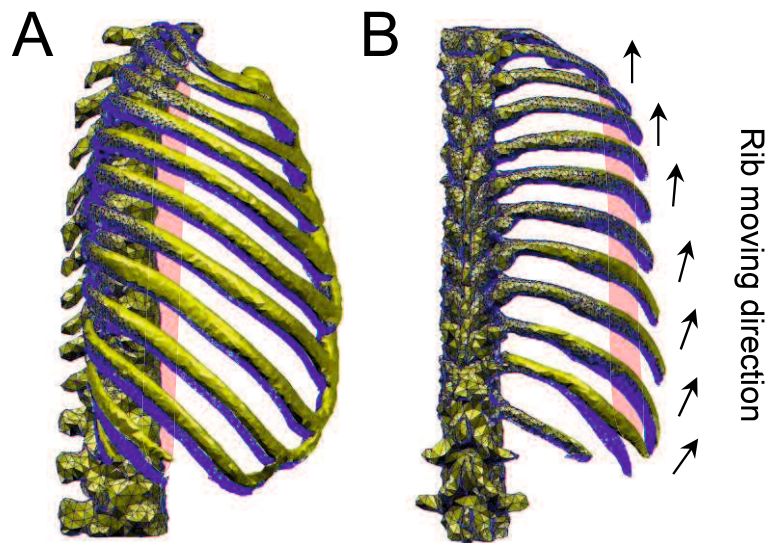


**Fig. 2-19** Rib motion caused by fragment 4 of external intercostal muscles in portion 1 (Amplification factor 4.0; blue: before muscle contraction; orange: after muscle contraction). A: Lateral view. B: Rear view.

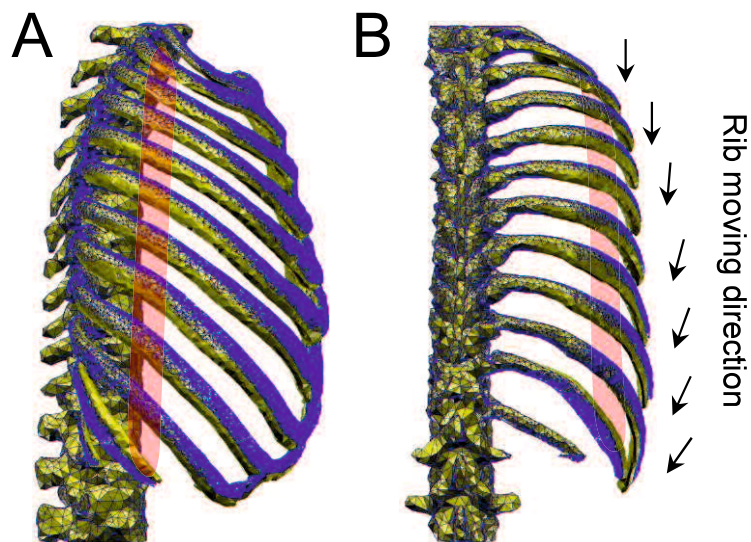


**Fig. 2-20** Rib motion caused by fragment 3 of internal interosseous intercostal muscles in portion 1 (Amplification factor 4.0; blue: before muscle contraction; orange: after muscle contraction). A: Lateral view. B: Rear view.

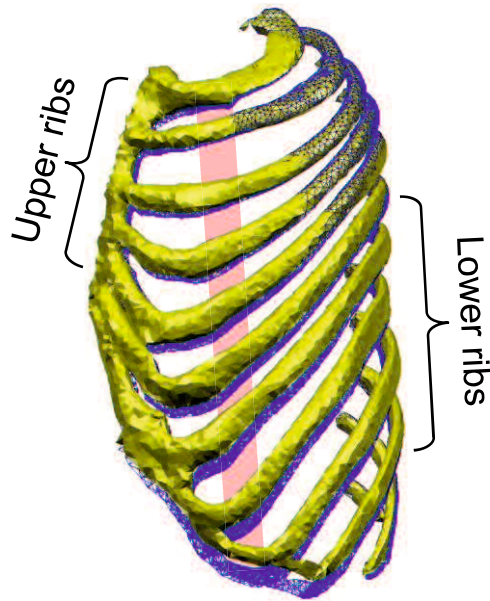


**Fig. 2-21** Rib motion caused by fragment 7 of external intercostal muscles in portion 2 (Amplification factor 4.0; blue: before muscle contraction; orange: after muscle contraction).

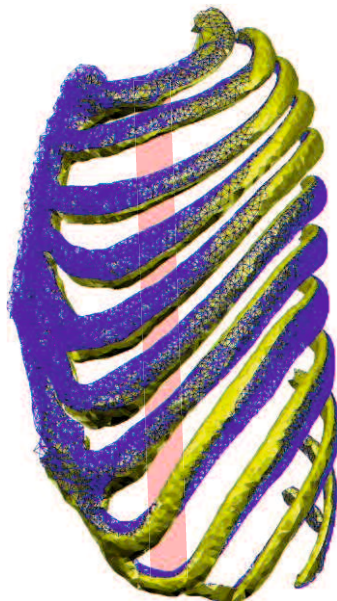


**Fig. 2-22** Rib motion caused by fragment 7 of internal intercostal muscles in portion 2 (Amplification factor 4.0; blue: before muscle contraction; orange: after muscle contraction).

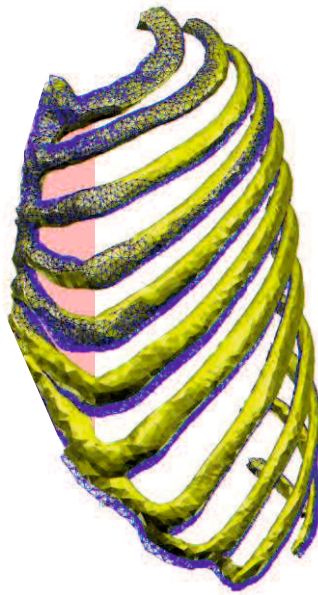


**Fig. 2-23** Rib motion caused by fragment 8 of internal intercostal muscles in portion 3 (Amplification factor 4.0; blue: before muscle contraction; orange: after muscle contraction).

For visualization, simulated rib motions caused by the intercostal muscles in portion 1, 2 and 3 were shown from Fig. 2-19 to Fig. 2-23. The red areas are the locations of the contracted muscle fragments. The external (fragment 4) and internal (fragment 3) intercostal muscles in portion 1 mainly caused inspiratory and expiratory rib rigid rotations, respectively, as shown in the lateral views of Fig. 2-19 and Fig. 2-20. The arrows in the rear views of Fig. 2-19 and Fig. 2-20, which illustrate the rib moving directions for visualization, show the rib rotation gradually shift from pump-handle to bucket-handle motion in caudal direction due to the rotation axes in the spinal as mentioned above, as observed clinically [45]. Fig. 2-21 shows the rib motion generated by the external intercostal muscles in portion 2 (fragment 7). We could observe the sternum was elevated and somewhat

caudal displacement was generated in the lateral portion of the upper ribs. Regarding rib motions caused by the internal intercostal muscles in portion 2 (fragment 7), Fig. 2-22 the sternum was lowered and the lateral portions of the ribs were elevated. The internal intercostal muscles in portion 3 (fragment 8) lowered the sternum and elevated the lateral portions of the ribs, as shown in Fig. 2-23.

#### **2.2.4 Rib movement generated by entire inspiratory and expiratory intercostal muscles**

After confirmed the partial mechanical action of the intercostal muscles, by activating entire inspiratory and expiratory intercostal muscles, we reproduced inspiratory and expiratory chest movements as observed clinically. Fig. 2-24 and Fig. 2-25 illustrate the inspiratory chest movement caused by contraction of the inspiratory muscles (external and parasternal intercostal muscles). The arrows show the rib rotation directions. We could observe the bucket-handle motion that the transverse diameter of the rib cage became larger from the front view in Fig. 2-24, and the pump-handle motion that the rise of the sternum was accompanied by the extending of the anteroposterior diameter of the rib cage from the lateral view in Fig. 2-25. The expiratory chest movement generated by activating the expiratory muscles (internal interosseous intercostal muscles) was shown in Fig. 2-26 and Fig. 2-27. The front view in Fig. 2-26 illustrates the bucket-handle motion that the rib cage was narrowed medially, and the lateral view in Fig. 2-27 shows the pump-handle motion of the ribs, shortening of the anteroposterior diameter of the rib cage.

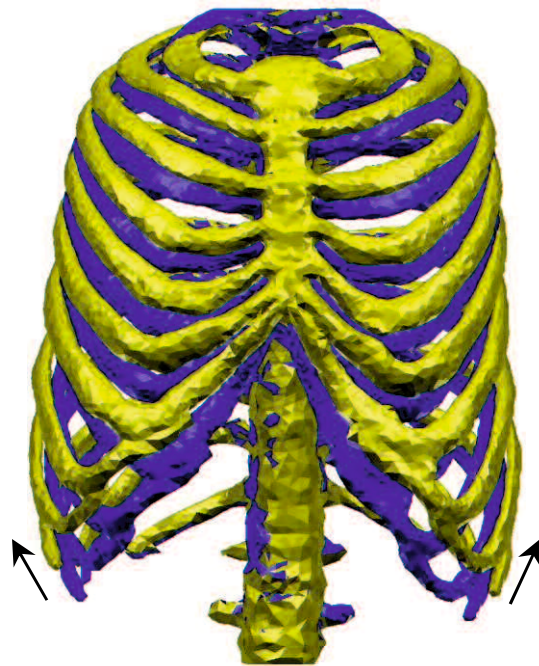


**Fig. 2-24** The front view of the inspiratory chest movement generated by the inspiratory intercostal muscles.

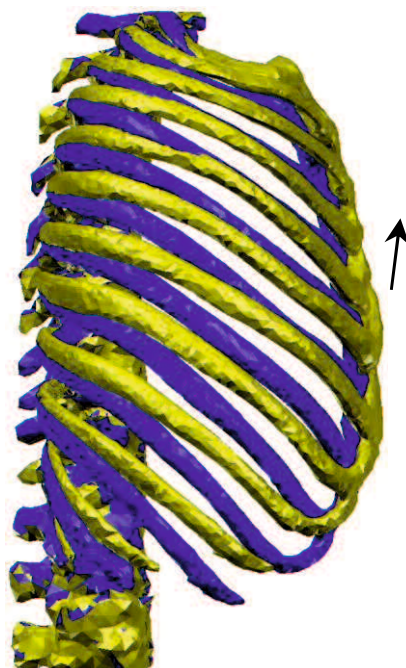


**Fig. 2-25** The lateral view of the inspiratory chest movement generated by the inspiratory intercostal muscles.

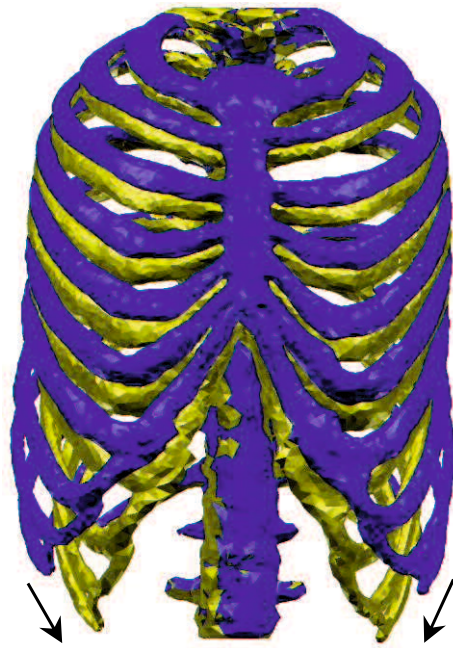


**Fig. 2-26** The front view of the inspiratory chest movement generated by the expiratory intercostal muscles.

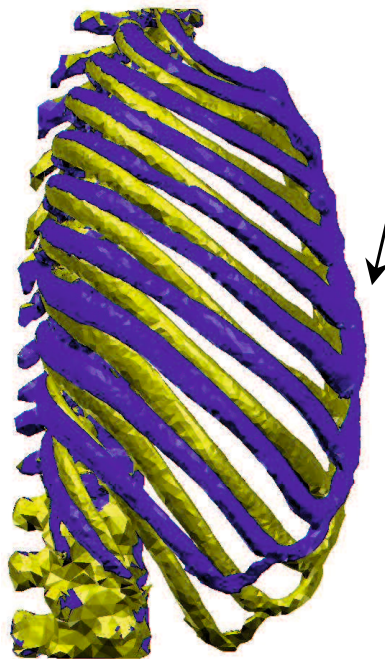


**Fig. 2-27** The lateral view of the inspiratory chest movement generated by the expiratory intercostal muscles.

## **2.3 Discussion**

### **2.3.1 Reproduction of the theory of Hamberger**

When the intercostal muscles contracted in a single interspace, for both the external and internal layer muscles, we obtained the ribs close to each other as obtained by De Troyer et al. [36] and Loring [12]. In addition, external intercostal muscles caused an inspiratory rib rotation due to the cranial displacement of sternum and ribs in the ventral region, and internal interosseous intercostal muscles generated an expiratory rib rotation due to caudal displacement of sternum and ribs in the ventral region. This cranial and caudal movement is consistent with the describing in the theory of Hamberger. Although some opposite displacement occurred in the dorsal-lateral region, the respective effect could be explained by the experiment results which concluded the displacement in the ventral region has a larger respiratory effect than in the dorsal region [37]. Therefore, although the rib compliance could determine the rib displacement, without considering the influence from the rib compliance, we concluded that the fiber orientation have a large significance on generating inspiratory and expiratory rib motions as the described by Hamberger.

### **2.3.2 Relationship between rigid rotation and deformation of ribs**

The theory of Hamberger had not considered the deformation of the ribs. The ribs are acted on the contraction of the muscle forces. After the muscle forces and moment are balanced, because the ribs are not pure rigid body as Fig. 2-8-C and also the experiment [36] and FEM simulation [12] show, the

ribs could be bent and deformed especially. Although the fiber orientation of the external and internal interosseous intercostal muscles caused upward and downward rib rotations, respectively, when we arterially changed the fiber orientation of the intercostal muscles, the craniocaudal fiber orientation did not generate rib rotation and just strongly bent the adjacent two ribs 5 and 6. Absolutely, the respiratory effect also could be ignored. That is when the rib rotation was not clearly generated, the rib deformed predominantly. Conversely, when the rib rotations were obviously happened, the rib deflection and deformation became inconspicuous.

It is easy to consider that, during the intercostal muscle contraction, if the torque generated by the muscle force is small for rib rotation, remained potential could bend and deform the bones. Also, if the deformation of the bones is not predominant, the contracting energy is utilized to resist the reaction force generated by the passive muscles and other tissues during rib rotation. Consequently, by considering the deformation of the rib cage during intercostal muscle contraction, the mechanical action of the intercostal muscles contraction on the rib cage is equivalent to the total action from the rib rotation and deformation. It is worth mentioning that this simple conclusion implies that the mechanical action of the intercostal muscle could shift between the rigid rotation and deformation. Notably, as shown in Fig. 2-10, the moment for the rigid rib rotation distributes along curved ribs and reaches zero around the costochondral articulations.

### **2.3.3 Action of intercostal muscle contraction on ribs**

In portion 1 of the rib cage where the muscles are close to the spinal joints and far from the cartilage, large moment caused dominant rib rigid rotation

during the intercostal muscles contraction. The respective effects are also consistent with those obtained with lung inflation experiment on human by De Troyer et al. [37]. However, regarding the intercostal muscles in portion 2 and 3, the moment for rib rotation is relatively small, therefore we could not ignore the deformations of the bones and cartilages happened in this region of the rib cage.

For the ease of explanation, the simulation results are shown in the middle of Fig. 2-28, and the mechanisms are shown in the left and right side of Fig. 2-28 with schematic diagram. Dotted lines illustrate the state after muscle contraction and the solid lines show the original shape of the rib cage. Red arrow shows the component of the muscle normal to the ribs.

The mechanism of external intercostal muscles locates in portion 2 was shown in Fig. 2-28-A. As mentioned in section 1.3.2, the mechanical action should be attributed as the summation action of the rib rotation and the deformation. For the rib rotations caused by the external intercostal muscles in portion 2, according to moment distribution in the Fig. 2-10-B, the moment could generate an upward rib rotation as the simulation result shows in Fig. 2-28-A. However, we could also observe some additionally caudal displacement in the lateral portion of the upper ribs (also as the displacement results illustrates in Fig. 2-17). That is the deformation part going to be explained in the left part of Fig. 2-28-A.

According to the anatomical structure of the upper ribs, because costochondral articulation is straight, the costal cartilage is normal to the sternum and the rib cage is symmetrical about the midsagittal plane, therefore the components of muscle forces going along the ribs could be balanced by the mirror symmetry components of muscle forces at the other

side of the rib cage. Furthermore, it is also because the normal muscle forces could mainly bend and deformed the ribs. Hence, in order to discuss the mechanism, the normal muscles forces were marked in the left part of Fig. 2-28-A with red arrows. When the muscle fiber contracts, we could observe the lateral portion of the upper rib is under a caudal muscle force and the sternal side is acted on a cranial muscle force. Therefore, during the upward rib rotation, the lateral portion of upper ribs was additionally bent caudally by the caudal muscle force. This deformation part also contributed to the cranial movement of the sternum during rib rigid rotation.

For the lower ribs, comparing with the upper ribs, the difference of the mechanism is caused by the oblique costal cartilages and the approximate right angle of the costochondral articulations. For the upper ribs, as explained above, the component runs along the ribs is balance through the sternum. However, for the lower ribs, because the costal cartilages goes obliquely, diverges under the sternum and the rib is approximately perpendicular to the costal cartilage. Therefore, the component runs along the ribs could not be balanced by the other side of the rib cage and just could be balanced by the reaction force from the abdominal issues as the blue arrow shows in 1-28 (because we want to investigate the rib motion caused by the intercostal muscles, therefore at this study we have not consider the abdominal wall, and the abdominal wall could be additionally considered after that [11]). Hence, the costochondral articulation could be spread and folded by the outward and inward muscle forces going along the ribs.

Detailed explanation for the lower ribs is shown in the right side of Fig. 2-28-A. The same as the upper ribs, the normal components of the muscles

caused the cranial displacement of the sternum and the caudal displacement of the lateral portion of the ribs. Regarding the component going along the ribs in the lower ribs, as the schematic diagram shows, this force running along the ribs could deform the costochondral articulation and rotate the costal cartilage in lateral-cranial direction. The costochondral articulation angle became large. The gradually increased cranial displacement in lateral portion of the ribs is because in this examination the separated fragments 8 gradually close to the costochondral articulation in caudal direction, therefore in caudal direction the moment gradually become small and the effect of deformation gradually became predominant, so that the lateral-cranial displacement of the ribs gradually reversed the caudal displacement to cranial. More importantly, although the moment for bucket-handle rotation in portion 2 is small, this deformation pattern of the costal cartilages could contribute to expand the chest in lateral direction as the respiratory effect of the bucket-handle rotation.

The mechanism during the internal intercostal muscle in portion 2 is shown in Fig. 2-28-B. According to the moment distribution of internal intercostal muscles in Fig. 2-10-B, the downward rib rotation could be generated as the simulation result shows in middle of Fig. 2-28-B. However, the cranial displacement was also obtained (Fig. 2-14 and Fig. 2-15) due to the deformation generated by the muscle forces. For the upper ribs (the left side of Fig. 2-28-B), the normal component to the rib of the muscles force generated the deformation that it pulled down the sternum and elevated the lateral portions of the ribs. For the lower ribs, as shown in the right side of Fig. 2-28-B, not only the normal components lowered the sternum and elevated the lateral portion of the ribs, but also the costal cartilage was

deformed by the component going along the rib in caudal direction and towards the midsagittal plane, so that the costochondral articulation angle became small, as the arrows of rib moving direction illustrates in Fig. 2-28-B. Furthermore, although the moment for expiratory rib rotation is small in portion 2, the midsagittal direction rotation of the costal cartilages and the bent ribs illustrate the reduce of the transverse diameter of the rib cage that is the deformation could contribute to the expiratory chest movement during internal intercostal muscle contraction in portion 2 of the rib cage.

Regarding the mechanical action of internal intercostal muscles in portion 3 (parasternal intercostal muscles), the mechanism is shown in Fig. 2-28-C. According the moment distribution of internal intercostal muscles in Fig. 2-10-B, the parasternal intercostal muscles could cranially rotate the ribs and sternum. However, because the deformation was happened, therefore the sternum was slightly lowered as the simulation result shows in the middle of Fig. 2-28-B. This is because the sternum and the ribs were under the caudal and cranial muscle force, respectively, as shown in the left side of Fig. 2-28-C. In addition, for the lower ribs, the mechanism is shown in the right side of Fig. 2-28-C. Because the muscles force acts on the costal cartilage, therefore the component normal to the costal cartilage pulls the costal cartilage in lateral-cranial direction. Hence, this deformation could contribute to expand the chest in lateral direction as the respiratory effect of the bucket-handle rotation. This mechanism could help to explain the experimental results that why the sternum moved caudally during the parasternal intercostal muscles contraction [40].

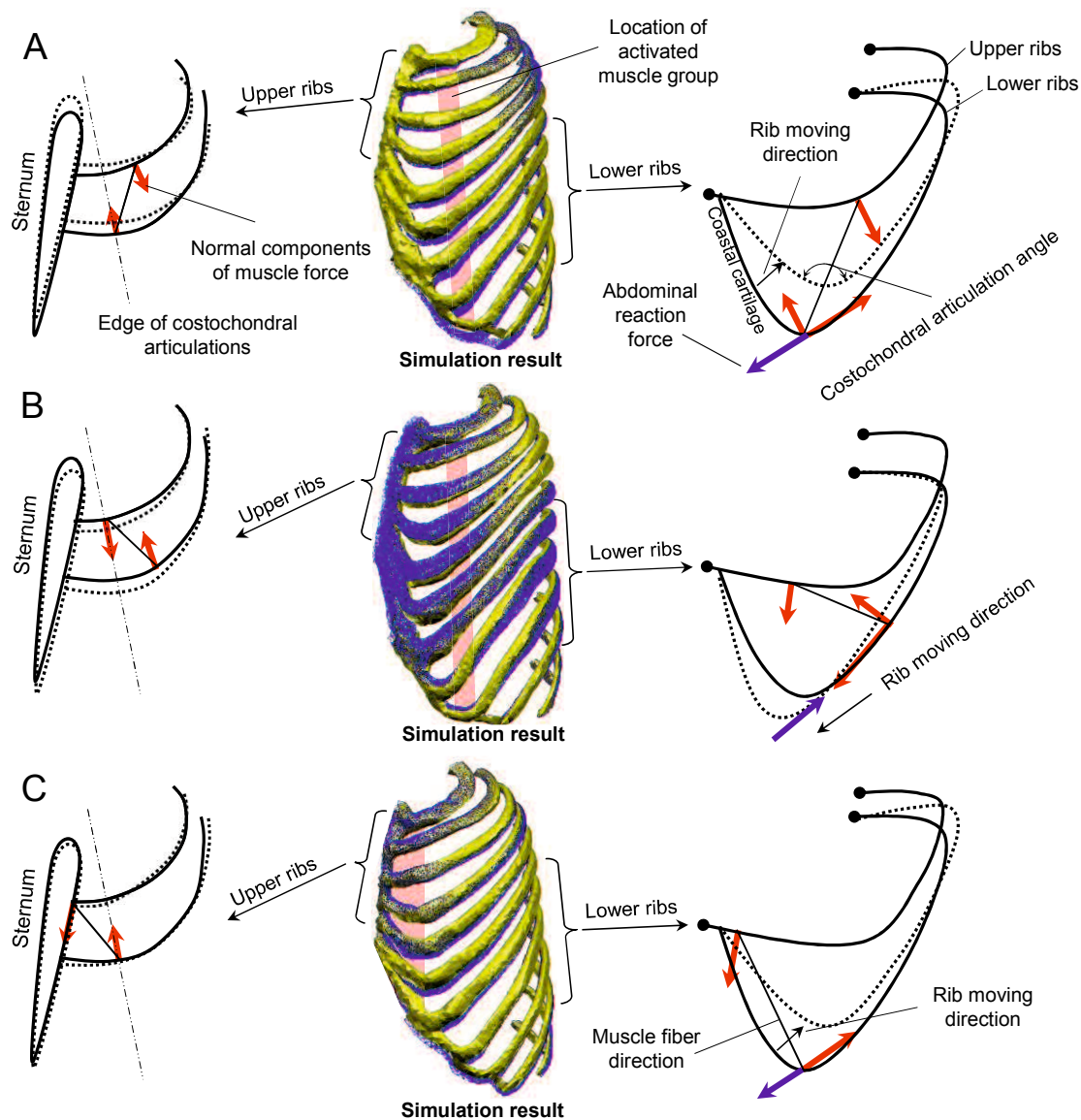


**Fig. 2-28** Mechanical actions of the intercostal muscles in portion 2 and 3 (solid line: before muscle contraction; dotted line: after muscle contraction) and simulated deformation results (blue: before muscle contraction; orange: after muscle contraction). A: Mechanical actions of upper (left side) and lower (right side) external intercostal muscles in portion 2. B: Mechanical actions of upper (left side) and lower (right side) internal interosseous intercostal muscles in portion 2. C: Mechanical actions of upper (left side) and lower (right side) parasternal intercostal muscles in portion 3.

### 2.3.4 The net effect during entire intercostal muscle contraction

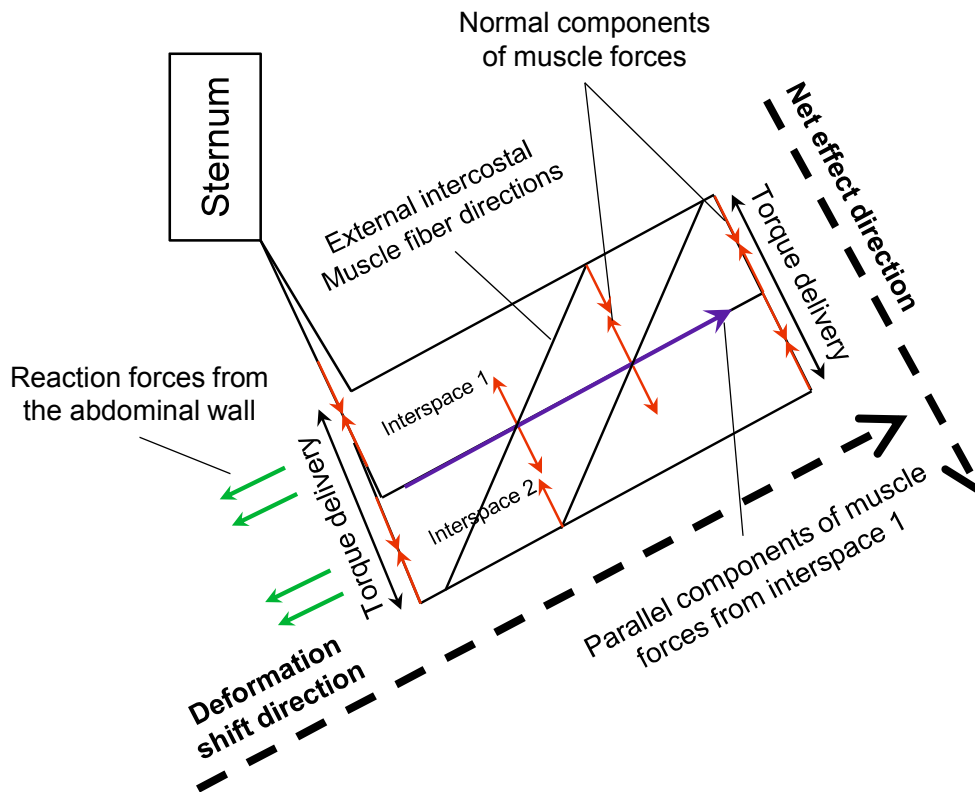


**Fig. 2-29** Deformation shift direction due to component going along the ribs of the muscle force and net effect direction due to the component normal to the ribs of the muscle force.

The net effect is important during the intercostal muscle contraction, as studied by Loring [12]. He described if just activate the muscles in a single interspace the ribs will be bent and move towards to each other, the same as our simulation results shows in Fig. 2-8. If activate entire intercostal muscles the rib could keep straight and inspiratory or expiratory rib rotation could be generated. The same as our simulation results, when we activated the entire inspiratory (external and parasternal intercostal muscles) and

expiratory intercostal muscles (internal intercostal muscles), we reproduced the inspiratory (Fig. 2-24 and Fig. 2-25) and expiratory (Fig. 2-26 and Fig. 2-27) movement of the rib cage, and the ribs keep straight and had not been bent. As the representative rib motions, the inspiratory and expiratory bucket-handle and pump-handle rotation of the ribs also could be observed. In this study, we studied two kinds of rib deformation patterns by individually activated the intercostal muscles from dorsal to ventral portion of the rib cage. One is caused by the normal component of the muscle force for both the upper and lower ribs, the other deformation pattern is happened concerning the costal cartilage for the lower ribs generated by the component of the muscle force running along the ribs. As Fig. 2-29 shows (the example of external intercostal muscles), the normal components of the muscle force in interspace 1 were balanced by the normal components in interspace 2 in net effect direction, therefore the ribs could not be bent during entirely activating intercostal muscles. This is the mechanism of the net effect. On the other hand, for the other deformation pattern happened in the costal cartilage caused by the ribs shift in the deformation shift direction as Fig. 2-29 shows, deformation about the middle rib generated by the parallel components of muscle forces in interspace 1 could not be balanced by the muscle force in interspace 2, and this deformation should be resisted by the reaction forces from the other issues in the trunk in the deformation shift direction. This is because, in deformation shift direction, if there is no abdominal reaction force as the simulation condition in this study, the muscle contraction force in interspace 1 could not influence the deformation result of interspace 2. Therefore, this deformation pattern could not generate net effects from the upper to lower ribs, and just could

be influenced by the reaction forces along the deformation shift direction such as the reaction force from the abdominal wall, as the green arrows illustrates in Fig. 2-29. More importantly, this deformation of the costal cartilage in the deformation shift direction could contribute to the expansion of lateral diameter and accompany with the bucket-handle rib rotation during human breathing, as shown in Fig. 2-24. It also indicated the way of energy stored in the costal cartilage during human breathing. Likewise, the internal intercostal muscles also could generate these two kinds of rib deformation patterns in the net effect direction and deformation shift direction.

According to the mechanism explained in Fig. 2-28 and Fig. 2-29, during the external and parasternal intercostal muscle simultaneous contraction, the muscles in portion 1 generate large inspiratory rib rotation and the muscles in portion 2 and 3 deform the costal cartilage with the muscle force going along the ribs in deformation shift direction. The elastic potential energy is restored in the costal cartilages after the external and parasternal intercostal muscles generate the inspiratory rib movement. After that, the elastic potential energy in the costal cartilage could contribute to expiratory process. Regarding the contraction of the internal interosseous intercostal muscles, the muscles in portion 1 generate large expiratory rib rotation and the muscles in portion 2 deform the costal cartilage with the muscle force going along the ribs in the opposite direction of the deformation shift direction, and the elastic potential energy is restored in the costal cartilages. After that, the elastic potential energy in the costal cartilage could contribute to inspiratory process.

From obtained rib movements, we could assess the respiratory effect for the intercostal muscles. In portion 1, the external and internal intercostal muscles have large inspiratory and expiratory effects, respectively. In portion 2, the anteroposterior and transverse diameter was largely increased and decreased by the external and internal intercostal muscles, respectively. Although somewhat caudal displacements were observed in the dorsal-lateral portion of the upper ribs, because the rib displacement has larger respiratory effects in ventral portion than the dorsal portion [37], therefore it indicated the external and internal intercostal muscles in portion 2 have inspiratory and expiratory effect, respectively. For the parasternal intercostal muscles in region 3, because the caudal displacement of the sternum was almost zero, and they generated an inspiratory upward and outward rib rotation, therefore it indicated the parasternal intercostal muscles have inspiratory respiratory effect. In summary, the external intercostal muscles have inspiratory effect throughout the rib cage. The internal interosseous and parasternal intercostal muscles have expiratory and inspiratory effects, respectively. These assessed respective effects have a good consistence with the findings by lung inflation experiment on human by De Troyer et al. [37].

## **2.4 Conclusions**

This study investigated the mechanical action of the intercostal muscles by attributing the rib motion to not only the rigid rotation but also the deformation of the ribs and costal cartilages. We concluded the mechanical actions of intercostal muscles could be classified with three portions throughout the rib cage. Especially for the portions where the intercostal

muscles have small moment for rigid rib rotation, analyzed results indicated the special shape of the costal cartilages running in the oblique directions could additionally assist to increase the inspiratory and expiratory effect for the rigid rib rotation during the intercostal muscles contraction and simultaneously store the elastic energy for the subsequent respiratory process when the intercostal muscles relax. These obtained detailed actions of the intercostal muscles on rib movement during breathing help us to reproduce the thorax deformation during human breathing.

# 3

## Simulation of thorax deformation by activating intercostal muscles and diaphragm

---

The deformation of the thorax significantly influences airflow in the lungs. After confirmed the action of the intercostal muscles and reproduced the rib movement caused by the intercostal muscle contraction, we focused on simulating the thorax deformation by simultaneously activated the intercostal muscles and diaphragm, which are the main muscles responsible for the thorax deformation during breathing.

Thorax deformation consists of the movements of the diaphragm and the rib cage, which mainly result from the contractions of the diaphragm and intercostal muscles during breathing [2]. Previous studies which used the finite element method (FEM) to simulate thorax deformation can be classified into two categories: (1) modelling respiratory muscles with beam elements [11], [16] and (2) representing the rib and diaphragm motions with a prescribed displacement or external load instead of muscle contraction [21], [23], [15]. From a biomechanical point of view, a three-dimensional continuum mechanical model of the muscles should be used to simulate the interaction between the muscles and organs inside the chest. Furthermore, physiologically unrealistic displacements and external loads cannot reasonably reproduce the biomechanical environment in the chest. Within the framework of continuum mechanics, a muscle is

modelled as an incompressible transversely isotropic hyperelastic material [50] such that the material response in the plane orthogonal to the direction of the muscle fibre is isotropic. However, to date, such material models have not been applied to the formulation of respiratory muscles for simulating thorax deformation.

To overcome the drawbacks faced by previous studies, in this study we set out to simulate the thorax deformation by modelling the respiratory muscles based on continuum mechanics and introducing muscle contractions. To reproduce the muscle contractions based on continuum mechanics, the same as investigating the action of the intercostal muscles in chapter 2, we also introduced a Hill-type transversely isotropic hyperelastic continuum material model which allowed the respiratory muscles to contract along the direction of the fibres with clinically measurable muscle activation. By applying an anatomical muscle fibre orientation and muscle activation to the respiratory muscles, we reproduced physiologically representative motions of the ribs and subsequently the diaphragm. Finally, by activating the inspiratory intercostal muscles and diaphragm simultaneously, we achieved reproduction of the thorax deformation during normal breathing, which we compared with four-dimensional computed tomography (4D-CT) images to validate the effectiveness of this approach.

## **3.1 Method**

### **3.1.1 Simulation condition**

Because the diaphragm comes into contact with and slides against the chest wall during breathing [13], a contact condition was applied between the

diaphragm and chest wall. All of the degrees of freedom at the bottom of the vertebrae were fixed as a displacement boundary condition. Abdominal pressure and pleural pressure were respectively applied to the lower surface of the diaphragm and inner surface of the thorax with linear variations from 0 to 2 kPa [16] and from -0.5 to -0.75 kPa [2] during normal quiet breathing. The time dependence of the activation  $\alpha(t)$  of the intercostal muscles and diaphragm was fitted to experimental data obtained from dogs during normal quiet breathing [53], as shown in Fig. 3-1.

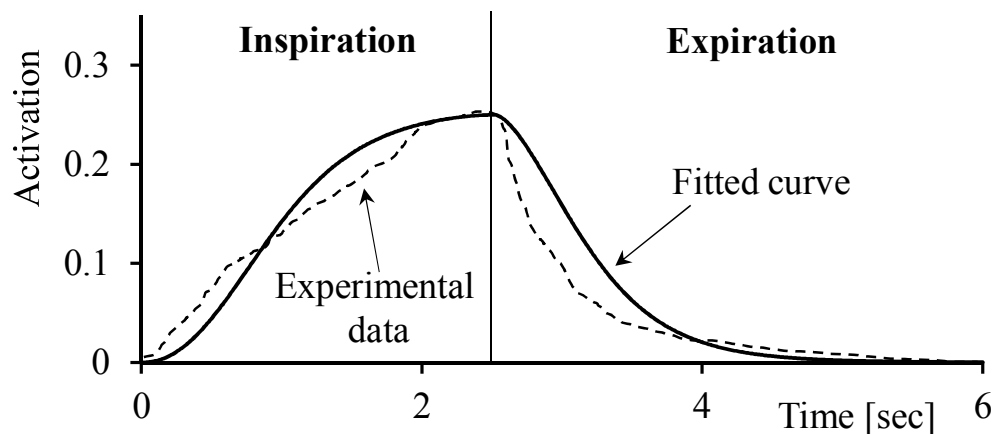


**Fig. 3-1** Time dependence of activation  $\alpha(t)$  of the diaphragm and intercostal muscles.

### 3.1.2 Simulation procedure

In this study, simulations were performed to examine and validate the introduced Hill-type transversely isotropic hyperelastic continuum skeletal muscle model for thorax deformation. First, we individually activated the intercostal muscles and diaphragm to reproduce representative motions of the ribs and the diaphragm according to physiology and clinical

observations. Then, we simultaneously activated the intercostal muscles and diaphragm in order to simulate the thorax deformation. Finally, the resultant thorax deformation was compared with 4D-CT data during normal quiet breathing. The data were collected at Tokuyama Central Hospital, Japan Community Healthcare Organization, based on the Declaration of Helsinki. The procedure was approved by the Ethics Committee of the hospital.

## **3.2 Results**

Based on the formulation given in the section entitled ‘Transversely isotropic hyperelastic material model of respiratory muscle’, the incompressible transversely isotropic hyperelastic material model was implemented in a nonlinear finite element analysis program developed in-house. The thorax deformation was simulated by using the FEM model presented in the section entitled ‘FEM model of thorax’.

### **3.2.1 Rib motion**

The intercostal muscles were activated based on the muscle activity distribution during inspiration and expiration to obtain the corresponding chest movements [1]. The parasternal intercostal muscles and external intercostal muscles were activated for the inspiratory chest movement, while the internal intercostal muscles were activated to reproduce the expiratory chest movement. For the parasternal muscles [1], the muscle activation reached a maximum near the sternum ( $\gamma = 1.0$ ) but decreased to zero in the lateral direction at the costochondral junctions. The largest muscle activation among the external intercostal muscles [54] occurred in the dorsal region of the interspace between ribs 1 and 2 ( $\gamma = 1.0$ ) and gradually decreased in the caudal and ventral directions through to the lower ribs. For the internal intercostal muscles [54], we activated the muscles in the lowest rib interspace with the largest activation ( $\gamma = 1.0$ ), while the activation gradually decreased in the cranial and ventral directions through to the upper ribs.

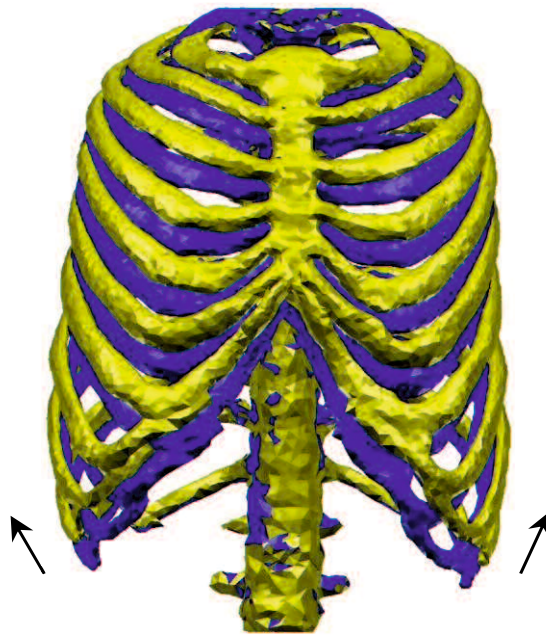


**Fig. 3-2** Front view of inspiratory rib motion generated by the intercostal muscles (The orange shape: after muscle contraction; the blue shape: before muscle contraction.).

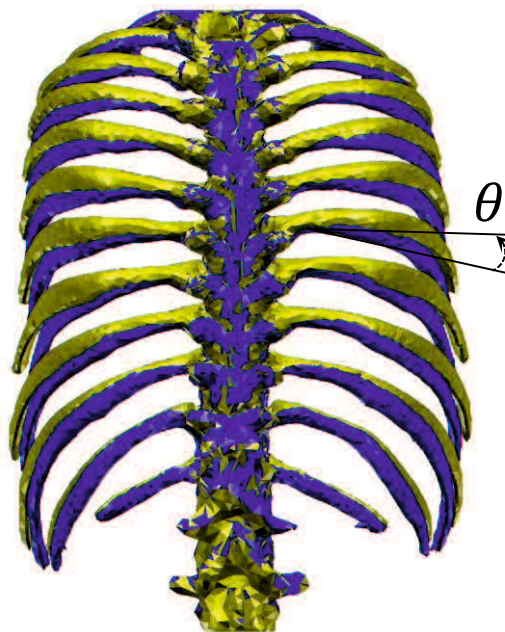


**Fig. 3-3** Rear view of inspiratory rib motion generated by the intercostal muscles (The orange shape: after muscle contraction; the blue shape: before muscle contraction.).

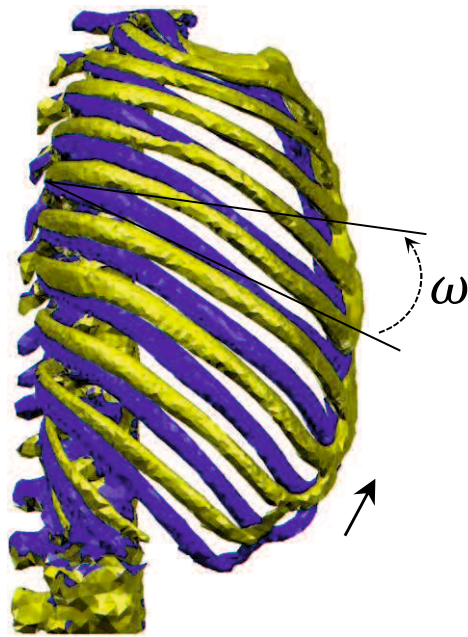


**Fig. 3-4** Lateral view of inspiratory rib motion generated by the intercostal muscles (The orange shape: after muscle contraction; the blue shape: before muscle contraction.).

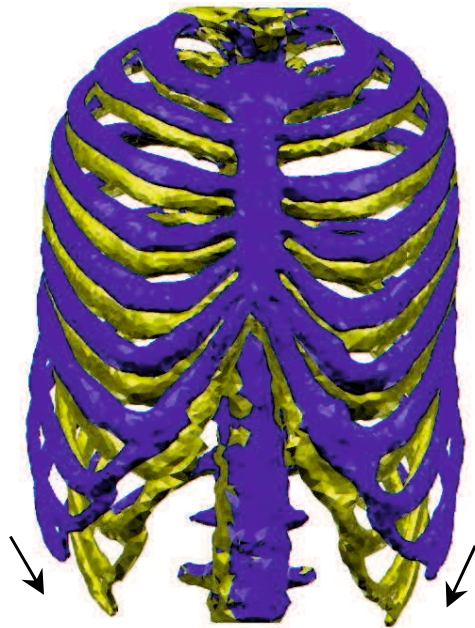


**Fig. 3-5** Front view of expiratory rib motion generated by the intercostal muscles (The orange shape: after muscle contraction; the blue shape: before muscle contraction.).

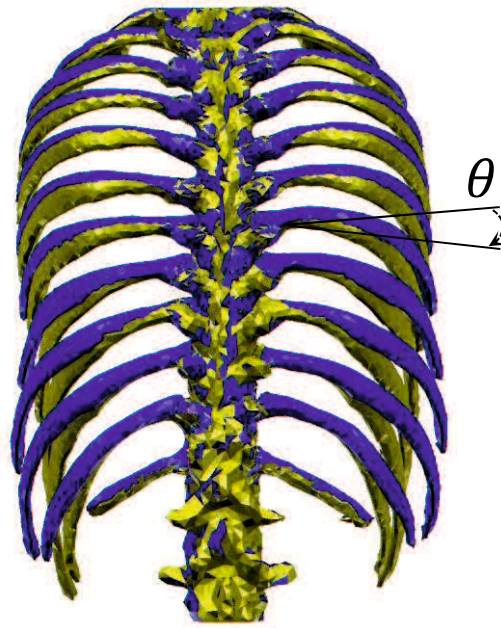


**Fig. 3-6** Rear view of expiratory rib motion generated by the intercostal muscles (The orange shape: after muscle contraction; the blue shape: before muscle contraction.).

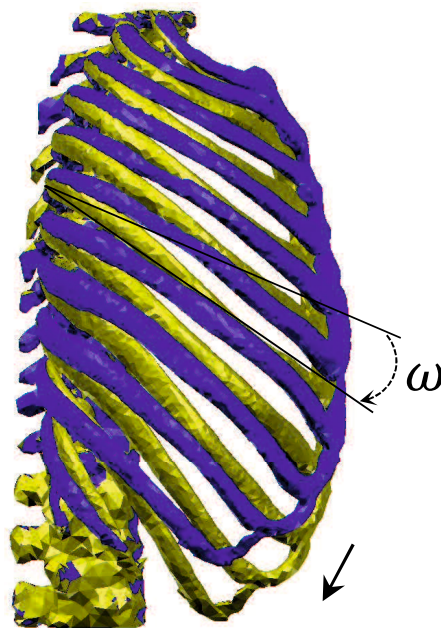


**Fig. 3-7** Lateral view of expiratory rib motion generated by the intercostal muscles (The orange shape: after muscle contraction; the blue shape: before muscle contraction.).

As a result, we obtained the inspiratory (Fig. 3-2, 3-3, 3-4) and expiratory (Fig. 3-5, 3-6, 3-7) movements of the rib cage. During inspiration, the front (Fig. 3-2) and rear (Fig. 3-3) views of the rib cage showed that the transverse diameter increased, especially for the lower ribs. The lateral view (Fig. 3-4) showed the extension of the anteroposterior diameter. These increases in the chest diameter demonstrated that the obtained chest movements were inspiratory. For the expiratory chest movements, the front views (Fig. 3-5 and Fig. 3-6) showed that the rib cage narrowed medially (i.e. transverse diameter decreased), particularly in the case of the lower ribs. The lateral view (Fig. 3-7) showed the decrease in the anteroposterior diameter. These decreases in the chest diameter demonstrated that the obtained chest movements were expiratory.

More importantly, among the inspiratory (Fig. 3-2, 3-3, 3-4) and expiratory (Fig. 3-5, 3-6, 3-7) chest movements, we observed representative rib motions which have been characterized physiologically. The arrows in Fig. 3-2 and Fig. 3-5 show the directions of the rib movements. The ribs moved like the handle of a bucket, which is known as the ‘bucket-handle motion’ in physiology. The arrows in Fig. 3-4 and Fig. 3-7 show that the ribs moved like the handle of an old-fashioned water pump, which is the source of the term ‘pump-handle motion’. The angle  $\theta$  shown in Fig. 3-3 and Fig. 3-6 is thus called the ‘bucket-handle angle’ of the rib, and the angle  $\omega$  shown in Fig. 3-4 and Fig. 3-7 is called the ‘pump-handle angle’ of the rib, as explained by Troyer et al. [38]. The angles  $\theta$  and  $\omega$  were measured for ribs 2–9 in a lung inflation experiment and were found to be equivalent to the inspiratory muscle contraction studied by Troyer et al. [38].

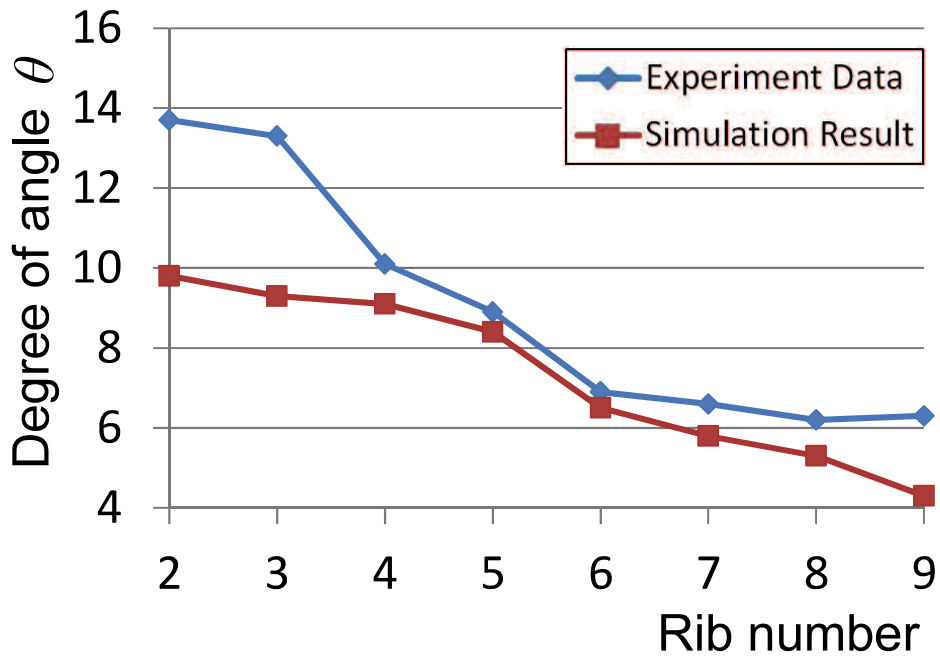


**Fig. 3-8** Comparison of simulated and experimental bucket-handle angle  $\theta$  during inspiratory chest movement

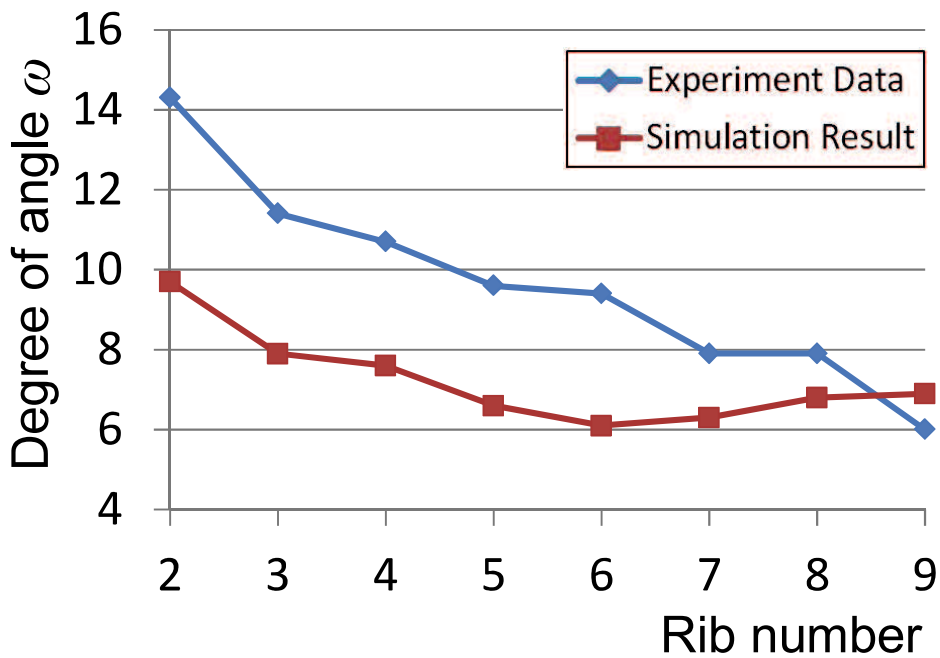


**Fig. 3-9** Comparison of simulated and experimental pump-handle angle  $\omega$  during inspiratory chest movement

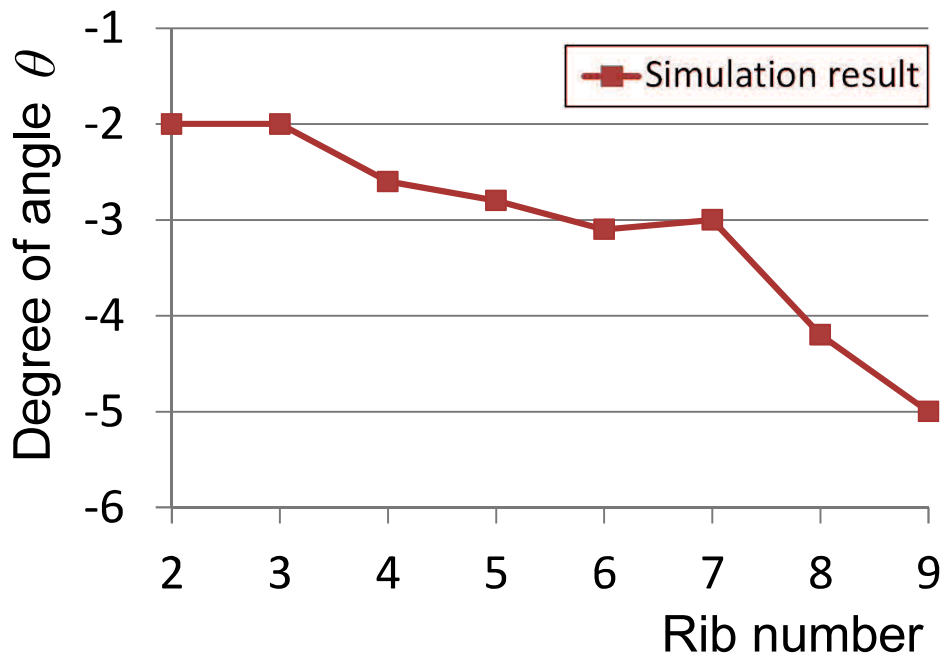


**Fig. 3-10** Simulated bucket-handle angle  $\theta$  during expiratory chest movement

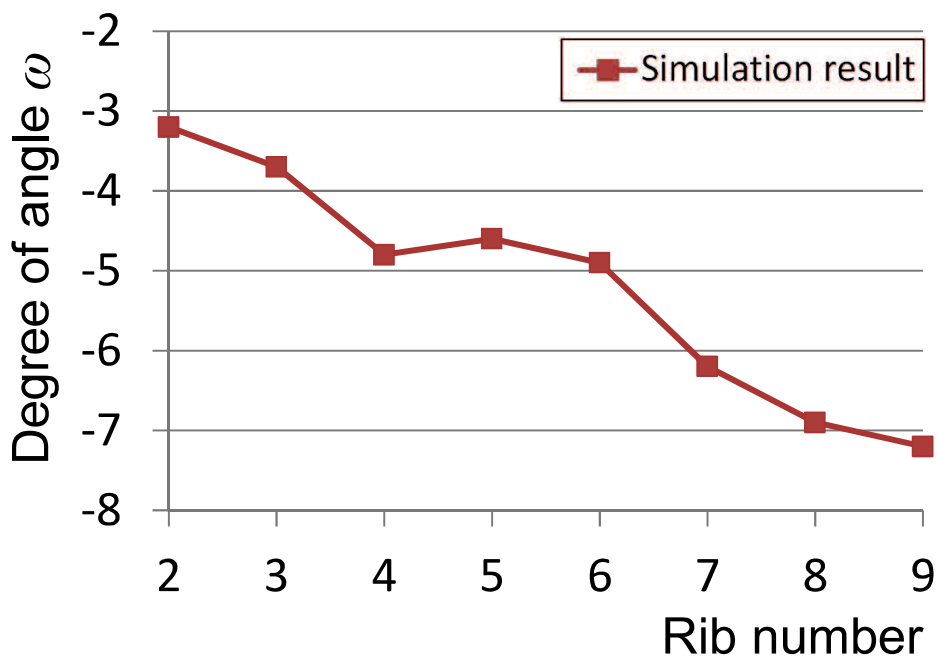


**Fig. 3-11** Simulated pump-handle angle  $\omega$  during expiratory chest movement.

To confirm the role of the intercostal muscles in the reproduction of the bucket-handle and pump-handle motions and to validate our approach, we compared the simulated angles  $\theta$  and  $\omega$  of ribs 2–9 generated by the inspiratory intercostal muscles with the experimental measurements, as shown in Fig. 3-8 and Fig. 3-9. The horizontal axis shows the rib number, and the vertical axis shows the angles  $\theta$  and  $\omega$ . We observed that the simulation results were similar to the experimental measurements: the upper ribs rotated more than the lower ribs for both the bucket-handle (angle  $\theta$ ) and pump-handle (angle  $\omega$ ) motions. The deviation in the bucket-handle angle  $\theta$  appeared at the upper ribs, which rotated more in the experimental data compared with the simulation results. For most of the ribs, the pump-handle angle  $\omega$  was smaller than those in the experimental data. Fig. 3-10 and Fig. 3-11 also summarize angles  $\theta$  and  $\omega$  generated by the expiratory intercostal muscles. The anticlockwise direction is taken as positive; the upper ribs rotated less than the lower ribs.

### **3.2.2 Diaphragm motion**

In order to confirm the simulation performance of the diaphragm motion, we first simulated the isolated contraction of the diaphragm ( $\gamma=1.0$ ) without the activation of the other inspiratory muscles in the FEM chest model. Fig. 3-12 shows a clinical observation of the sagittal plane of the diaphragm dome, which not only descended caudally but also exhibited some movement in the ventral direction accompanied by inspiratory chest movement during breathing. Fig. 3-13 illustrates a lateral view of the simulated diaphragm deformation for comparison with the clinical observation. The dome of the diaphragm exhibited a similar movement to

the clinical observation shown in Fig. 3-12, which illustrates the representative motion of the diaphragm as observed with MRI scans [55]–[57]. The front and rear views in Fig. 3-14 and Fig. 3-15 show that the diaphragm dome also descended caudally. However, regarding the ribs and sternum, contrary to the MRI scans, the isolated diaphragm contraction generated an expiratory rib rotation whereby the ribs and sternum were simultaneously pulled dorsally and caudally, as shown in Fig. 3-16 (the deformation is amplified twice for visualization). Such a movement may have resulted from the anteroposterior muscle force acting on the top of the diaphragm and was consistent with the fibre direction of the diaphragm shown in Fig. 3-17. The collaboration between the intercostal muscles and diaphragm in the thorax deformation was confirmed when the intercostal muscles and diaphragm were contracted simultaneously. In this case, a thorax deformation consistent with the MRI scans was obtained in the simulation, as shown in Fig. 3-18.

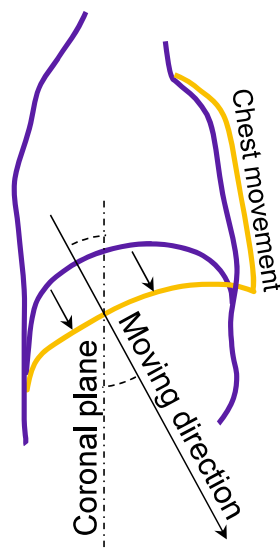


**Fig. 3-12** Clinical observation of the diaphragm motion and chest movement on the sagittal plane in MRI scans

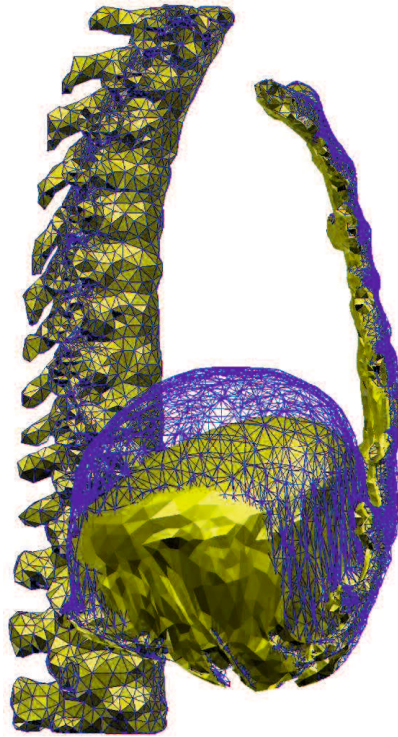


**Fig. 3-13** Simulation results of the right hemidiaphragm for comparison with the clinical observation (The orange shape: after muscle contraction; the blue shape: before muscle contraction.).

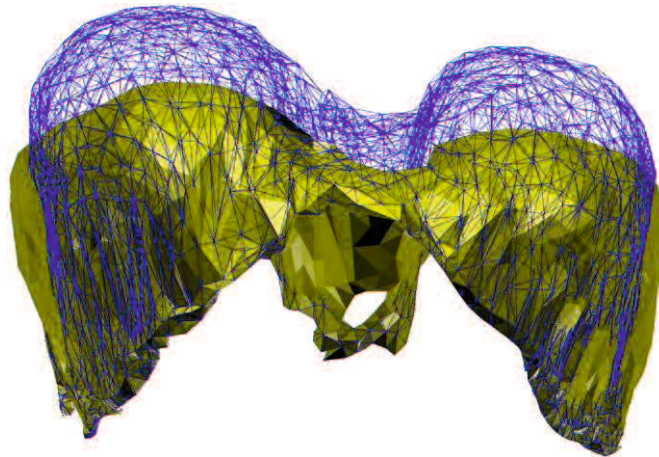


**Fig. 3-14** Front view of the diaphragm deformation (The orange shape: after muscle contraction; the blue shape: before muscle contraction.).

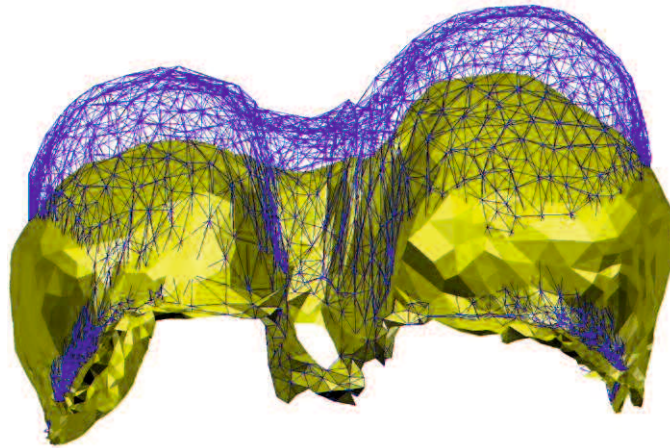


**Fig. 3-15** Rear view of the diaphragm deformation (The orange shape: after muscle contraction; the blue shape: before muscle contraction.).

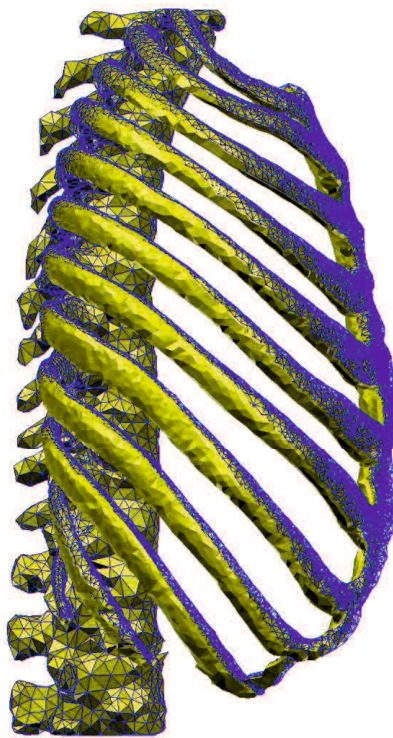


**Fig. 3-16** Motion of the rib cage caused by isolated contraction of the diaphragm (Amplified 2×; the orange shape: after muscle contraction; the blue shape: before muscle contraction.).

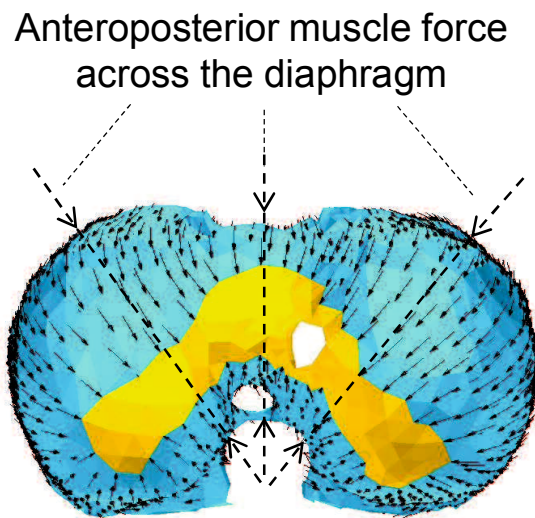


**Fig. 3-17** Distribution of muscle forces based on the radial fibre orientation in the diaphragm

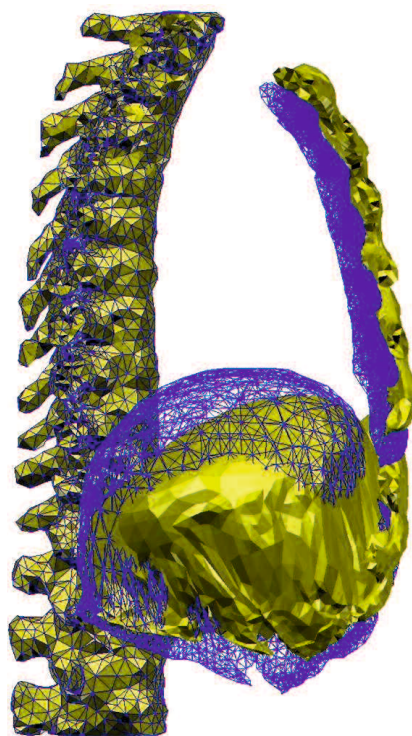


**Fig. 3-18** Simulation results of the right hemidiaphragm from simultaneous activation of the diaphragm and inspiratory intercostal muscles for comparison with the clinical observation (The orange shape: after muscle contraction; the blue shape: before muscle contraction.).

### **3.2.3 Thorax deformation during normal quiet breathing and comparison with 4D-CT images**

After confirming the performance of the intercostal muscles and diaphragm, we simultaneously activated the external intercostal muscles, parasternal intercostal muscles, and diaphragm to simulate the thorax deformation during normal quiet breathing. For the external intercostal and parasternal intercostal muscles, the same activation distribution as that described in the section entitled ‘Rib motion’ was adopted, and the activation level  $\gamma$  was set to 0.3 for the inspiratory intercostal muscles and diaphragm based on the results of experiments with spontaneously breathing dogs [58]. The simulated deformation results were compared with the 4D-CT images captured during normal quiet breathing in order to validate our findings.

Fig. 3-19, Fig. 3-20 and Fig. 3-21 show the resultant thorax deformation. The front, lateral, and oblique views show that the sternum moved superiorly and that the ribs rotated cranially and ventrally, while the dome of the diaphragm moved inferiorly and anteriorly. For the movements of the diaphragm observed with CT images, we chose planes X and Z, (shown in Fig. 3-22) which did not cross the heart, and extracted the movements of the ribs and the diaphragm from the 4D-CT images, as shown from Fig 3-23 to 3-28. The solid line in Fig. 3-24 and Fig. 3-27 represents the state before inhalation, while the dashed line corresponds to the state after inhalation. The arrows illustrate the movement direction of the diaphragm tops for visualization. The arrows in Fig. 3-24 show that the diaphragm moved in the craniocaudal direction. The arrow in Fig. 3-27 illustrates the oblique moving direction of the diaphragm top, which not only descended in the craniocaudal direction but also in the dorsal-ventral direction.

Correspondingly, the simulated deformations shown in Fig. 3-25 and Fig. 3-28 represent the same motion observed in the CT images. The dashed lines in Fig. 3-24 and Fig. 3-27 show the rib movements extracted from the CT images. Even though the inspiratory rib movement was small during normal quiet breathing, the simulation results were consistent with the CT images: the ribs slightly rotated cranially and ventrally, and the circumference of the chest increased, which represented the inspiratory rib motion. We also compared the time variation of the diaphragm deformation with the 4D-CT images. Fig. 3-27 and Fig. 3-28 show the three locations on plane Z chosen for comparison, which are marked with dotted lines and labelled L1, L2, and L3. Fig. 3-29, Fig. 3-30 and Fig. 3-31 show the compared results. The vertical axis ( $D/D1$ ) in Fig. 3-29, Fig. 3-30 and Fig. 3-31 shows the displacement normalized against that of location L1.  $D$  is the displacement of each location and  $D1$  is the displacement of location L1. The horizontal axis corresponds to the elapsed time during quiet breathing from 0 to 5 s. The dotted line corresponds to the 4D-CT images, while the solid line represents the simulation results.

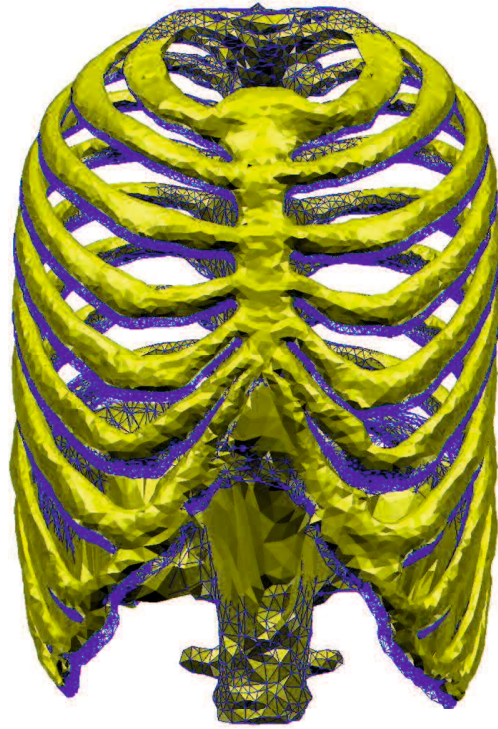


**Fig. 3-19** The front view of obtained thorax deformation



**Fig. 3-20** The lateral view of obtained thorax deformation

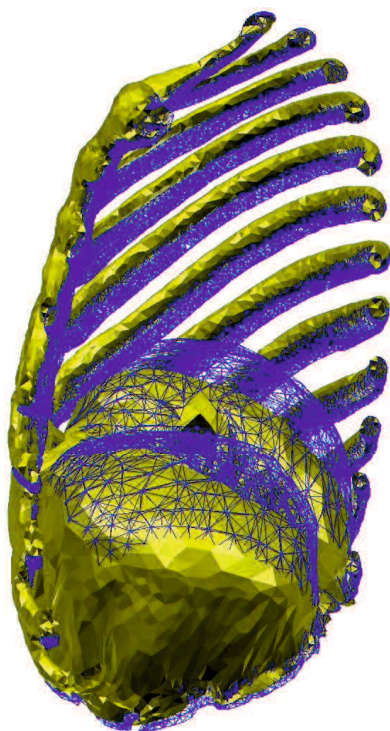


**Fig. 3-21** The oblique view of obtained thorax deformation

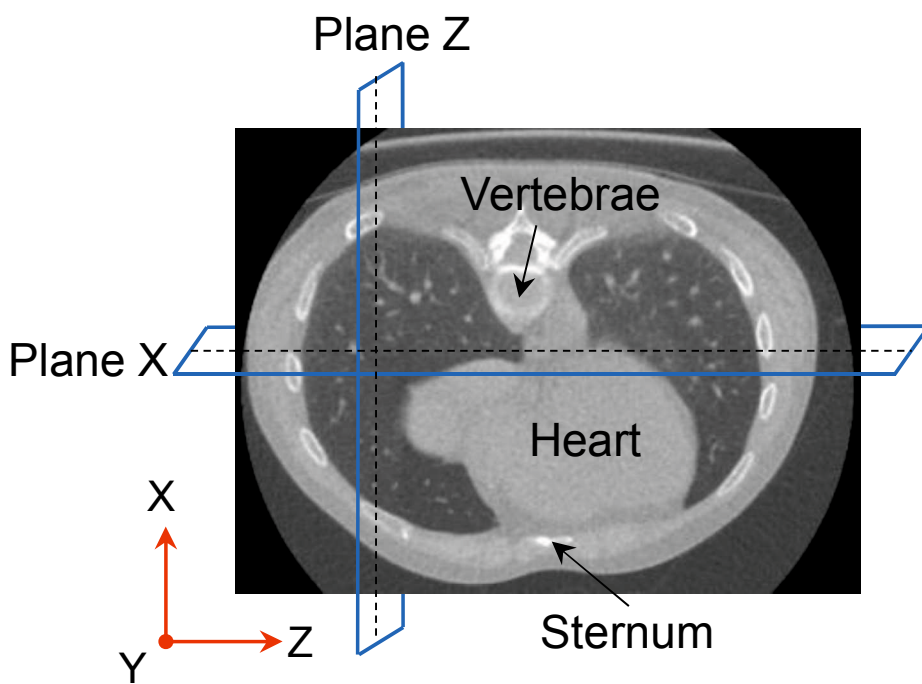


**Fig. 3-22** Location of planes X and Z in the chest

Plane X

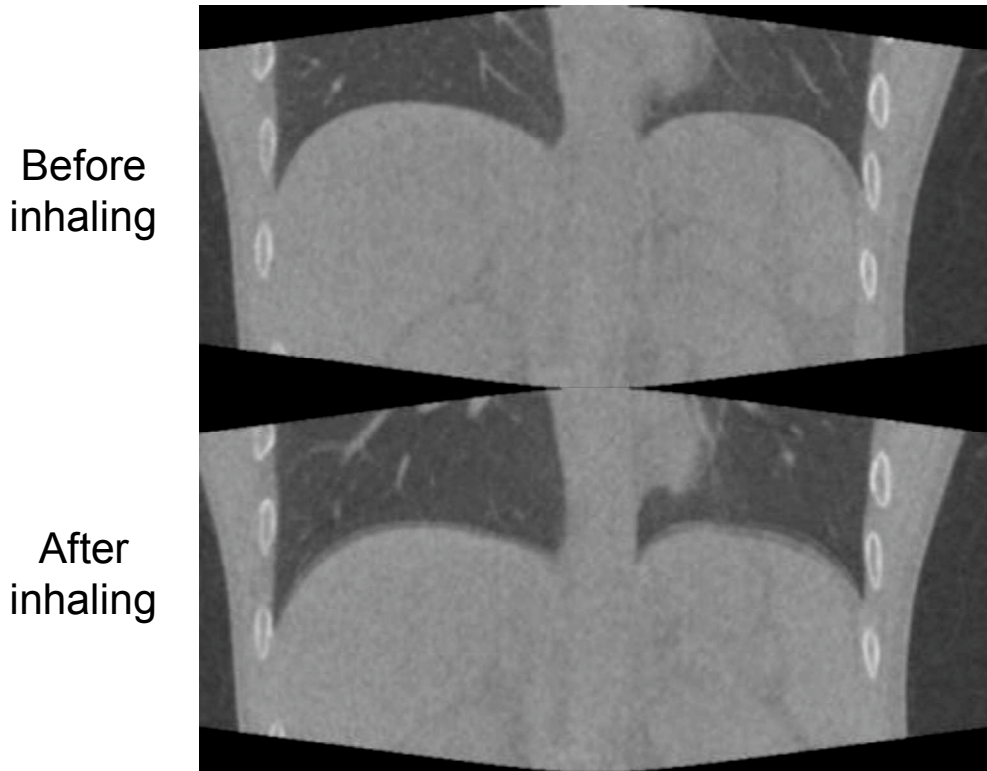


Fig. 3-23 CT images on plane X

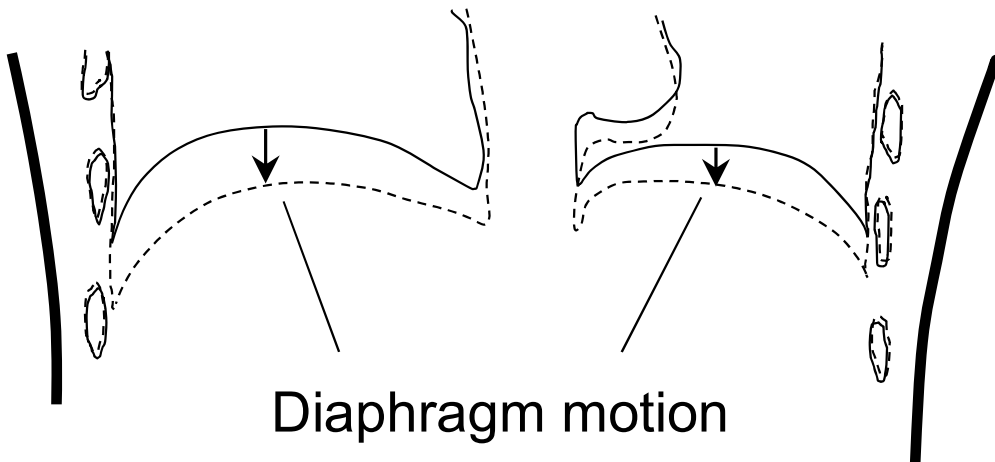
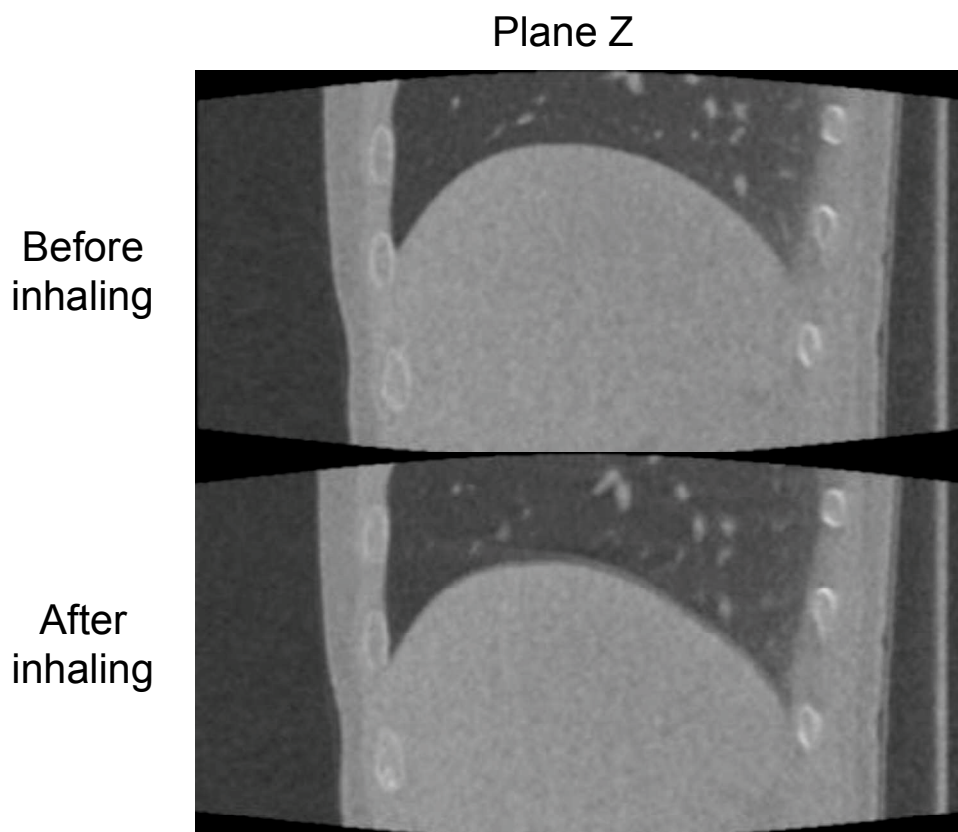


Fig. 3-24 Extracted motion of plane X from CT images (the dashed line represents the state after inhaling; the solid line represents the state before inhaling)



**Fig. 3-25** The simulation results on plane X (the orange shape represents the state after muscle contraction; the blue shape represents the state before muscle contraction)



**Fig. 3-26** CT images on plane Z

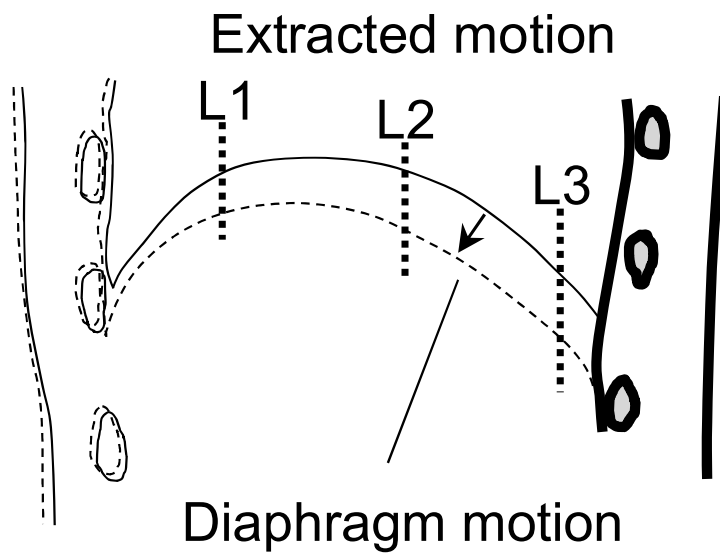


**Fig. 3-27** Extracted motion of plane Z from CT images (the dashed line represents the state after inhaling; the solid line represents the state before inhaling)

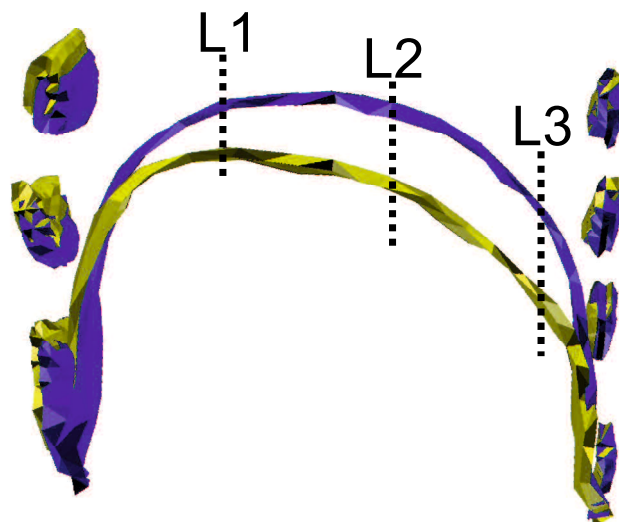


**Fig. 3-28** The simulation results on plane Z (the orange shape represents the state after muscle contraction; the blue shape represents the state before muscle contraction)

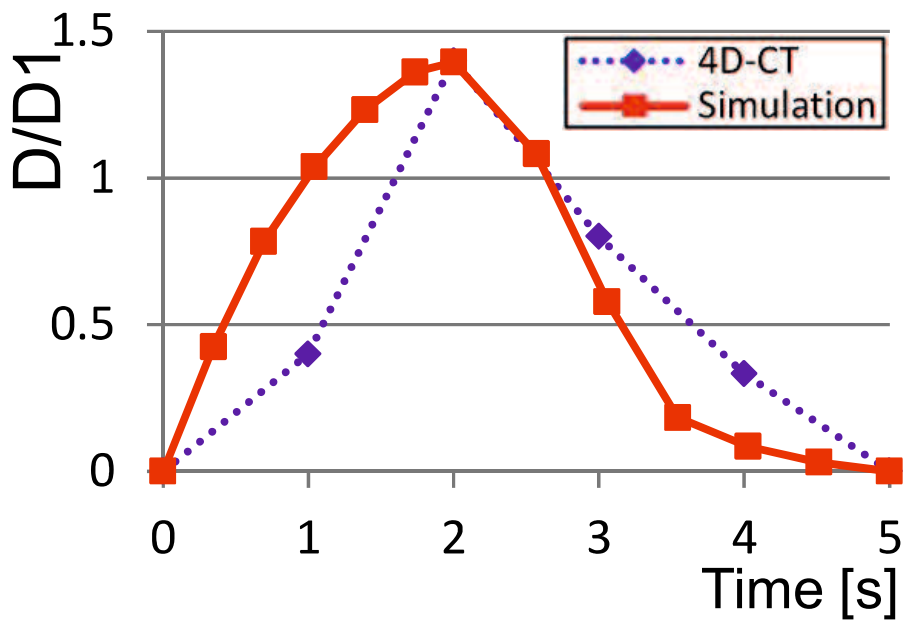


Fig. 3-29 Movement at location L1 on plane Z compared with 4D-CT images

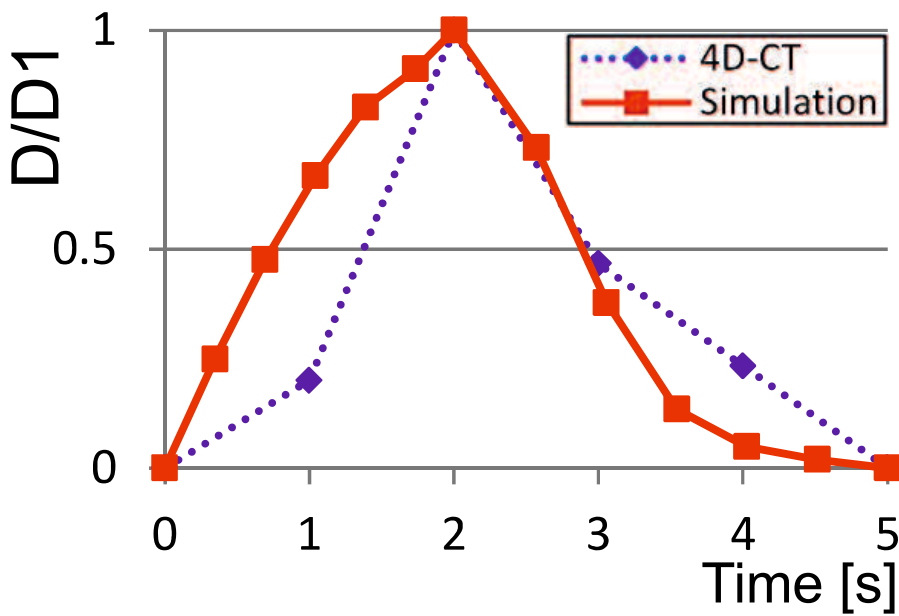


Fig. 3-30 Movement at location L2 on plane Z compared with 4D-CT images

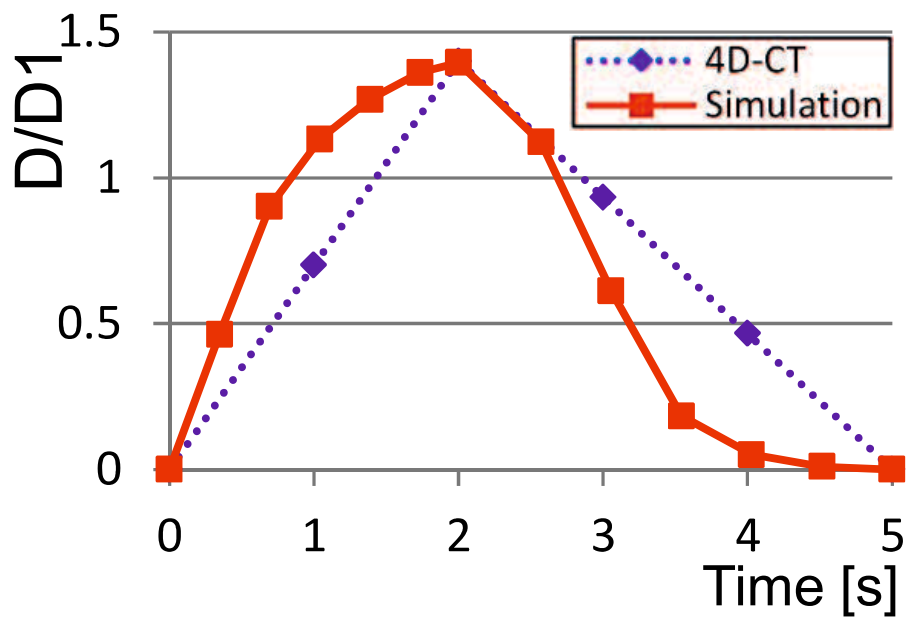


Fig. 3-31 Movement at location L3 on plane Z compared with 4D-CT images

### 3.3 Discussion

To simulate the thorax deformation, we modelled the respiratory muscles based on continuum mechanics while considering muscle contractions. The introduction of the Hill-type transversely isotropic hyperelastic continuum skeletal muscle model allowed the respiratory muscles to contract along the direction of the fibres and thus reproduce the representative motions of the ribs and diaphragm according to physiology. In this study, we focused on validating the effectiveness of this approach at simulating the thorax deformation driven by the diaphragm and the intercostal muscles, which are significant for human breathing.

### 3.3.1 Rib motion

We simulated the chest movement driven by the inspiratory and expiratory intercostal muscles based on the measured muscle activity distribution [1], [54]. As expected, the anteroposterior and transverse diameters increased while the inspiratory intercostal muscles contracted (Fig. 3-2, 3-3, 3-4) and decreased while the expiratory intercostal muscles contracted (Fig. 3-5, 3-6, 3-7). These results demonstrated the importance of the intercostal muscles to breathing because they can expand and contract the rib cage.

Besides the changes in the diameter of the rib cage, we were also able to reproduce the representative bucket-handle and pump-handle motions of the ribs. In the same manner as described in the literature [45], the bucket-handle motion primarily appeared in the lower ribs, for which the transverse diameter changes (Fig. 3-2, and Fig. 3-5) were larger than the changes in the anteroposterior diameter (Fig. 3-4 and Fig. 3-7). For the upper ribs, the changes in the anteroposterior diameter of the upper ribs prominently expressed the pump-handle motion. Hence, the intercostal muscles were found to have the primary function of producing the bucket-handle and pump-handle motions during human breathing.

To validate the generated bucket-handle and pump-handle motions for each rib, we compared the simulation results of the bucket-handle angle  $\theta$  and pump-handle angle  $\omega$ , as shown in Fig. 3-3, Fig. 3-4, Fig. 3-6 and Fig. 3-7, for ribs 2–9 with the results of the lung inflation experiments carried out by Troyer et al. [38]. As shown in Fig 3-8 and Fig. 3-9, the rib rotation angles  $\theta$  and  $\omega$  were close to the experimental measurements. This demonstrated that our approach of activating the inspiratory intercostal muscles successfully reproduced the bucket-handle and pump-handle

motions for each rib, which actually occur during human inspiration. Consequently, the obtained inspiratory and expiratory chest movements and reproduction of the representative rib motions validated our approach of simulating rib motions driven by the inspiratory intercostal muscles.

Regarding the deviation of the upper ribs, which rotated more in the experimental data than in the simulation results, we believe that this was because we did not consider the other inspiratory muscles which also contract during human deep breathing, especially the cervical accessory muscles which act on top of the rib cage. Although the external intercostal muscles are the most important muscles for elevating the rib cage, the cervical accessory muscles (i.e. sternocleidomastoid and scalene muscles) also help elevate the upper ribs [2]. Loring's FEM analysis demonstrated that the cervical accessory muscles elevate the entire rib cage and especially cause the pump-handle motion for each rib [11]. Regarding the simulation results, Fig 3-8 and Fig. 3-9 show that the deviation of the bucket-handle angle was relatively large in the upper ribs, whereas the pump-handle angles were smaller than the experimental measurements for each rib. These results imply that the cervical accessory muscles may have a greater influence on elevating the rib cage during deep breathing.

Although we are unaware of any experimental data for rib rotation during expiration, because the internal intercostal muscles in the caudal–dorsal area exhibited the greatest activity during expiration [54], the results of our simulation showed that the internal intercostal muscles could rotate the lower ribs more than the upper ribs during expiration, as shown in Fig 3-10 and Fig. 3-11.

Consequently, this examination demonstrated that the Hill-type transversely isotropic hyperelastic continuum skeletal muscle model provides an effective means of simulating rib motions driven by the intercostal muscles.

### **3.3.2 Diaphragm motion**

For the simulation of the diaphragm motion, we first confirmed the ability of the proposed approach to reproducing the representative motion of the diaphragm as observed clinically by MRI scans. In these clinical observations, the diaphragm moves in the craniocaudal direction at an angle to the coronal plane, as shown in Fig. 3-12 [55]–[57]. This movement characterizes the fact that the diaphragm not only moves vertically like a piston but also moves in the caudal-ventral direction. In the simulation with isolated diaphragm contractions, as shown in Fig. 3-13, the dome of the diaphragm on the sagittal plane moved in the same directions (caudally and ventrally) as those observed with MRI scans. The front and rear views in Fig. 3-14 and Fig. 3-15 show that the diaphragm moved vertically like a piston. This diaphragm motion can be attributed to its anatomical structure, in that the muscle fibres are short in the area between the sternum and anterior tendon while the longer muscles are in the posterior part and on both sides of the diaphragm (Fig. 2-3). Although the muscles in the anterior part of the diaphragm also lower the tendon, the displacement is smaller than in the other areas. Therefore, the diaphragm moved in the craniocaudal direction at an angle to the coronal plane (Fig. 3-13 and Fig. 3-18).

Note that the isolated contraction of the diaphragm pulled the ribs dorsally and caudally to result in an expiratory rib motion (Fig. 3-16) due to the

anteroposterior muscle force (Fig. 3-17) on top of the diaphragm dome. Clearly, such deformation differs from the clinical observation shown in Fig. 3-12, where the chest movements are inspiratory. To investigate the reason for the deviation, we simultaneously activated the inspiratory intercostal muscles and the diaphragm, and the resultant deformation is shown in Fig. 3-18. The comparison between Fig. 3-12 and Fig. 3-18 clearly shows that an inspiratory chest movement and diaphragm motion similar to the clinical observation were obtained in the simulation.

Note that the effects of the diaphragm and inspiratory intercostal muscles were opposite because the contraction of the diaphragm could caudally and dorsally rotate the ribs to extend the inspiratory intercostal muscle fibres, whereas the contraction of the inspiratory intercostal muscles could cranially and ventrally rotate the ribs to lengthen the diaphragm muscle fibres. This phenomenon is consistent with the experimental observation by DiMarco et al. [35]. The significance of this phenomenon is primarily related to the active force-length relationship (Fig. 1-7). The active force-length relationship determines the optimal length for exerting muscle force. Thus, during the contraction of the diaphragm, the length of the contracted muscle fibres gradually diverges from the optimal length. If the inspiratory intercostal muscles contract, they not only expand the thorax but also extend the diaphragm muscle fibres to approach their optimal length and thus provide more muscle contraction force to resist the abdominal and pleural pressures during breathing. Therefore, representing this mechanism is important in order to simulate a mostly realistic mechanical environment of the chest during breathing.

The simulation results not only demonstrated the effectiveness of our approach to simulating the diaphragm motion but also illustrated the importance of simultaneous contraction of the diaphragm and inspiratory intercostal muscles when simulating human breathing.

### **3.3.3 Validation of simulated thorax deformation with 4D-CT images**

In normal quiet breathing, the diaphragm and intercostal muscles are the main inspiratory muscles, and the abdominal pressure is small compared with the diaphragmatic contracting force. Thus, we simulated the thorax deformation during normal quiet breathing by simultaneously activating the external intercostal muscles, parasternal intercostal muscles, and diaphragm. The distributions of the inspiratory intercostal muscle activation were based on the measurements obtained during spontaneous breathing [1], [54], as described in the subsection ‘Rib motion’ of the ‘Results’ section.

The obtained chest movement (Fig. 3-19 and Fig. 3-20) and diaphragm motion (Fig. 3-21) illustrate that the inspiratory chest movement was generated, and the dome of the diaphragm descended in the caudal-ventral direction. Even though the rib movement is small during normal quiet breathing, inspiratory rib motion can be observed in both the CT images and simulation results (from Fig. 3-22 to Fig. 3-28); the ribs slightly rotated cranially and ventrally as the circumference of the chest increased. This inspiratory rib motion also contained the bucket-handle and pump-handle motions as shown in Fig. 3-2 and Fig. 3-4.

Concerning the deformation of the diaphragm, we first compared the diaphragm shape after the inhaling state when the movements of the ribs

and diaphragm reached their maximum during normal quiet breathing. The extracted CT images in Fig. 3-24 show that the diaphragm descended caudally and the shape remained unchanged, similar to the simulated diaphragm shape. The extracted CT images in Fig. 3-27 show that the posterior portion descended more caudally than the anterior portion. The same deformation pattern was also observed in the simulated diaphragm shape as shown in Fig. 3-25 and Fig. 3-28. The amount of movement on top of the diaphragmatic dome in the craniocaudal direction (MTDDCD) was approximately equal to 12 times that in the dorsal-ventral direction of the sternum in both the CT images and simulation results. The magnitude of the MTDDCD was 1.5 cm, which agrees with the measurements obtained by Wade during normal quiet breathing [59].

To confirm the diaphragm movement during the breathing process, we examined the time variation in the movement of the diaphragm by selecting three locations on plane Z of the diaphragm in 4D-CT (Fig. 3-27 and Fig. 3-28). Similar time variations in the measured and simulated movements are given in Fig. 3-29, Fig. 3-30 and Fig. 3-31. The diaphragm movements extracted from the 4D-CT images were slower than the simulation results during both the inspiratory and expiratory procedures. This can be attributed to the viscosity of the airflow in the lungs during breathing because the redistribution of the airflow in the bronchi and alveoli throughout the lungs delays the response of the lung deformation to the inspiratory muscle contraction. Therefore, the deviation between the simulation and 4D-CT images indicates the importance of introducing a lung model and airway system which can represent the viscous effect in the chest during breathing.

By introducing the Hill-type transversely isotropic hyperelastic continuum skeletal muscle model and simultaneously activating the external intercostal muscles, parasternal intercostal muscles, and diaphragm, we were able to validate the effectiveness of the proposed approach for simulating the thorax deformation during normal quiet breathing by comparison with 4D-CT images.

### **3.4 Conclusions**

To simulate the thorax deformation driven by the diaphragm and intercostal muscles, we modelled the respiratory muscles according to continuum mechanics and by introducing muscle contractions. By introducing the Hill-type transversely isotropic hyperelastic continuum skeletal muscle model for the diaphragm and intercostal muscles, we were able to obtain the representative motions of the diaphragm and ribs as generated by muscle contractions.

For the ribs, inspiratory and expiratory rib movements including the representative bucket-handle and pump-handle motions were reproduced by activating the inspiratory and expiratory intercostal muscles individually. The rib rotation angles for the bucket-handle and pump-handle motions were validated by comparison to experimental measurements carried out by Troyer et al. [38]. For the diaphragm, we not only obtained the representative motion as observed in MRI scans but also demonstrated the interaction between the diaphragm and inspiratory intercostal muscles during breathing. The latter is important for simulating the mostly realistic mechanical environment of the chest during breathing. The effectiveness of the proposed approach at simulating the thorax deformation during normal quiet breathing was validated by comparison with 4D-CT images. A deviation between the simulation and clinical observation occurred in the rib and diaphragm motions; this was due to the lack of cervical accessory muscles in the model and the viscosity effect of the airflow in the lung. More important, this approach makes it possible to simulate the lung deformation and ventilation caused by the thorax deformation.

# 4

## Simulation of lung deformation and ventilation

---

The human breathing is generated by the respiratory muscle contraction that the lungs are extended and shrunk during inhaling and exhaling. The lung deformation involves the deformation of the lung parenchyma and the air flow during ventilation. Base on the reproducing of thorax deformation, in order to simulate the lung deformation, this work introduces the porous hyperelastic material model to calculate both the deformation of the lung parenchyma and air volume change in the lung due to the ventilation. Consequently, the lung deformation, alveolar and pleural pressures are reproduced by activating the intercostal muscles and diaphragm as the actual physiological activities happened during human breathing.

### 4.1 Method

#### 4.1.1 Porous hyperelastic material model

The porous hyperelastic material model is based on biphasic theory which macroscopically assumes the solid and fluid phases have the same spatial localization. In addition, microscopically the infinitesimal volume of the solid phase  $dV^s$  and fluid phase  $dV^f$  are

$$dV^s + dV^f = dV \quad (4.1)$$

where  $dV$  is the infinitesimal volume of the biphasic mixture. The volume ratio of each phase could be defined as

$$\phi^s = \frac{dV^s}{dV}, \quad \phi^f = \frac{dV^f}{dV}, \quad \phi^s + \phi^f = 1 \quad (4.2)$$

where the index  $s$  and  $f$  illustrate solid and fluid. Hence, the density of the biphasic mixture  $\rho$  could be written as

$$\begin{aligned} \rho &= \frac{dm_T^s}{dV} + \frac{dm_T^f}{dV} \\ &= \frac{dV^s \rho_T^s}{dV} + \frac{dV^f \rho_T^f}{dV} \\ &= \frac{dV \phi^s \rho_T^s}{dV} + \frac{dV \phi^f \rho_T^f}{dV} \\ &= \phi^s \rho_T^s + \phi^f \rho_T^f \end{aligned} \quad (4.3)$$

where the  $\rho_T^s$  and  $\rho_T^f$  illustrates true density of the solid and fluid phases, respectively. Therefore, the apparent density  $\rho^\alpha$  of each phase could be defined as follow

$$\rho^\alpha = \phi^\alpha \rho_T^\alpha \quad (4.4)$$

According to law of conservation of mass,

$$\frac{D}{Dt} \int_{B_t} \rho^\alpha(\mathbf{x}, t) dv = 0 \quad (4.5)$$

where D means material time derivative and  $B_t$  is current configuration.

$$\begin{aligned} \frac{D}{Dt} \int_{B_t} \rho^\alpha(\mathbf{x}, t) dv &= \int_{B_t} \left( \frac{D\rho^\alpha(\mathbf{x}, t)}{Dt} + \rho^\alpha(\mathbf{x}, t) \operatorname{div} \mathbf{v}^\alpha(\mathbf{x}, t) \right) dv \\ &= \int_{B_t} \left( \frac{\partial \rho^\alpha(\mathbf{x}, t)}{\partial t} + \nabla \cdot (\rho^\alpha(\mathbf{x}, t) \mathbf{v}^\alpha(\mathbf{x}, t)) \right) dv \\ &= 0 \end{aligned} \quad (4.6)$$

Because the mass keeps constant at everywhere in  $B_t$ , therefore

$$\frac{\partial \rho^\alpha(\mathbf{x}, t)}{\partial t} + \nabla \cdot (\rho^\alpha(\mathbf{x}, t) \mathbf{v}^\alpha(\mathbf{x}, t)) = 0 \quad (4.7)$$

and,

$$\begin{aligned} &\frac{\partial \phi^\alpha(\mathbf{x}, t) \rho_T^\alpha(\mathbf{x}, t)}{\partial t} + \nabla \cdot (\phi^\alpha(\mathbf{x}, t) \rho_T^\alpha(\mathbf{x}, t) \mathbf{v}^\alpha(\mathbf{x}, t)) \\ \Rightarrow &\rho_T^\alpha(\mathbf{x}, t) \frac{\partial \phi^\alpha(\mathbf{x}, t)}{\partial t} + \phi^\alpha(\mathbf{x}, t) \frac{\partial \rho_T^\alpha(\mathbf{x}, t)}{\partial t} \\ &+ \frac{\partial (\phi^\alpha(\mathbf{x}, t) \rho_T^\alpha(\mathbf{x}, t) v_i^\alpha(\mathbf{x}, t))}{\partial x_i} \end{aligned}$$

$$\begin{aligned}
&= \rho_T^\alpha(\mathbf{x}, t) \frac{\partial \phi^\alpha(\mathbf{x}, t)}{\partial t} + \phi^\alpha(\mathbf{x}, t) \frac{\partial \rho_T^\alpha(\mathbf{x}, t)}{\partial t} \\
&+ \rho_T^\alpha(\mathbf{x}, t) \frac{\partial (\phi^\alpha(\mathbf{x}, t) v_i^\alpha(\mathbf{x}, t))}{\partial x_i} + \phi^\alpha(\mathbf{x}, t) v_i^\alpha(\mathbf{x}, t) \frac{\partial (\rho_T^\alpha(\mathbf{x}, t))}{\partial x_i} \\
&= 0
\end{aligned} \tag{4.8}$$

Consider the solid and fluid phases, equation (4.8) could be written as

$$\begin{aligned}
&\rho_T^f(\mathbf{x}, t) \frac{\partial \phi^f(\mathbf{x}, t)}{\partial t} + \phi^f(\mathbf{x}, t) \frac{\partial \rho_T^f(\mathbf{x}, t)}{\partial t} \\
&+ \rho_T^f(\mathbf{x}, t) \frac{\partial (\phi^f(\mathbf{x}, t) v_i^f(\mathbf{x}, t))}{\partial x_i} + \phi^f(\mathbf{x}, t) v_i^f(\mathbf{x}, t) \frac{\partial (\rho_T^f(\mathbf{x}, t))}{\partial x_i} \\
&+ \rho_T^s(\mathbf{x}, t) \frac{\partial \phi^s(\mathbf{x}, t)}{\partial t} + \phi^s(\mathbf{x}, t) \frac{\partial \rho_T^s(\mathbf{x}, t)}{\partial t} \\
&+ \rho_T^s(\mathbf{x}, t) \frac{\partial (\phi^s(\mathbf{x}, t) v_i^s(\mathbf{x}, t))}{\partial x_i} + \phi^s(\mathbf{x}, t) v_i^s(\mathbf{x}, t) \frac{\partial (\rho_T^s(\mathbf{x}, t))}{\partial x_i} \\
&= \rho_T^f(\mathbf{x}, t) \left( \frac{\partial \phi^f(\mathbf{x}, t)}{\partial t} + \frac{\partial (\phi^f(\mathbf{x}, t) v_i^f(\mathbf{x}, t))}{\partial x_i} \right) \\
&+ \phi^f(\mathbf{x}, t) \left( \frac{\partial \rho_T^f(\mathbf{x}, t)}{\partial t} + v_i^f(\mathbf{x}, t) \frac{\partial (\rho_T^f(\mathbf{x}, t))}{\partial x_i} \right) \\
&+ \rho_T^s(\mathbf{x}, t) \left( \frac{\partial \phi^s(\mathbf{x}, t)}{\partial t} + \frac{\partial (\phi^s(\mathbf{x}, t) v_i^s(\mathbf{x}, t))}{\partial x_i} \right) \\
&+ \phi^s(\mathbf{x}, t) \left( \frac{\partial \rho_T^s(\mathbf{x}, t)}{\partial t} + v_i^s(\mathbf{x}, t) \frac{\partial (\rho_T^s(\mathbf{x}, t))}{\partial x_i} \right) \\
&= 0
\end{aligned} \tag{4.9}$$

Because the solid and fluid phases are considered as incompressible material in biphasic theory, so that

$$\frac{D\rho_T^\alpha(\mathbf{x},t)}{Dt} = \frac{\partial\rho_T^\alpha(\mathbf{x},t)}{\partial t} + \mathbf{v}^\alpha(\mathbf{x},t) \cdot \frac{\partial\rho_T^\alpha(\mathbf{x},t)}{\partial \mathbf{x}} = 0 \quad (4.10)$$

$$\begin{aligned} & \rho_T^f(\mathbf{x},t) \left( \frac{\partial\phi^f(\mathbf{x},t)}{\partial t} + \frac{\partial(\phi^f(\mathbf{x},t)v_i^f(\mathbf{x},t))}{\partial x_i} \right) \\ & + \rho_T^s(\mathbf{x},t) \left( \frac{\partial\phi^s(\mathbf{x},t)}{\partial t} + \frac{\partial(\phi^s(\mathbf{x},t)v_i^s(\mathbf{x},t))}{\partial x_i} \right) \\ & = 0 \end{aligned} \quad (4.11)$$

Equation (4.11) also could be written for the solid and fluid phases, respectively, hence

$$\frac{\partial\phi^f(\mathbf{x},t)}{\partial t} + \frac{\partial(\phi^f(\mathbf{x},t)v_i^f(\mathbf{x},t))}{\partial x_i} = 0 \quad (4.12)$$

$$\frac{\partial\phi^s(\mathbf{x},t)}{\partial t} + \frac{\partial(\phi^s(\mathbf{x},t)v_i^s(\mathbf{x},t))}{\partial x_i} = 0 \quad (4.13)$$

So that,

$$\frac{\partial\phi^s(\mathbf{x},t)}{\partial t} + \frac{\partial(\phi^s(\mathbf{x},t)v_i^s(\mathbf{x},t))}{\partial x_i} + \frac{\partial\phi^f(\mathbf{x},t)}{\partial t} + \frac{\partial(\phi^f(\mathbf{x},t)v_i^f(\mathbf{x},t))}{\partial x_i}$$

$$\begin{aligned}
&\Rightarrow \frac{\partial(\phi^s(\mathbf{x},t) + \phi^f(\mathbf{x},t))}{\partial t} + \nabla \cdot (\phi^s(\mathbf{x},t)\mathbf{v}^s(\mathbf{x},t) + \phi^f(\mathbf{x},t)\mathbf{v}^f(\mathbf{x},t)) \\
&= \frac{\partial(1)}{\partial t} + \nabla \cdot (\phi^s(\mathbf{x},t)\mathbf{v}^s(\mathbf{x},t) + \phi^f(\mathbf{x},t)\mathbf{v}^f(\mathbf{x},t)) \\
&= \nabla \cdot (\phi^s(\mathbf{x},t)\mathbf{v}^s(\mathbf{x},t) + \phi^f(\mathbf{x},t)\mathbf{v}^f(\mathbf{x},t)) \\
&\Rightarrow \nabla \cdot (\phi^s\mathbf{v}^s + \phi^f\mathbf{v}^f) \\
&= \nabla \cdot ((1 - \phi^f)\mathbf{v}^s + \phi^f\mathbf{v}^f) \\
&= \nabla \cdot (\mathbf{v}^s - \mathbf{v}^s\phi^f + \phi^f\mathbf{v}^f) \\
&= \nabla \cdot (\mathbf{v}^s + \phi^f(\mathbf{v}^f - \mathbf{v}^s)) \\
&= \nabla \cdot (\mathbf{v}^s + \mathbf{w}) \\
&= 0
\end{aligned} \tag{4.14}$$

where  $\mathbf{w} = (\mathbf{v}^f - \mathbf{v}^s)$  is apparent relative velocity between the solid and fluid phases. The interaction force between the solid and fluid phases are defined as  $\pi^s$  and  $\pi^f$ , so that without considering body forces and inertial forces the motion equation could be written as

$$\nabla \cdot \boldsymbol{\sigma}^\alpha + \boldsymbol{\pi}^\alpha = \mathbf{0} \tag{4.15}$$

$\boldsymbol{\sigma}^\alpha$  is partial Cauchy stress for the solid and fluid phases. Because of  $\boldsymbol{\pi}^s = -\boldsymbol{\pi}^f$ , therefore

$$\nabla \cdot (\boldsymbol{\sigma}^s + \boldsymbol{\sigma}^f) = \mathbf{0} = \nabla \cdot \boldsymbol{\sigma} \tag{4.16}$$

And Cauchy stress for the solid and fluid phases could be written as

$$\boldsymbol{\sigma}^s = -\phi^s p \mathbf{I} + \boldsymbol{\sigma}_E^s \quad (4.17)$$

$$\boldsymbol{\sigma}^f = -\phi^f p \mathbf{I} \quad (4.18)$$

where  $p$  is hydrostatic pressure,  $\boldsymbol{\sigma}_E^s$  is the Cauchy stress due to the deformation of solid phase. Therefore, according to equation (4.17) and (4.18) the Cauchy stress for the biphasic mixture is

$$\boldsymbol{\sigma} = \boldsymbol{\sigma}^s + \boldsymbol{\sigma}^f = -p \mathbf{I} + \boldsymbol{\sigma}_E^s \quad (4.19)$$

In this model, the apparent relative velocity  $\boldsymbol{w}$  and hydrostatic pressure  $p$  have a relationship that

$$\boldsymbol{w} = -\boldsymbol{\kappa} \cdot \nabla p \quad (4.20)$$

where  $\boldsymbol{\kappa}$  is permeability tensor. On the boundary surface,

$$\boldsymbol{\sigma}^T \cdot \boldsymbol{n} = \hat{\boldsymbol{t}} \quad \text{on } \gamma_t \quad (4.21)$$

$$p = \hat{p} \quad \text{on } \gamma_p \quad (4.22)$$

$\hat{\mathbf{t}}$  is the applied external force,  $\hat{p}$  is applied pressure of fluid phase. Hence, the governing equations and boundary conditions in current configuration are as follow:

$$\nabla \cdot \boldsymbol{\sigma} = \mathbf{0} \quad (4.23)$$

$$\mathbf{w} = -\boldsymbol{\kappa} \cdot \nabla p \quad (4.24)$$

$$\nabla \cdot (\mathbf{v}^s + \mathbf{w}) = 0 \quad (4.25)$$

$$\boldsymbol{\sigma}^T \cdot \mathbf{n} = \hat{\mathbf{t}} \quad \text{on } \gamma_t \quad (4.26)$$

$$p = \hat{p} \quad \text{on } \gamma_p \quad (4.27)$$

For calculations of the large deformation problems, the governing equations were transformed to reference configuration as follow:

$$\nabla_0 \cdot \boldsymbol{\Pi} = \mathbf{0} \quad (4.28)$$

$$\mathbf{W} = -\boldsymbol{\mathcal{K}} \cdot \nabla_0 p \quad (4.29)$$

$$J - 1 + \nabla_0 \cdot \mathbf{Q} = 0 \quad (4.30)$$

$$\boldsymbol{\Pi} \cdot \mathbf{N} = \bar{\mathbf{t}} \quad \text{on } \Gamma_t \quad (4.31)$$

$$p = \hat{p} \quad \text{on } \Gamma_p \quad (4.32)$$

Where  $\boldsymbol{\Pi}$  is the first Piola-Kirchoff stress tensor,  $\mathbf{Q}$  is defined by  $V = \mathbf{Q} \cdot \mathbf{N} dS$  that  $\mathbf{N}$  is the unit vector normal to the infinitesimal surface

element  $dS$  and  $V$  is the volume of the fluid phases flowed out of the infinitesimal surface element from initial to present time.  $\Gamma_t$  and  $\Gamma_p$  is the boundary surfaces of the solid and fluid phase at reference configuration. The detailed formulation of this porous hyperelastic material model was studied by Chen et al[60].

### **4.1.2 Simulation conditions**

We fixed the bottom of the spinal cord. The initial condition of pleural pressure was set to be -5cmH<sub>2</sub>O based on the clinical observation that at the end of expiration, there is a negative pressure in the pleural space due to the lung's elastic recoil [2]. At the present stage, the atmosphere pressure (i.e. zero pressure) was applied directly at appropriately selected nodes in the lung by ignoring the difference between pressures of alveolar and atmosphere resulted from the resistance in the airway.

The material parameters and the muscle activation used for the intercostal muscles and diaphragm are the same as those in the thorax deformation simulation during normal quiet breathing. For the porous hyperelastic model of the lung the permeability is 9.0E-05 mm<sup>2</sup>/(s·MPa), and the Lamé parameters  $\mu$  and  $\lambda$  are 6.92E-05MPa and 1.04E-04MPa, respectively [30]. Finally, the Lamé parameters  $\mu$  and  $\lambda$  are 2.1E-01MPa and 3.2E-01MPa, respectively for the heart.

## **4.2 Results and discussion**

### **4.2.1 Lung deformation**

The lung deformation was obtained during this normal quiet breathing simulation. The front view is shown in Fig. 4-1, and the lateral view is shown in Fig. 4-2. From the front view, we could observe the lung was expanded in lateral direction especially in dorsal portion of the lungs due to the bucket-handle motion of the ribs. The lateral view shows the anteroposterior diameter of the lung was increased especially in the cranial portion of the lung due to the pump-handle motion of the ribs. Obtained lung deformations indicated that the pump-handle motion of the upper ribs and the bucket-handle motion of the lower ribs predominantly influence the lung deformation during breathing.



**Fig. 4-1** Front view of lung deformation during normal quiet breathing

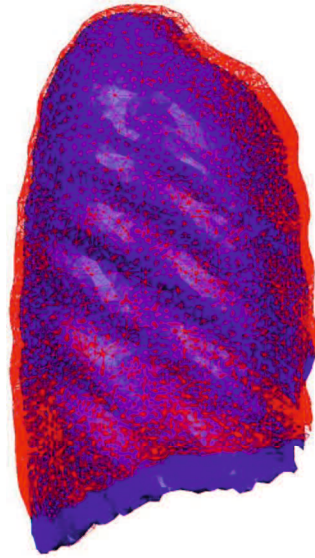


**Fig. 4-2** Lateral view of lung deformation during normal quiet breathing

### 4.2.2 Ventilatory volume, Alveolar and pleural pressures during normal quiet breathing

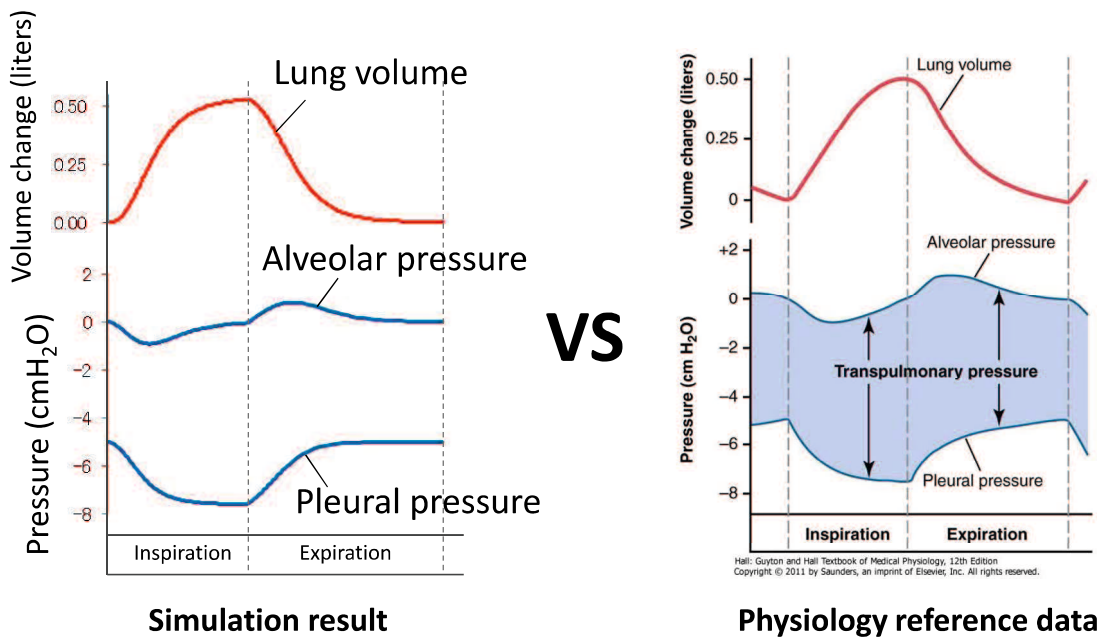


**Fig. 4-3** Variations of alveolar, pleural pressures and lung volume change during normal quiet breathing respiration

The simulation was performed by assuming a normal quiet breathing. Therefore, the thorax deformation was the same as the Fig. 4-19, Fig. 4-20 and Fig. 4-21 shows. The thorax deformation could influence the mechanical environment in the chest. During the inspiration and expiration, the variations of the lung volume, alveolar and pleural pressures were reproduced in this study, as shown in Fig. 4-3.

During the inspiration, from the contraction of external intercostal muscles and diaphragm, the ribs were moved up and the diaphragm fell down. So the Negative pleural pressure was produced in the Pleural space, the lungs were expanded and lung volume was increased. Finally, the Negative alveolar pressure was produced. During the expiration, due to the muscle's deactivation, elastic-recoil forces of the muscles and lungs returned the ribs and the diaphragm rose up. So the pleural pressure and lung volume were gradually returned, and at the same time the positive alveolar pressure was produced.

The alveolar pressure was computed by the hydrostatic pressure  $p$  (chapter 4.1.1) in the lungs. The hydrostatic pressure  $p$  was selected at the nodes which locate far from the pressure boundary. Therefore, alveolar pressure was generated at the nodes of lung parenchyma when the air flowed from the lung parenchyma to the pressure boundary. On the other hand, the pleural pressure was computed by the hydrostatic pressure  $p$  in the pleural space. The pleural space was modelled as an incompressible material. Hence, when the thorax was expanded by the muscle contraction, the negative hydrostatic pressure  $p$  was generated in the pleural space due to the reactive force from the lungs. Consequently, during normal quiet

breathing, the negative pleural pressure became larger in the inspiratory process and returned to zero during the expiratory process.

The variation of the pleural pressure depends on the stiffness of the lung and the resistance of airflow due to the viscosity happened in the alveoli level. Therefore, alveolar pressure and the resistance of airflow could influence the value of the pleural pressure. In addition, if the pleural pressure generated by the muscle contraction becomes smaller, the lung volume changing will also be influenced and reduces. It means that the lung volume changing, alveolar pressure and pleural pressure have a critical relationship with each other. It is worth to mention that obtained lung volume changing, alveolar pressure and pleural pressure were consistent with the physiological measurement [2], as shown in Fig. 4-3.

### **4.3 Conclusions**

The lung deformation during ventilation due to the thorax deformation is reproduced by additionally consider the lung as porous hyperelastic material. The porous hyperelastic material macroscopically reproduced the lung deformation and the airflow during ventilation simultaneously. This approach simulated the mechanical environment inside the chest by reproducing the alveolar pressure and pleural pressure during breathing. Moreover, resultant lung volume change, alveolar pressure and pleural pressure have a good consistence with clinical measurements, thereby validated our approach.

# 5 Influences of ventilation on blood circulation during cardiopulmonary resuscitation

---

With established respiratory model, we reproduced the mechanical environment in the chest during ventilation. As it should be, the ventilation can also affect the mechanical environment during breathing or other chest motions such as performing cardiopulmonary resuscitation (CPR). CPR is an important first aid technique for life saving. CPR has been introduced and practically used for emergency of cardiopulmonary arrest in the past few decades. As the normal way, CPR is performed by an external force periodically applied on the sternum that could change the pressure circumstance around the heart in order to reinstate partial oxygenated blood flow to the brain and heart, and at same time by keeping an open airway to promote ventilation. However, the ventilation during CPR had been a big argument for a long time.

By the experiments performed on domestic swine, K. B. Kern et al. demonstrated that there is no difference in survival even though the airway was totally occluded [61]. However, the studies using animals also have been criticized for the differences of airway mechanics between human and of the animals. The problem is that it is almost impossible to perform experiments on human body directly. Therefore, it is expected that a computational method would be a valuable aid in revealing the mechanical

environment in the human chest during CPR and improving the performing procedure of CPR.

In this study, by introducing the circulatory systems, we simulate CPR with established respiratory model which could reproduce several physiological phenomena during CPR, such as thorax deformation, lung deformation, heart deformation, pleural pressure, cardiac chamber pressure, and the ventilation. Base on this, we investigate the influences of the ventilation on blood circulation during CPR and propose a new method to perform CPR.

## **5.1 Methods**

### **5.1.1 Connection of the circulatory system**

When the cardiac muscles contract in a living body, the circulatory system causes loads and influences the mechanical environment in the heart. As Fig. 5-1 shows, the left atrium delivers the blood into the left ventricle, and the contraction of the left ventricle pumps the blood throughout the body which is called main circulation. The same as the left atrium and ventricle, the right atrium delivers the blood into the right ventricle, and the contraction of the ventricle pumps the blood into the lung circulation. Before the right and left atrium contracts, the load is called preload, and the load against the muscle contractile force is called afterload.

In order to consider the influence from the circulatory systems during CPR, a circuit was connected to the heart representing the preload and afterload, as shown in Fig. 5-2 [62]. According to the reference [62], the parameters in the circuit were adopted as follow, for the afterload:  $R_1 = 10\text{Pa} \cdot \text{s/ml}$ ,

$R_2 = 160\text{Pa}\cdot\text{s/ml}$ ,  $C = 0.016\text{ml/Pa}$ ; for the preload:  $R_1 = 3.466\text{Pa}\cdot\text{s/ml}$ ,  
 $R_2 = 12\text{Pa}\cdot\text{s/ml}$ ,  $C = 0.016\text{ml/Pa}$ .

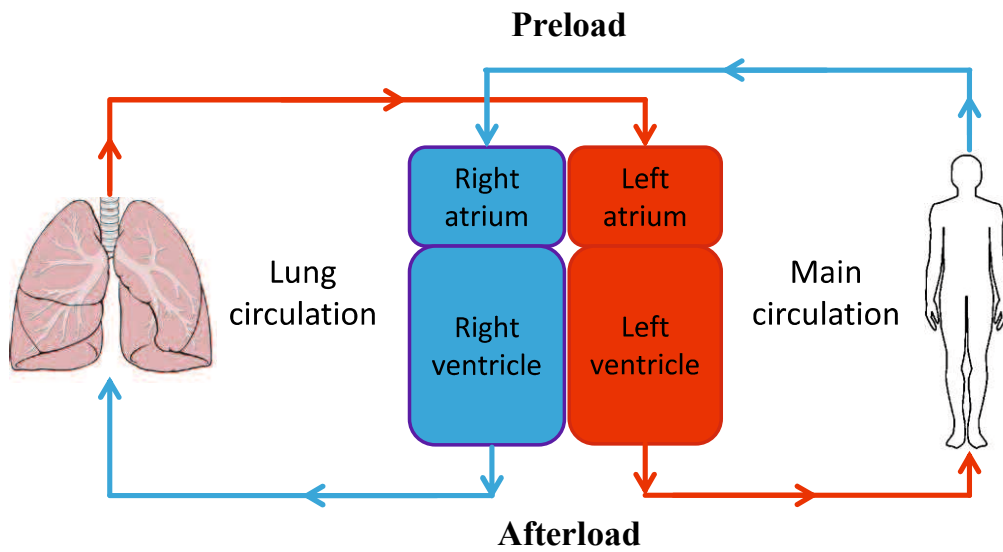


**Fig. 5-1** The main and lung circulation, and preload and afterload in human body.

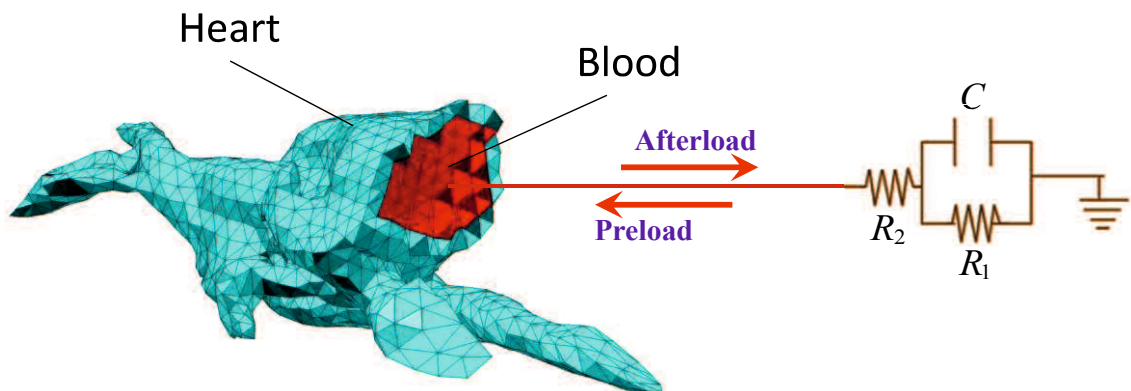


**Fig. 5-2** Circuit of the preload and afterload connected to the FEM model of the heart

### 5.1.2 Simulation procedure

An external force equal to 400N was applied on the sternum during 0.3s and generated a displacement in dorsal direction about 40mm, after that the external force gradually decreased to 0N in 0.3s. In order to investigate the influence from the ventilation, we simulated the CPR during open airway, occluded airway, open-occluded airway, occluded-open airway and occluded-open-occluded-open airway.

## 5.2 Results and discussion

### 5.2.1 Deformation of lung and heart

Fig. 5-3, Fig. 5-4, and Fig. 5-5 show the deformation results of the thorax, lung, heart under the external force (400N) and an open airway condition, respectively. It could be observed that during CPR, when the thorax was deformed due to the descending of the sternum, the heart became smaller and most moved in dorsal direction. And, the largest deformed portion of the lung located under the sternum and the lung also slightly moved in caudal direction caused a little downward movement of the diaphragm. It means that the mostly deformed portion in the chest during the thorax deformation was under the sternum where just the heart locates.

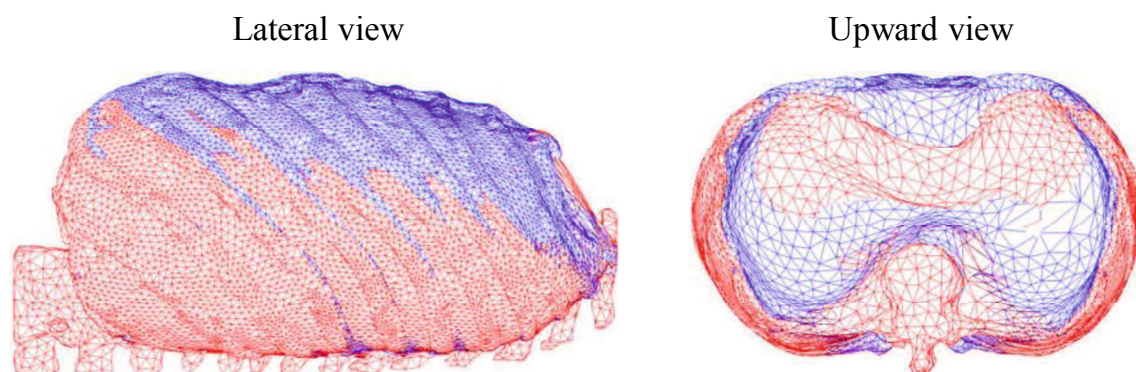


**Fig. 5-3** Deformation results of the thorax (blue: before deformation; red: after deformation)

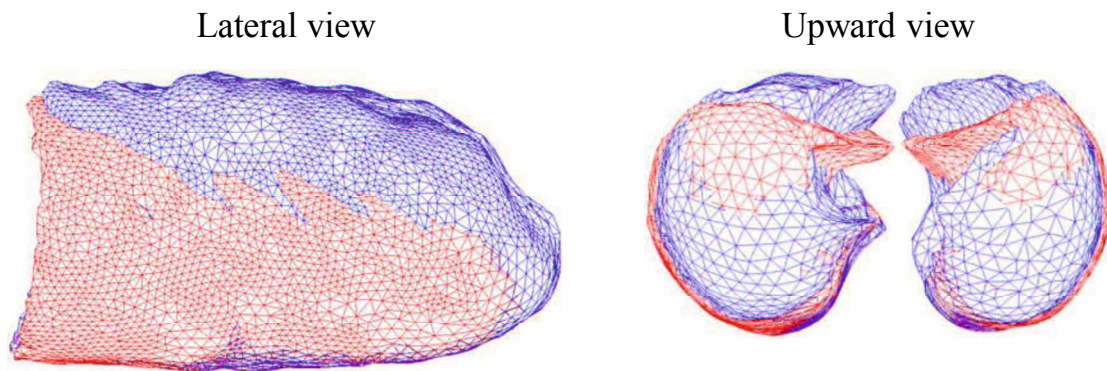


**Fig. 5-4** Deformation results of the lung (blue: before deformation; red: after deformation)

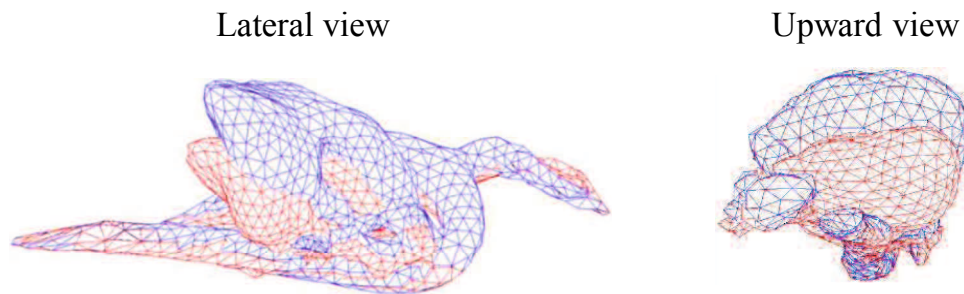


**Fig. 5-5** Deformation results of the heart (blue: before deformation; red: after deformation)

#### **4.2.2 Open airway and occluded airway cardiopulmonary resuscitation**

In this study, first we simulated the normal CPR with an open airway. We applied 0 at the pressure boundary of the node in the lung. Therefore, the air could cross the pressure boundary and the lung volume change was happened. Because the ventilation during CPR could influence the mechanical environment in the chest, therefore we also simulated the CPR with an occluded airway. We investigated the heart volume change, the

pressure in the heart and the pleural pressure during open and occluded airway, as shown in Fig. 5-6, Fig. 5-7, and Fig. 5-8.

During the sternum was lowered, the heart and lung were deformed in dorsal direction and the pleural pressure became larger, therefore the pressure in the heart also became higher. Finally, the heart became smaller and the blood was pumped out of the heart.

When airway was occluded, the air was constrained in the lung and the lung volume could not change, so that the pleural pressure during the occluded airway was higher than during the open airway. Also, this higher pleural pressure generated a larger heart volume change. It demonstrated that, as the experiments illustrated [61], the occluded airway could contribute to the blood circulation during CPR.

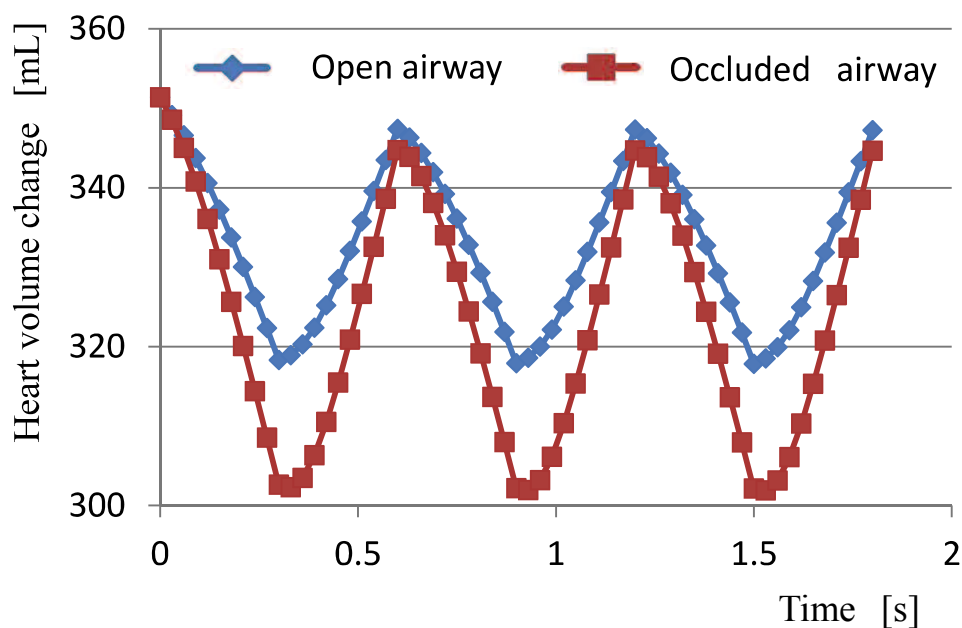


**Fig. 5-6** Heart volume change during open and occluded airway CPR.

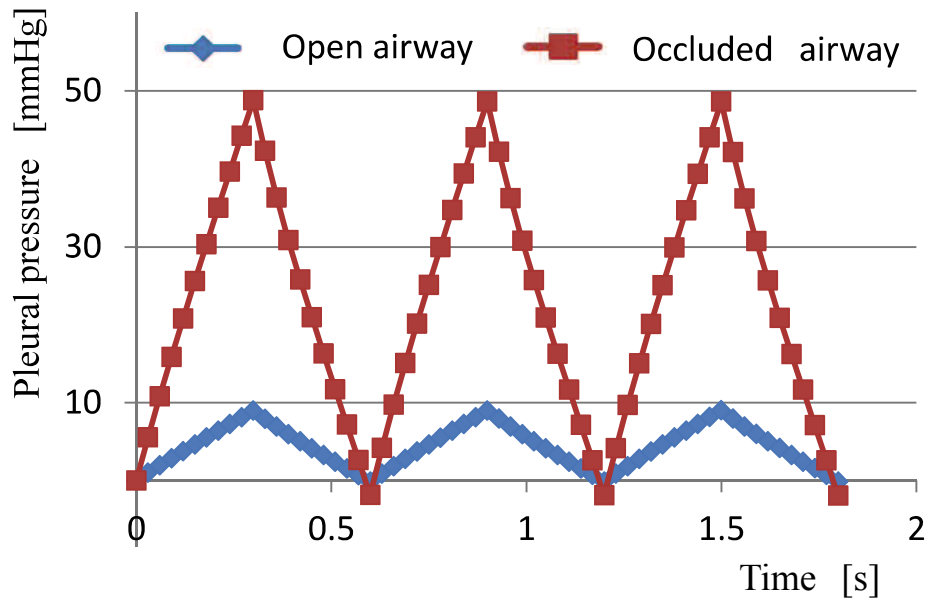


**Fig. 5-7** Pleural pressure during open and occluded airway CPR.

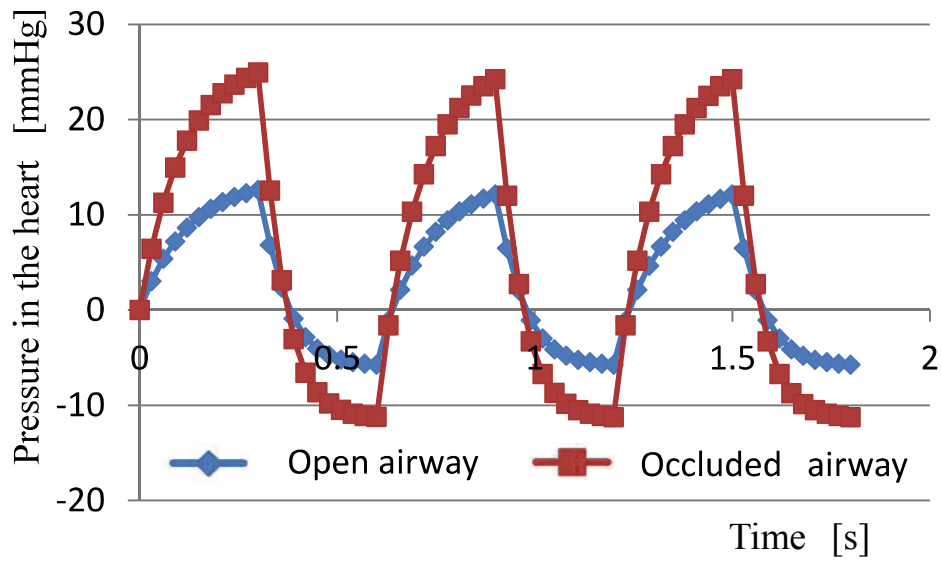


**Fig. 5-8** Pressure in the heart during open and occluded airway CPR.

### 5.2.3 Open-occluded airway and occluded-open airway cardiopulmonary resuscitation

Although the occluded airway could contribute to the blood circulation, the problem is the oxygen content decrease during CPR. Therefore, we simulated the open-occluded and occluded-open airway, as shown in Fig. 5-9, Fig. 5-10 and Fig. 5-11. In the open-occluded airway simulation, because the air in the lung was pumped out during the airway was open, so that if the airway was closed after that, the higher negative pleural pressure and pressure inside the heart were generated and this negative pleural pressure expanded the heart to make the heart larger than the original volume. More interesting, because the heart was expanded, therefore when the airway become open again, the restoring elastic energy in the muscles of the heart caused a large pressure in the heart, as shown in Fig. 5-11.

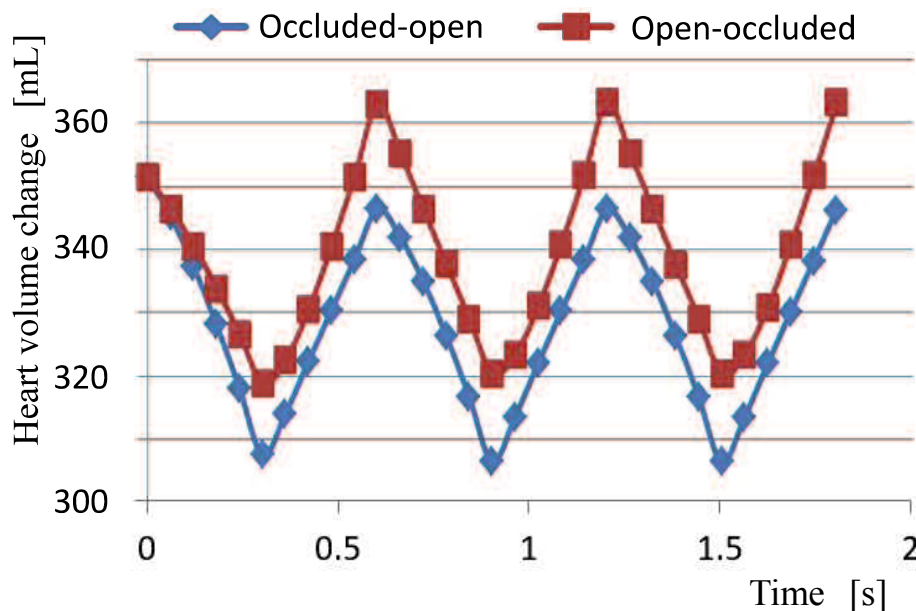


**Fig. 5-9** Heart volume change during occluded-open and open-occluded airway CPR.

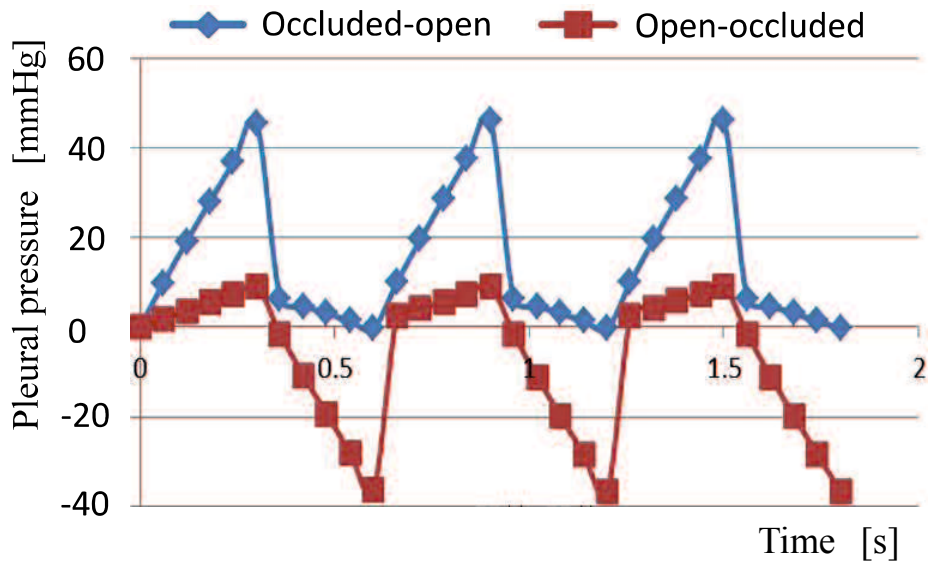


**Fig. 5-10** Pleural pressure during occluded-open and open-occluded airway CPR.

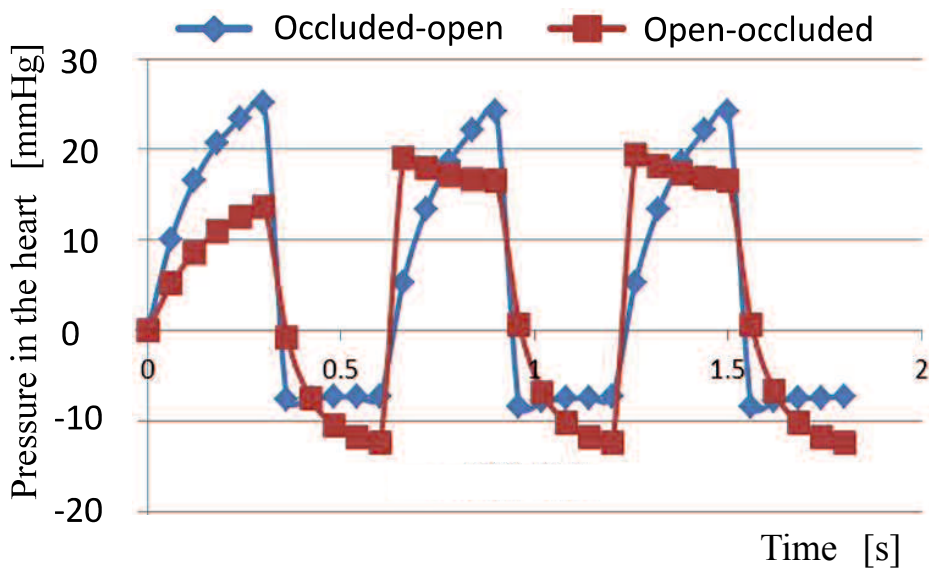


**Fig. 5-11** Pressure in the heart during occluded-open and open-occluded airway CPR.

On the other hand for occluded-open airway as shown in Fig. 5-9, Fig. 5-10 and Fig. 5-11, the larger volume change of heart was generated as that obtained in the occluded airway examination. When the airway become open after that, the air was pumped out of the lung due to the higher pleural pressure, and the pleural pressure become small at the same time. The higher negative pressure in the heart was generated because of the restoring elastic energy in the muscles of the heart which has been compressed smaller during the occluded airway. In this case, the heart volume change was not only the same as the occluded-open airway examination, but also the ventilation was also performed. It means that the efficiency of occluded-open airway CPR is better than the normal open airway CPR and occluded airway CPR.

#### **5.2.4 Occluded-open-occluded-open airway cardiopulmonary resuscitation**

The examinations of occluded-open and open-occluded airway illustrates that the occluded-open airway could compress the heart and the open-occluded airway could extend the heart. However, they have a same total volume change of the heart. In order to additionally increase the volume change of the heart, we simulated an occluded-open-occluded-open airway CPR.

As shown in Fig. 5-12, 5-13, 5-14, 5-15, first we closed the airway to obtain a larger volume change of the heart. Then, when we open the airway, displacement of the sternum also keep constant. Therefore, the air could flow out of the lung, and the pleural pressure become smaller, negative pressure was generated in the heart due to the recoiling force of the muscles,

and the volume of the heart also become smaller simultaneously. Because some air has been pumped out of the lung, so that if the airway was closed after that, a larger heart volume and a bigger negative pressure inside the heart could be obtained. Also, the negative pleural pressure reached largest at the same time. Finally, when the airway was open again, the air could flow into the lung, therefore the plural pressure return to zero and the volume of the heart also gradually return to original volume. Because the volume of the heart suddenly become smaller, a higher pressure was generated in the heart duo to the afterload.

In this examination, we obtained largest heart volume change and also consider the ventilation. These results indicated that the ventilation could predominantly influence the heart volume change, pleural pressure and the pressure in the heart during CPR. Consequently, the simulation results illustrates that the occluded-open-occluded-open airway CPR dominantly has a better efficiency than normal open CPR.

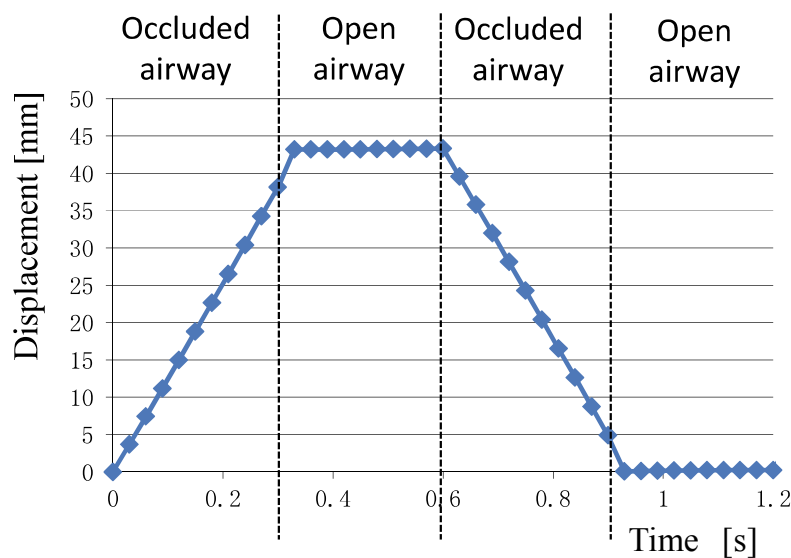


**Fig. 5-12** The displacement of the sternum in dorsal direction during occluded-open-occluded-open airway CPR.

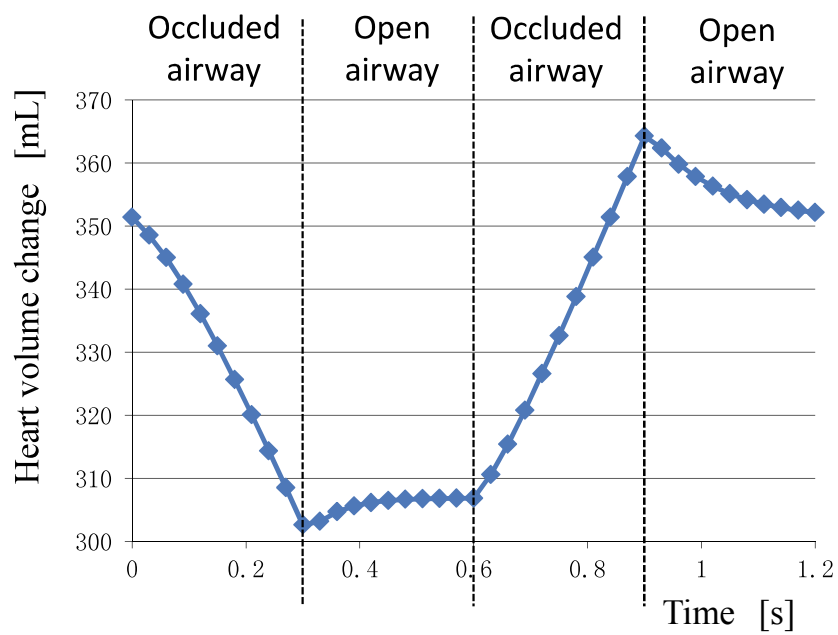


**Fig. 5-13** Heart volume change during occluded-open-occluded-open airway CPR.

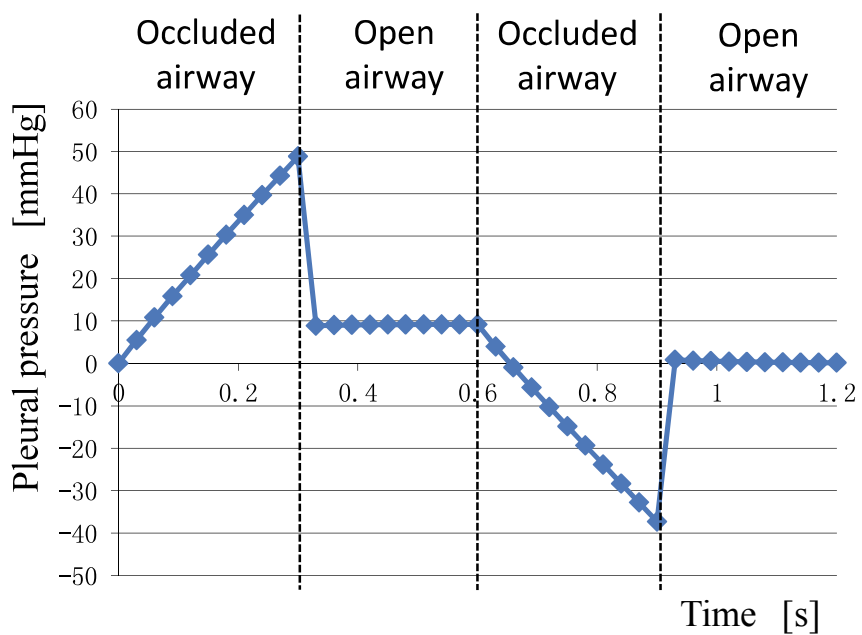


**Fig. 5-14** Pleural pressure during occluded-open-occluded-open airway CPR.

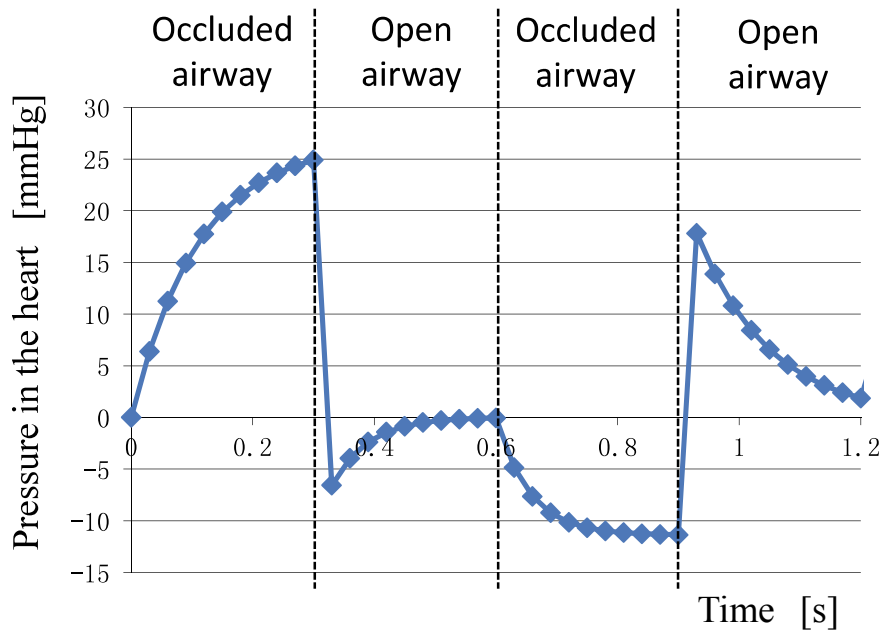


**Fig. 5-15** Pressure in the heart during occluded-open-occluded-open airway CPR

### 5.3 Conclusions

By introducing the circulatory system to established respiratory model, we simulated the thorax deformation, lung deformation, heart deformation, pleural pressure, cardiac chamber pressure, and the ventilation during CPR. Furthermore, we investigated the influence of the ventilation on the blood circulation during CPR. The simulation results indicated that as the experiment performed in animals, an occluded airway could increase the pleural pressure to contribute to the blood circulation during CPR. More importantly, when we closed, opened, closed and opened the airway during CPR, a predominantly larger heart volume change was obtained. This new

method to perform CPR also will be continuously studied and discussed in the future work with a precise FEM heart model.

# 6

## Conclusions

---

In this study, we established a computational mechanics model to simulate the human respiration, which could reproduce the biomechanical phenomena such as the ventilation, lung deformation, pleural pressure, alveolar pressure, respiratory muscles contraction, and chest movement.

As the main respiratory muscles to generate chest movement, due to the complex structure of the rib cage, detailed action of the intercostal muscles on the rib movement was first investigated in this study. From the simulation results and reference the experimental measurement in physiology, we concluded the mechanical action of the intercostal muscles on the rib cage. Because the respiratory effect of intercostal muscles depends on their mechanical action on the rib cage, so that from investigated mechanical action we also inferred the respiratory effect of the intercostal muscles and the respiratory effect had a good consistence with the experimental measurement. This investigation not only demonstrated the effectiveness of our approach on simulating rib motion, but also indicated some unclear mechanical actions of the intercostal muscles in physiology.

By reproducing the diaphragm motion additionally, we simulated the thorax deformation during breathing. The reproduction of pump-handle and bucket-handle motion during breathing which is the representative rib motion in physiology and 4D-CT images of the diaphragm motion during normal quite breathing validated our approach on simulating thorax

deformation. With this, we achieved the simulation of the thorax deformation by activating the primary respiratory muscles.

Base on this achievement of the thorax deformation, we additionally introduced porous hyperelastic material model for the lungs and reproduced the lung deformation, alveolar pressure and pleural pressure during normal quiet breathing. Obtained lung deformation demonstrated the rib motion predominantly influences the lung deformation. Owing to the Hill-type transversely isotropic hyperelastic skeletal muscle model, it make it possible to let us activate the respiratory muscles with a measurable muscle activation changing during breathing, thereby we reproduced the alveolar pressure and pleural pressure and lung volume change during normal quiet breathing. Although the alveolar pressure and pleural pressure and lung volume change have a critical relationship with each other, the simulation results is also consistent with physiological measurement. Consequently, we established the respiratory model, which could reproduce the thorax deformation, ventilation, lung deformation and mechanical environment inside the chest during human breathing.

The ventilation can affect the mechanical environment in the chest. As an application of established respiratory model, by modelled the heart as porous hyperelastic material and connect the circulatory system to the heart, we investigated the influence of the ventilation on the blood circulation during CPR, and concluded that an occluded-open-occluded-open airway CPR was a more effective method promoting the blood circulation to perform CPR.

In future work, to establish an integrated computational biomechanics model of the human respiratory system, we will add auxiliary respiratory

muscles and the organs in the abdominal wall to the current model. We will also introduce the airway system to develop an effective tool for revealing the mechanisms of human respiration and ultimately for diagnosing and treating respiratory diseases.

# References

- [1] Andre De Troyer and Aladin M. Boriek, “Mechanics of the Respiratory Muscles,” vol. 1, no. July, pp. 1273–1300, 2011.
- [2] J. E. Hall, “Guyton and Hall Textbook of Medical Physiology,” *Physiology*, p. 1091, 2010.
- [3] R. P. Onders, H. Aiyar, and J. T. Mortimer, “Characterization of the human diaphragm muscle with respect to the phrenic nerve motor points for diaphragmatic pacing.,” *Am. Surg.*, vol. 70, no. 3, pp. 241–7; discussion 247, 2004.
- [4] S. Matsuoka, Y. Kurihara, K. Yagihashi, M. Hoshino, N. Watanabe, and Y. Nakajima, “Quantitative assessment of air trapping in chronic obstructive pulmonary disease using inspiratory and expiratory volumetric MDCT,” *Am. J. Roentgenol.*, vol. 190, no. 3, pp. 762–769, 2008.
- [5] K. S. Burrowes, T. Doel, and C. Brightling, “Computational modeling of the obstructive lung diseases asthma and COPD.,” *J. Transl. Med.*, vol. 12 Suppl 2, no. Suppl 2, p. S5, 2014.
- [6] G. Tian, M. Hindle, S. Lee, and P. W. Longest, “Validating CFD Predictions of Pharmaceutical Aerosol Deposition with in Vivo Data,” *Pharm. Res.*, vol. 32, no. 10, pp. 3170–3187, 2015.
- [7] P. Manescu, H. Ladjal, J. Azencot, M. Beuve, E. Testa, and B. Shariat, “Four-dimensional radiotherapeutic dose calculation using biomechanical respiratory motion description,” *Int. J. Comput. Assist. Radiol. Surg.*, vol. 9, no. 3, pp. 449–457, 2014.
- [8] J. A. Haller and G. M. Loughlin, “Cardiorespiratory functions is significantly improved following corrective surgery for severe pectus excavatum: Proposed treatment guidelines,” *Minerva Pneumol.*, vol. 40, no. 1, pp. 1–7, 2001.

- [9] T. Nagasao, J. Miyamoto, T. Tamaki, K. Ichihara, H. Jiang, T. Taguchi, R. Yozu, and T. Nakajima, “Stress distribution on the thorax after the Nuss procedure for pectus excavatum results in different patterns between adult and child patients,” *J. Thorac. Cardiovasc. Surg.*, vol. 134, no. 6, pp. 1502–1507, 2007.
- [10] T. Nagasao, M. Noguchi, J. Miyamoto, H. Jiang, W. Ding, Y. Shimizu, and K. Kishi, “Dynamic effects of the Nuss procedure on the spine in asymmetric pectus excavatum,” *J. Thorac. Cardiovasc. Surg.*, vol. 140, no. 6, pp. 1294–1299.e1, 2010.
- [11] H. Loring, “Action of human respiratory muscles inferred from finite element analysis of rib cage,” pp. 1461–1465, 1992.
- [12] S. H. Loring and J. a Woodbridge, “Intercostal muscle action inferred from finite-element analysis.,” *J. Appl. Physiol.*, vol. 70, no. 6, pp. 2712–8, 1991.
- [13] M. P. M. Pato, N. J. G. Santos, P. Areias, E. B. Pires, M. de Carvalho, S. Pinto, and D. S. Lopes, “Finite element studies of the mechanical behaviour of the diaphragm in normal and pathological cases.,” *Comput. Methods Biomech. Biomed. Engin.*, vol. 14, no. 6, pp. 505–13, 2011.
- [14] N. J. G. Santos, “Preliminary Biomechanical Studies on the Diaphragmatic Function in Control and Patients with Loss of Motor Units,” pp. 1–100, 2009.
- [15] T. Ookura, H. Ito, S. Koshizuka, and A. Nomoto, “Diaphragm respiratory motion model with ribcage movement,” 2013.
- [16] M. Behr, J. Pérès, M. Llari, Y. Godio, Y. Jammes, and C. Brunet, “A three-dimensional human trunk model for the analysis of respiratory mechanics.,” *J. Biomech. Eng.*, vol. 132, no. 1, p. 014501, 2010.
- [17] H. Ladjal, J. Saade, M. Beuve, J. Azencot, J.-M. Moreau, and B. Shariat, “3D Biomechanical Modeling of the Human Diaphragm Based on CT Scan Images,” *World Congr. Med. Phys. Biomed. Eng.*

- May 26-31, 2012, Beijing, China SE - 574, vol. 39, pp. 2188–2191, 2013.
- [18] A. L. Didier, P. F. Villard, J. Saadé, J. M. Moreau, M. Beuve, and B. Shariat, “A chest wall model based on rib kinematics,” *Proc. - 2009 2nd Int. Conf. Vis. VIZ 2009*, pp. 159–164, 2009.
- [19] J. Saadé, A. Didier, R. Buttin, J. Moreau, M. Beuve, P. Villard, J. Botanique, and V. Nancy, “a Preliminary Study for a Biomechanical Model of the Respiratory System,” *Eng. Comput. Sci. Med. Imaging Oncol. VISAPP 2010*, pp. 509–515, 2006.
- [20] A. L. Didier, P. F. Villard, J. Y. Bayle, M. Beuve, and B. Shariat, “Breathing thorax simulation based on pleura physiology and rib kinematics,” *Proc. - 4th Int. Conf. Med. Inf. Vis. Biomed. Vis. MediViz 2007*, pp. 35–40, 2007.
- [21] H. Ladjal, B. Shariat, J. Azencot, and M. Beuve, “Appropriate Biomechanics and kinematics Modeling of the respiratory System : Human Diaphragm and Thorax,” pp. 2004–2009, 2013.
- [22] J. Awrejcewicz and B. Å□Uczak, “The finite element model of the human rib cage,” *J. Theor. Appl. Mech.*, vol. 45, pp. 25–32, 2007.
- [23] N. K. Ito H, Koshizuka S, Haga A, “Rib Cage Motion Model Construction Based on Patient-Specific CT Images Between Inhalation and Exhalation,” *Med. Imaging Technol.*, 2011.
- [24] P. F. Villard, M. Beuve, B. Shariat, V. Baudet, and F. Jaillet, “Simulation of lung behaviour with finite elements : Influence of bio-mechanical parameters,” *Proc. - Third Int. Conf. Med. Inf. Vis. - Biomed. Vis. MediVis 2005*, vol. 2005, pp. 9–14, 2005.
- [25] J. Eom, X. G. Xu, S. De, and C. Shi, “Predictive modeling of lung motion over the entire respiratory cycle using measured pressure-volume data, 4DCT images, and finite-element analysis.,” *Med. Phys.*, vol. 37, no. 8, pp. 4389–4400, 2010.
- [26] A. Al-Mayah, J. Moseley, M. Velec, S. Hunter, and K. Brock, “Deformable image registration of heterogeneous human lung

- incorporating the bronchial tree.,” *Med. Phys.*, vol. 37, no. 9, pp. 4560–4571, 2010.
- [27] F. Verdugo, C. J. Roth, L. Yoshihara, and W. A. Wall, “Efficient solvers for coupled models in respiratory mechanics,” *Int. j. numer. method. biomed. eng.*, 2016.
- [28] M. Kim, R. Bordas, W. Vos, R. A. Hartley, C. E. Brightling, D. Kay, V. Grau, and K. S. Burrowes, “Dynamic flow characteristics in normal and asthmatic lungs,” *Int. j. numer. method. biomed. eng.*, vol. 31, no. 12, 2015.
- [29] L. Berger, R. Bordas, K. Burrowes, V. Grau, S. Tavener, and D. Kay, “A poroelastic model coupled to a fluid network with applications in lung modelling,” *Int. j. numer. method. biomed. eng.*, vol. 32, no. 1, pp. 1–17, 2016.
- [30] O. J. Ilegbusi, Z. Li, B. Seyfi, Y. Min, S. Meeks, P. Kupelian, and A. P. Santhanam, “Modeling airflow using subject-specific 4DCT-based deformable volumetric lung models,” *Int. J. Biomed. Imaging*, vol. 2012, pp. 1–16, 2012.
- [31] Y. Yin, J. Choi, E. a. Hoffman, M. H. Tawhai, and C. L. Lin, “Simulation of pulmonary air flow with a subject-specific boundary condition,” *J. Biomech.*, vol. 43, no. 11, pp. 2159–2163, 2010.
- [32] J. Choi, M. H. Tawhai, E. A. Hoffman, and C. L. Lin, “On intra- and intersubject variabilities of airflow in the human lungs,” *Phys. Fluids*, vol. 21, no. 10, 2009.
- [33] R. K. Freitas, “Numerical investigation of the three-dimensional flow in a human lung model,” *J. Biomech.*, vol. 41, no. 11, pp. 2446–2457, 2008.
- [34] H. Kumar, M. H. Tawhai, E. A. Hoffman, and C. L. Lin, “The effects of geometry on airflow in the acinar region of the human lung,” *J. Biomech.*, vol. 42, no. 11, pp. 1635–1642, 2009.

- [35] A. F. DiMarco, G. S. Supinski, and K. Budzinska, "Inspiratory muscle interaction in the generation of changes in airway pressure," *J. Appl. Physiol.*, vol. 66, no. 6, pp. 2573–2578, 1989.
- [36] A. De Troyer, S. Kelly, and W. Zin, "Mechanical action of the intercostal muscles on the ribs," *Science (80-. )*, vol. 509, no. 1966, pp. 87–88, 1983.
- [37] A. De Troyer, P. A. Kirkwood, and T. A. Wilson, "Respiratory action of the intercostal muscles," *Physiol. Rev.*, vol. 85, no. 2, pp. 717–756, 2005.
- [38] T. a. Wilson, A. Legrand, P. A. Gevenois, and A. De Troyer, "Respiratory effects of the external and internal intercostal muscles in humans," *J. Physiol.*, vol. 530, no. 2, pp. 319–330, 2001.
- [39] T. a Wilson and A. De Troyer, "The two mechanisms of intercostal muscle action on the lung.," *J. Appl. Physiol.*, vol. 96, no. 2, pp. 483–488, 2004.
- [40] G. C. Sieck, L. F. Ferreira, M. B. Reid, and C. B. Mantilla, "Mechanical properties of respiratory muscles," *Compr Physiol*, vol. 3, no. 4, pp. 1553–1567, 2013.
- [41] D. R. Carrier, "Function of the intercostal muscles in trotting dogs: ventilation or locomotion?," *J. Exp. Biol.*, vol. 199, no. Pt 7, pp. 1455–65, 1996.
- [42] A. De Troyer, S. Kelly, P. T. Macklem, and W. A. Zin, "Mechanics of intercostal space and actions of external and internal intercostal muscles.," *J. Clin. Invest.*, vol. 75, no. 3, pp. 850–7, 1985.
- [43] D. R. Carrier, "Ventilatory action of the hypaxial muscles of the lizard *Iguana iguana*: a function of slow muscle," *J. Exp. Biol.*, vol. 143, pp. 435–457, 1989.
- [44] G. Hamberger, "De Respirationis Mechanismo et usu genuino," 1727.
- [45] E. DiGiovanna, S. Schiowitz, and D. Dowling, "An osteopathic approach to diagnosis and treatment," 2005.

- [46] T. Washio, J. Okada, and T. Hisada, “A Parallel Multilevel Technique for Solving the Bidomain Equation on a Human Heart with Purkinje Fibers and a Torso Model,” *SIAM Review*, vol. 52, no. 4, pp. 717–743, 2010.
- [47] F. H. Netter, *Atlas of human anatomy*, vol. 97. 2006.
- [48] G. A. Holzapfel, “Nonlinear solid mechanics: a continuum approach for engineers.” 2000.
- [49] J. A. C. Martins, E. B. Pires, R. Salvado, and P. B. Dinis, “A numerical model of passive and active behavior of skeletal muscles,” *Comput. Methods Appl. Mech. Eng.*, vol. 151, no. 97, pp. 419–433, 1998.
- [50] J. a. C. Martins, M. P. M. Pato, and E. B. Pires, “A finite element model of skeletal muscles,” *Virtual Phys. Prototyp.*, vol. 1, no. 3, pp. 159–170, 2006.
- [51] G. A. Farkas, “Mechanical properties of respiratory muscles in primates,” *Respir. Physiol.*, vol. 86, no. 1, pp. 41–50, 1991.
- [52] P. a L. S. Martins, R. M. N. Jorge, and a J. M. Ferreira, “A comparative study of several material models for prediction of hyperelastic properties: Application to silicone-rubber and soft tissues,” *Strain*, vol. 42, no. 3, pp. 135–147, 2006.
- [53] J. Remmers, “Inhibition of inspiratory activity by intercostal muscle afferents,” *Respir. Physiol.*, 1970.
- [54] A. Legrand and A. De Troyer, “Spatial distribution of external and internal intercostal activity in dogs,” *J. Physiol.*, vol. 518, no. 1, pp. 291–300, 1999.
- [55] P. Kolář, J. Neuwirth, J. Šanda, V. Suchánek, Z. Svatá, J. Volejník, and M. Pivec, “Analysis of diaphragm movement during tidal breathing and during its activation while breath holding using MRI synchronized with spirometry,” *Physiol. Res.*, vol. 58, no. 3, pp. 383–392, 2009.

- [56] P. Cluzel, T. Similowski, C. Chartrand-Lefebvre, M. Zelter, J. P. Derenne, and P. a Grenier, “Diaphragm and chest wall: assessment of the inspiratory pump with MR imaging-preliminary observations.,” *Radiology*, vol. 215, no. 2, pp. 574–583, 2000.
- [57] M. Eichinger, R. Tetzlaff, M. Puderbach, N. Woodhouse, and H.-U. Kauczor, “Proton magnetic resonance imaging for assessment of lung function and respiratory dynamics.,” *Eur. J. Radiol.*, vol. 64, no. 3, pp. 329–34, 2007.
- [58] N. S. Cherniack, M. A. Haxhiu, J. Mitra, K. Strohl, and E. Van Lunteren, “Responses of upper airway, intercostal and diaphragm muscle activity to stimulation of oesophageal afferents in dogs,” *J Physiol*, vol. 349, pp. 15–25, 1984.
- [59] O. L. Wade, “Movements of the thoracic cage and diaphragm in respiration,” *J. Physiol.*, vol. 124, no. 2, pp. 193–212, 1954.
- [60] X. CHEN, Y. CHEN, and T. HISADA, “A Study on Mechanical Model of Soft Tissues by Nonlinear Finite Element Analysis Based on Biphasic Theory,” *Trans. Japan Soc. Mech. Eng. Ser. A*, vol. 70, no. 697, pp. 1208–1215, 2004.
- [61] K. B. Kern, R. W. Hilwig, R. a. Berg, and G. a. Ewy, “Efficacy of chest compression-only BLS CPR in the presence of an occluded airway,” *Resuscitation*, vol. 39, no. 3, pp. 179–188, 1998.
- [62] T. Washio, J. Okada, A. Takahashi, K. Yoneda, Y. Kadooka, S. Sugiura, and T. Hisada, “Multiscale Heart Simulation with Cooperative Stochastic Cross-Bridge Dynamics and Cellular Structures,” *Multiscale Model. Simul.*, vol. 11, no. 4, pp. 965–999, 2013.